A Uniform Geometrical Theory of Diffraction Model of Very-High-Frequency Omni-directional Range Systems for Improved Accuracy

A thesis presented to

the faculty of

the Russ College of Engineering and Technology of Ohio University

In partial fulfillment

of the requirements for the degree

Master of Science

Augustine D. Yellu

August 2013

This thesis titled

A Uniform Geometrical Theory of Diffraction Model of Very-High-Frequency Omni-directional Range Systems for Improved Accuracy

by

AUGUSTINE D. YELLU

has been approved for

the Department of Electrical Engineering and Computer Science

and the Russ College of Engineering and Technology by

Chris Bartone

Professor of Electrical Engineering and Computer Science

Dennis Irwin

Dean, Russ College of Engineering and Technology

ABSTRACT

YELLU, AUGUSTINE D.,M.S., August 2013., Electrical Engineering

A Uniform Geometrical Theory of Diffraction Model of Very-High-Frequency Omni-directional Range Systems for Improved Accuracy

Director ofThesis: Chris Bartone

In this thesis a computer model for predicting the radiated fields and system errors of the Conventional Very-High-Frequency (VHF) Omni-directional Range (CVOR) and the Doppler VHF Omni-directional Range (DVOR) systems was developed and validated. This software model is based on the Uniform Geometrical Theory of Diffraction (UTD) and can predict the aforementioned fields and errors for different CVOR/DVOR transmitting station configurations. By integrating the model into an existing computer model namely the Ohio University Navaids Performance Prediction Model (OUNPM), a software which predicts the performance of Instrument Landing Systems (ILS) and CVOR/DVOR systems in multipath environments, an improvement in the accuracy of the CVOR/DVOR model of the OUNPPM is achieved. The improved CVOR/DVOR error prediction model of the OUNPPM presents an accurate and inexpensive means for siting CVOR/DVOR system ground stations.

ACKNOWLEDGEMENTS

I want to express my gratitude to the Avionics Engineering Center (AEC), Ohio University for funding my M.S. education. My heartfelt thanks go to the chairman of my thesis committee and academic advisor Professor Chris Bartone, and co-Advisor Dr Simbo Odunaiya for supervising this thesis, and their academic guidance throughout my studies. I express my sincere appreciation to Prof Michael Braasch and Prof. Eric Stinaff for their invaluable and insightful inputs and for finding time within their schedule to serve on my thesis committee.

I also express my gratitude to Dr. Ronald Marhefka of the Electroscience Laboratory, Ohio State University for helping me understand some concepts in the uniform theory of diffraction, and specifically for his help in formulating the mathematical search equation for finding the positions of diffraction points along a curved edge. To Dr. Kent Chamberlain for his insight on how to model the Doppler VHF Omni-directional Range, I am very appreciative. I am deeply grateful to Chad Mourning for his help with integrating the initial stand-alone model that I developed into the Ohio University Navigation Performance Prediction Model. I am grateful to Scott Nykl for his help in understanding some concepts in C++ programming.

I also want to use this opportunity to express my gratitude to my parents Felix and Victoria, and my siblings for their emotional and financial support throughout these years. I also express my thanks to Aki for her encouragement and support. To crown it all I express my ultimate thanks to God without whose guidance and protection all this would have been impossible.

TABLE OF CONTENTS

LIST OF TABLES

LIST OF FIGURES

LIST OF ABBREVIATIONS

AIEE	American Institute of Electrical Engineers
AM	Amplitude Modulation
CAA	Civil Aeronautics Administration
CVOR	Conventional VHF Omni-directional Range
DOT	Department of Transportation
DSB	Double Sideband
DVOR	Doppler VHF Omni-directional Range
SSB	Single Sideband
EFPD	Edge-Fixed Plane of Diffraction
EFPI	Edge-Fixed Plane of Incidence
EM	Electromagnetic
FAA	Federal Aviation Administration
FM	Frequency Modulation
GO	Geometrical Optics
ICAO	International Civil Aviation Organization
IEEE	Institute of Electrical and Electronics Engineers
ILS	Instrument Landing Systems
ISB	Incidence Shadow Boundary
LOS	Line of Sight
LSB	Lower Sideband
MN	Magnetic North

OUNPPM	Ohio University Navigation Performance Prediction Model
PEC	Perfect Electrical Conductor
PO	Physical Optics
PTD	Physical Theory of Diffraction
RF	Radio-Frequency
RSB	Reflection Shadow Boundary
USB	Upper Sideband
UTD	Uniform Theory of Diffraction
VHF	Very High Frequency
VOR	VHF Omni-directional Range
VORTAC	Tactical VOR
2-D	2-Dimensional
3-D	3-Dimensional
rpm	Revolutions per minute
rps	Revolutions per second

CHAPTER 1: INTRODUCTION

1.1 Overview

The Federal Aviation Administration (FAA) is an agency under the United States (US) Department of Transportation (DOT) that regulates aviation in US [1]. The FAA is in charge of optimizing and ensuring safety in the US airspace [1]. To this end, the FAA amongst other responsibilities is responsible for standardizing systems for navigation on the US airways [1]. Instrument Landing Systems (ILS) and Very-High-Frequency (VHF) Omni-directional Range (VOR) systems are some of these navigation aids [2]. ILS consists of localizers and glide slopes which are used respectively for lateral and vertical precision approach [2]. VOR systems transmit signals that are used by a receiver aboard an aircraft to compute the bearing of the aircraft with respect to a VOR transmitting station [2]. VOR systems are used for en route navigation and approach [2]. Two (2) types of VOR systems namely the Conventional VOR (CVOR) and the Doppler VOR (DVOR) are the most popular variants in use by the FAA [3]. ILS and VOR systems are also International Civil Aviation Organization (ICAO) standards [3].

The performance of radio-navigation aids such as ILS and CVOR/DVOR systems is sensitive to the environments in which they operate. Multipath from buildings and other structures in the vicinity of ILS/CVOR/DVOR ground stations combines with direct signals to produce a combined signal whose amplitude and phase properties differ from those of the direct signal. An airborne receiver (ILS/ CVOR /DVOR) which intercepts and processes such multipath “polluted” signals would output erroneous position or bearing indications. [3]

The Ohio University Navaids Performance Prediction Model (OUNPPM) is a computer model that can be used to predict the effects of multipath on the performance of ILS and CVOR/DVOR systems. The CVOR/DVOR ground station is modeled using the Uniform Geometrical Theory of Diffraction (UTD). The multipath field from obstacles in the field of view of the CVOR/DVOR system transmitting antennas is modeled by the Physical Optics (PO) method of electromagnetic scattering analysis. ILS and CVOR/DVOR receiver models are implemented in the OUNPPM to process the composite of the direct and multipath signals. [4, 5, 6]

1.2 Problem Statement

The main problem to be solved for this research is to improve the performance of the CVOR/DVOR error prediction model of the OUNPPM. Additionally, verification of this improvement is considered to be part of this research effort.

1.3 Scope of Thesis

Results of flight validation tests of the OUNPPM reported in [7] indicate that although the OUNPPM predictions and flight tests results follow the same trend, the OUNPPM overestimates CVOR bearing errors and underestimates DVOR bearing errors. The ILS model of the OUNPPM is however known to perform accurately. A new CVOR/DVOR model is developed in this thesis. The improved OUNPPM with the new CVOR/DVOR model will be referred to as the *new* OUNPPM in the rest of this document to distinguish it from the *old* OUNNPM with the reported inaccurate CVOR/DVOR model.

The old OUNPPM overestimates CVOR system errors and underestimates DVOR system errors. It can be inferred that since the ILS and CVOR/DVOR models of the OUNPPM employ the same Physical Optics (PO) scattering model to compute the multipath fields, the inaccurate performance of the old CVOR/DVOR model is due to the manner in which the old CVOR/DVOR ground/transmitting station was modeled. The assumptions in the old CVOR/DVOR model of the old OUNPPM are as follows:

1. The CVOR/DVOR ground station antenna has an isotropic pattern [6].
2. The CVOR/DVOR ground station has only one antenna which is centered above a circular metallic screen which is referred to in CVOR/DVOR community as the counterpoise [6].

Based on assumptions 1 and 2 listed above, the old CVOR/DVOR ground station in the old OUNPPM was modeled using a 2-dimensional (2-D) form of UTD. Assumptions 1 and 2 are oversimplifications and are responsible for the inaccuracy of the CVOR/DVOR model of the OUNPPM.

To improve the fidelity of the CVOR/DVOR model of the OUNPPM, the CVOR/DVOR ground station is remodeled using 3-dimensional (3-D) UTD, and a new receiver model is implemented to process the composite of the direct CVOR/DVOR signal (i.e., field) from the station and the multipath field. In this improved new CVOR/DVOR system ground station model, the transmitting antennas are modeled as Alford loops which are the antennas typically used in the CVOR/DVOR ground station systems. All 4 antennas in the CVOR system and the 51 antennas in the DVOR system are modeled. The new OUNPPM also expands the capabilities and applications of the OUNPPM. First of all, course errors that result from the inherent configuration of the CVOR/DVOR ground station can be simulated with this new OUNPPM. Thus the new OUNPPM can be used to accurately investigate the effects of parameters such as counterpoise size, counterpoise height above ground, antenna height above counterpoise, and ground type on CVOR/DVOR systems' radiated electric field intensities, and course errors. By integrating the improved 3-D UTD CVOR/DVOR ground station model with the PO scattering multipath model, the performance of CVOR/DVOR systems in multipath environments can more accurately be investigated. The 2-D UTD ground reflection model implemented in the old OUNPPM has been modified in this new model to incorporate the 3-D UTD fields reflected off the ground.

Figure 1-1 illustrates the structure of the new OUNPPM Model. The only fields modeled in the new OUNPPM are those represented by rays labeled 1-11 in Figure 1-1.

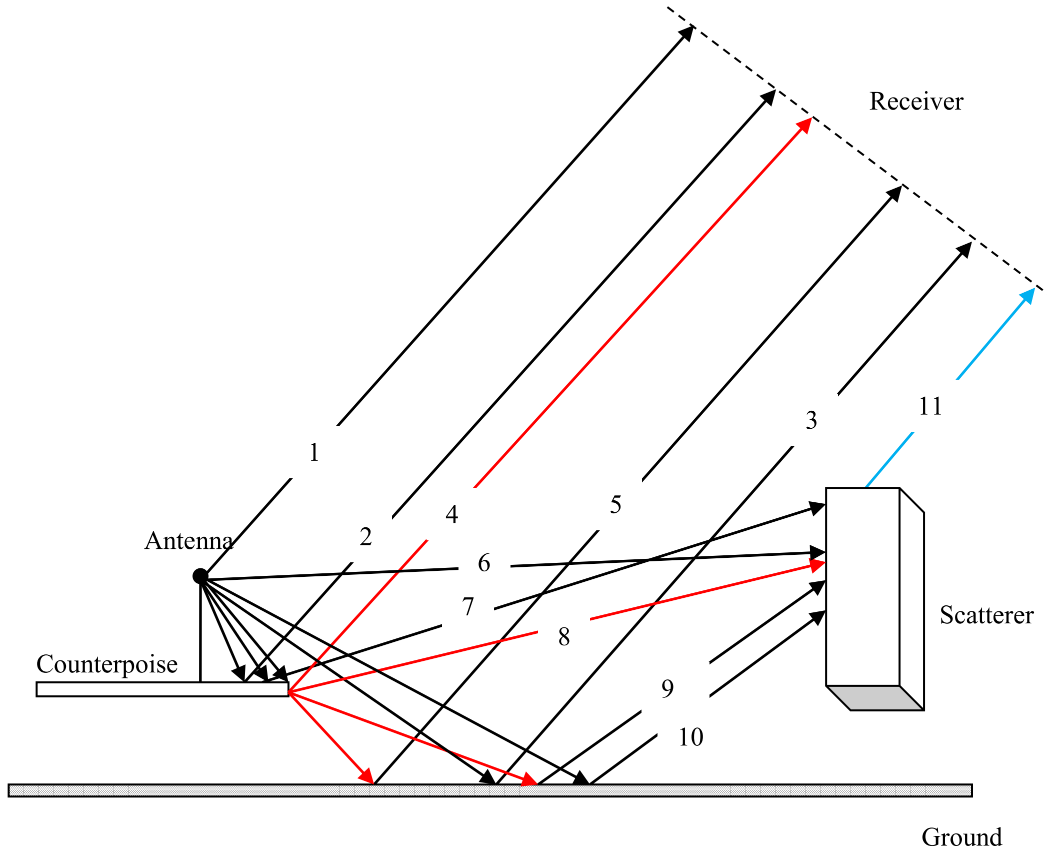

Figure 1-1. CVOR/DVOR Model of OUNPPM illustrating relevant fields (not to scale).

The multipath field represented by the ray labeled 11 in Figure 1-1 is computed using an existing PO Scattering Model. Fields, represented by rays 6, 7, 8, 9 and 10 in Figure 1-1 are supplied as inputs to this PO Scattering Model. The PO Scattering Model then computes the multipath field (ray 11) using the aforementioned inputs. Figure 1-2 is an input-output representation of the PO Scattering Model.

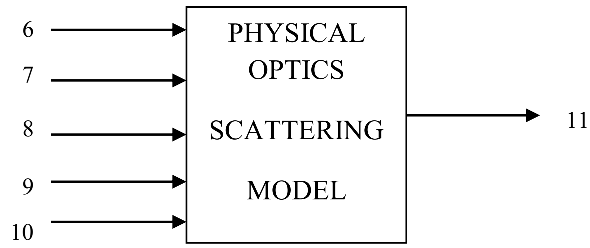

Figure 1-2. Input-output representation Physical Optics Scattering Model.

A word of note for computing the fields reflected off the ground/terrain is in order at this point. The ground reflected fields are those represented by rays 3, 5, 9, and 10 in Figure 1-1. In order to compute these fields, the reflection coefficient of the ground which depends on the electrical properties of the ground, the angle of incidence of the incident field on the ground, and the frequency of operation must be determined first. An existing ground reflection model is applied in this new OUNPPM to determine each of the ground reflection coefficients. Thus throughout this document the ground reflection coefficient will be represented by a complex-valued function,

$\mathbf{\Gamma}_{\perp, GROUND}(\omega, \delta, \sigma, \varepsilon)$

Where,

ω = Angular frequency at operating frequency of CVOR/DVOR, [rad/m]

δ = Angle of incidence on the ground/terrain, [degrees]

σ = Conductivity of ground, [S/m]

ε = Permittivity of ground, [Farad/m]

A subscript "$\perp$" has been used in $\mathbf{\Gamma}_{\perp,GROUND}(\omega, \delta, \sigma, \varepsilon)$ in reference to the fact that it is the horizontal/perpendicular polarization reflection coefficient that is being referred to since CVOR/DVOR systems employ a horizontal polarization scheme.

For instance, in order to determine the ground reflection coefficient for the field represented by ray 3, the angle of incidence, δ_3 on the ground (see Figure 1-3), the frequency of operation of the CVOR/DVOR ground station and the type of ground i.e., model selects the correct electrical properties depending on the type of ground specified, are input into the ground reflection model. The ground reflection model outputs the complex-valued ground reflection coefficient. The angle of incidence needed to compute the field represented by ray 5 is δ_5 (see Figure 1-3).

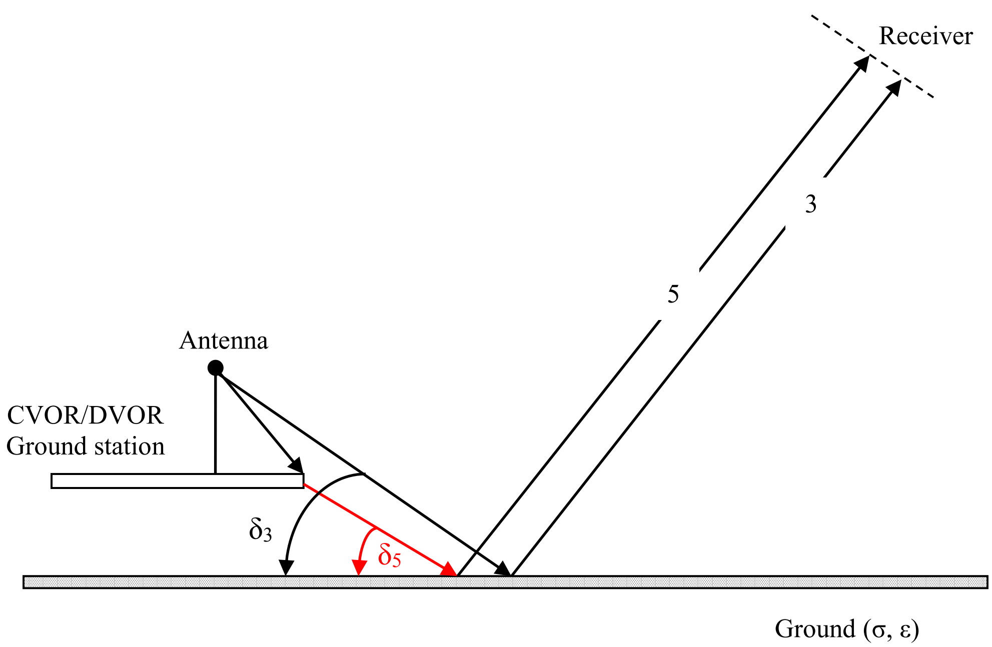

Figure 1-1. Ground reflection model of OUNPPM.

CHAPTER 2: THEORETICAL BACKGROUND

2.1 VOR System Overview

2.1.1 Conventional VHF Omni-directional Range (CVOR) System. The CVOR system is a radio direction finding system operating in the 108.00 -117.95 MHz Radio Frequency (RF) band (only the 112 MHz – 117.95 MHz part of the band is used) that enables an aircraft to determine its bearing from the CVOR transmitter station with respect to Magnetic North (MN) [3]. The choice of VHF frequencies prevents contamination of the CVOR guidance signals by sky and ground wave propagation [8]. A horizontal polarization scheme has been adopted for CVOR systems because tests indicated that this scheme was less susceptible to multipath than vertical polarization [9]. The CVOR system consists of a ground segment and airborne segment. [3]

Figure 2-1 illustrates the main elements of the standard FAA/ICAO CVOR ground station [8]. The CVOR ground station comprises an array of four (4) Alford loops mounted above a counterpoise [3, 10]. The counterpoise raises the radiated RF pattern in order to minimize the effect of the local ground and nearby buildings etc. on the signals radiated from the CVOR ground station [3, 8]. Alford loops are used in CVOR ground stations due their high efficiency and horizontal polarization purity in the VHF band [11]. As shown in Figure 2-2 the Alford loops are arranged in a square configuration so that the center of the array coincides with the center of the counterpoise, and are designated north-west (NW), north-east (NE), south-west (SW), and south-east (SE) depending on their positions with respect to MN [3, 10]. The NW and SE Alford loops form one pair and the NE and SW Alford loops constitute another pair [3, 10].

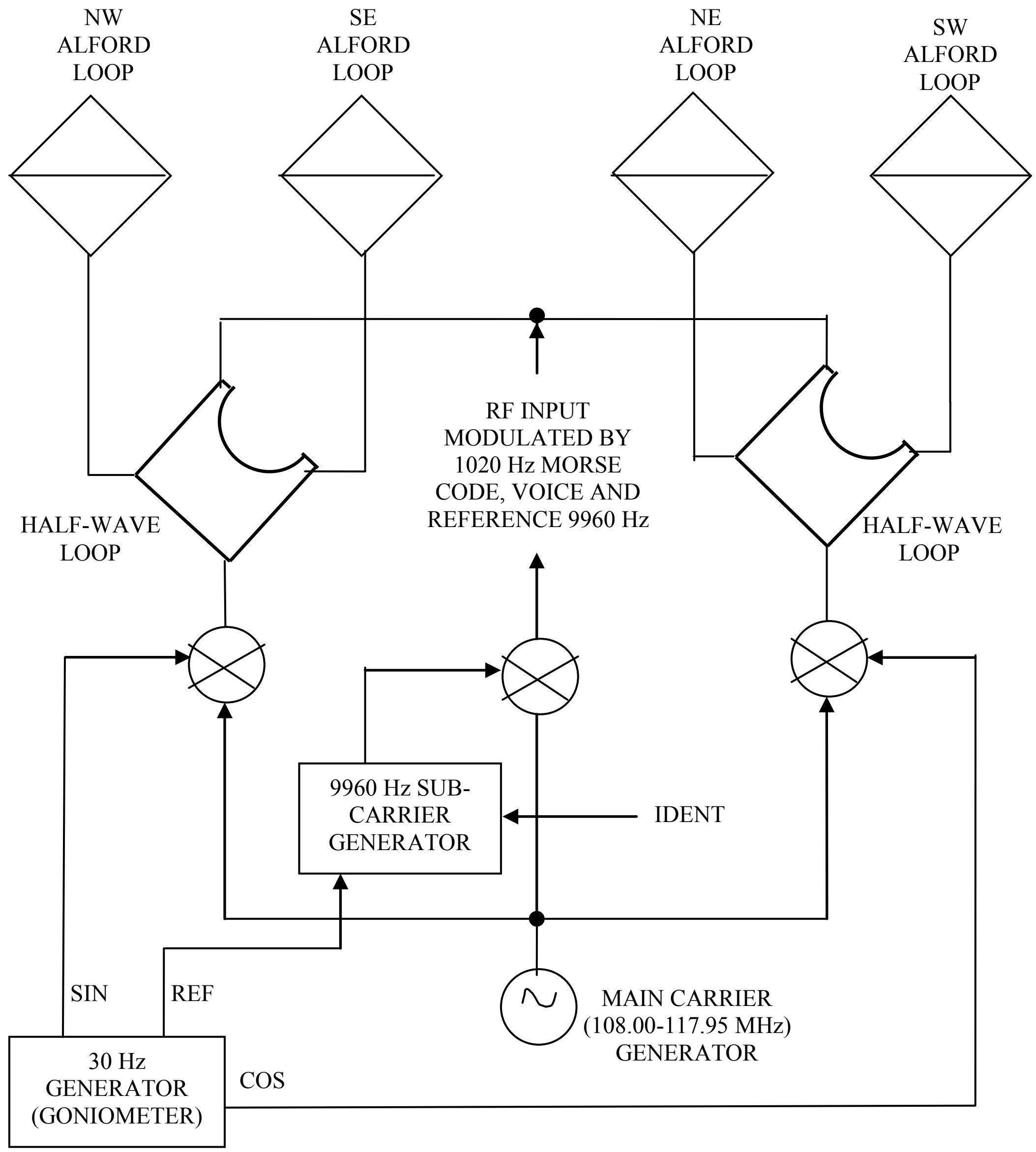

Figure 2-1. CVOR ground station. This figure was redrawn from [8].

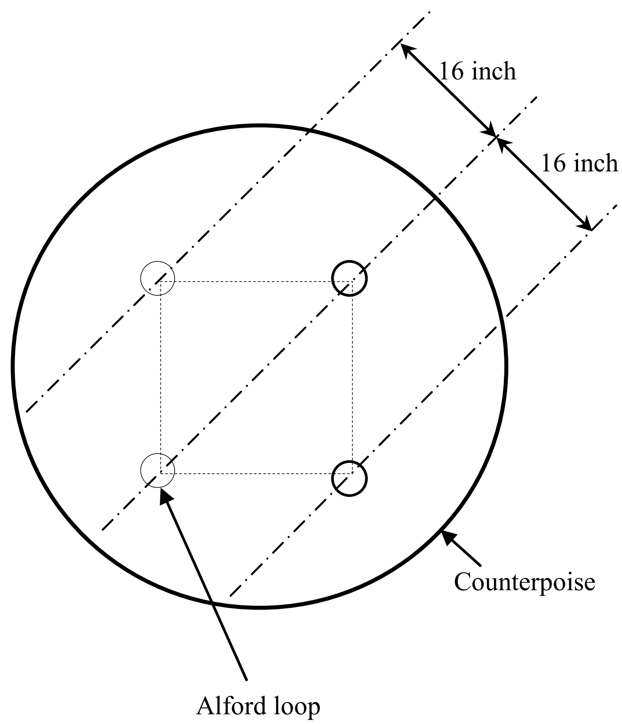

Figure 2-2. Top-view of CVOR ground station antenna array (Redrawn from [9]).

A main RF carrier in the108-117.95 MHz band is amplitude modulated with a Morse code station identification signal, a 9.96 KHz sub-carrier and voice. The 9.96 KHz sub-carrier is frequency modulated (FM) with a 30 Hz signal [3, 8, 10]. Fifty (50) percent of the main RF power with its aforementioned amplitude modulation (AM) is fed into the NW/SE antenna pair, and the other 50 percent of the RF power into the NE/SW antenna pair [8, 10]. The RF power supplied to each antenna pair is divided equally between the antennas of that pair [10]. The antennas of each pair are fed in phase [10]. The resulting radiation pattern of the main RF carrier input is therefore isotropic in the azimuth plane [8, 10]. Thus, the 30 Hz FM on the 9.96 KHz sub-carrier has a constant phase around the CVOR station and is known as the reference signal [8, 10].

The goniometer (i.e., 30 Hz generator), (see Figure 2-1) generates two (2) quadrature double sideband suppressed carrier (DSB-SC) signals [9, 10]. One antenna pair is fed with one DSB-SC signal, and the second pair fed with the other DSB-SC signal. The antennas of each pair are fed-out-of-phase with their respective DSB-SC signal. The half wave bridge circuits in Figure 2-1 isolate the carrier and DSB-SC signal inputs into the CVOR antenna array from each other [8, 10]. The composite DSB-SC pattern from the CVOR array forms a figure-eight radiation pattern [10]. The goniometer rotates its DSB-SC signal outputs at 30 Hz, and therefore the figure-eight DSB-SC pattern rotates at 30 Hz [10]. The rotating "separately radiated" [10] composite DSB-SC signal combines with the isotropic radiated carrier in space through a process known as *space modulation* to produce a rotating cardioid pattern [10]. The result is a 30 Hz amplitude modulation of the main RF carrier.

At a goniometer phase angle of 135 degrees, the maximum of the cardioid radiation pattern lines up with the MN radial [10]. The position of this maximum shifts proportionally in the clockwise sense with the progression of the goniometer angle at a rate of 30 Hz [10]. Since the reference pattern is omni-directional, it implies that the position of the cardioid maximum is controlled by the phase of the 30 Hz AM signal component. The phase of this 30 Hz AM component is in turn controlled by the goniometer angle. At MN, the phase of the 30 Hz AM is 135 degrees, and at a bearing of 1 degree (measured clockwise from MN) its phase is 136 degrees, and so on [10]. Since the phase of this 30 Hz AM is direction dependent, it is aptly called the variable signal [8, 10]. The bearing (audio-phase) of the aircraft is derived from the phase difference between this variable signal, and the 30 Hz FM (reference signal) on the main carrier [8, 9, 10]. In order to set the bearing at MN to zero degrees, the reference signal's phase is fixed at 135 degrees [10].

The airborne segment of the CVOR consists of a horizontal polarized antenna typically a V-dipole, and a CVOR receiver to process the CVOR signal [9]. The CVOR "nav composite" [8] signal received by the airborne receiver is expressed [12] as

$$s(t) = m(t)\cos\omega_c t \qquad (2\text{-}1)$$

Where:

$\omega_c = 2\pi$ (108.00 MHz to 117.95 MHz), [rad/s]

$m(t) = 1 + 0.3\cos(\omega_m t + \theta_1) + 0.3\cos[\omega_{sc}t + 16\cos(\omega_m t + \theta_2)] + 0.1\cos(\omega_{ID}t + \theta_3)$, [V]

$\omega_m = 2\pi f_m$, [rad/s]

$\omega_{sc} = 2\pi f_{sc}$, [rad/s]

$\omega_{ID} = 2\pi f_{ID}$, [rad/s]

θ_1 = Phase of variable signal, [rad]

θ_2 = Phase of reference signal, [rad]

θ_3 = Phase of station identification signal, [rad]

f_m = 30 Hz (reference and variable signal frequency)

f_{sc} = 9960 Hz (frequency of sub-carrier signal)

f_{ID} = 1020 Hz (CVOR station identification signal)

The signal (2-1) is processed by a CVOR receiver. The major components of a typical CVOR receiver are illustrated in Figure 2-3. The CVOR nav composite (2-1) is first amplified and down-converted before further processing [8]. The AM detector recovers all the amplitude modulations on (2-1) [3, 8, 9]. A 30 Hz filter extracts the 30 Hz AM (variable signal) on the main carrier [3, 8, 9]. The 9960±480 Hz band pass filter extracts the 9960 Hz FM sub-carrier from the detected AM envelope [3, 8, 9]. FM demodulation of this sub-carrier by the discriminator yields the 30 Hz reference signal [3, 8, 9]. The bearing ($\theta_{bearing}$) is computed by the difference between phases of the 30 Hz FM and 30 Hz AM tones. With reference to (2-1), the bearing to the CVOR ground station is given [12] by

$$\theta_{bearing} = \theta_2 - \theta_1 \tag{2-2}$$

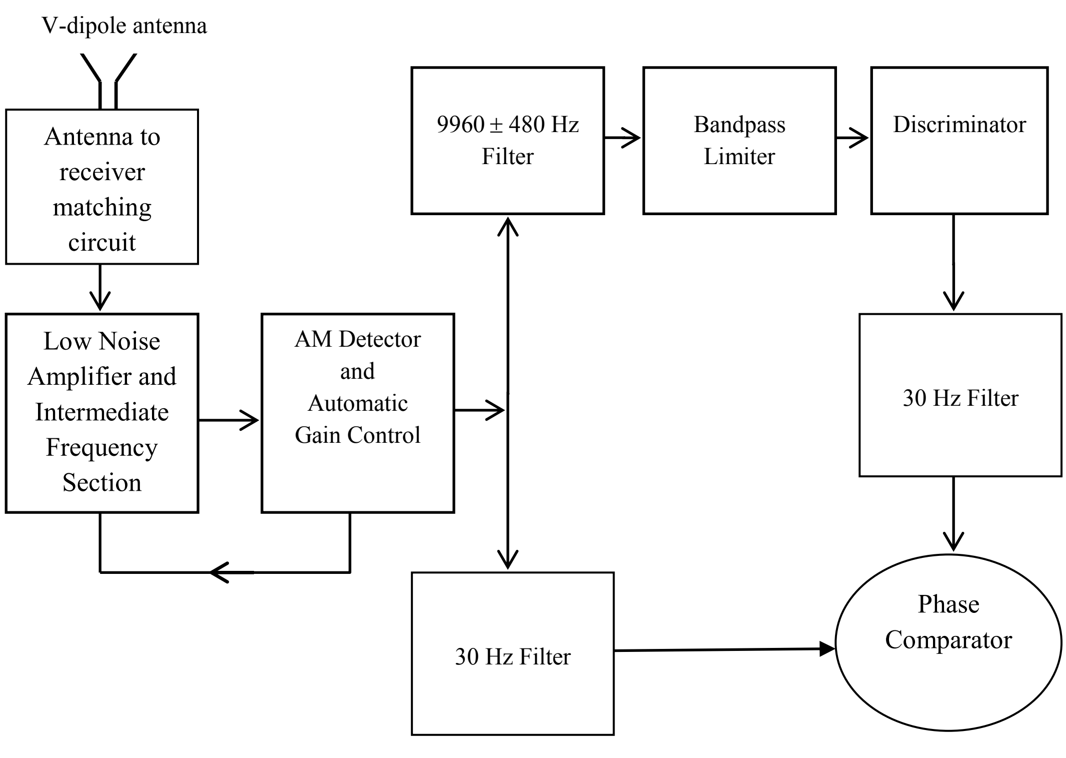

Figure 2-3. CVOR receiver block diagram (Voice and station I.D circuitry are not shown). Figure was redrawn and adapted from [3, 9].

2.1.2 Doppler VHF Omni-directional Range (DVOR) System. The AM of the CVOR variable signal on the main carrier makes it susceptible to distortion by multipath from structures (e.g., buildings etc.) and the local terrain, etc. [3, 8]. The DVOR system employs a wide aperture array to reduce the influence of siting effects on its performance [3, 8, 13, 15]. Moreover by frequency modulating the variable signal on a 9.96 KHz sub-carrier, the threshold enhancement of the FM receiver portion of the airborne receiver can be used to limit the effect of RF interference on the variable signal [14]. The DVOR system operates in the same frequency band as the CVOR system.

The DVOR ground station consists of a circular array of about 50 antennas, and a single antenna located at the center of the circular array [3, 8, 13, 15]. The center antenna "is driven" [8] at the main DVOR system RF carrier frequency (f_c). The RF carrier is amplitude modulated by a Morse code identification signal, and a 30 Hz signal, and has an isotropic radiation pattern in the azimuth plane. Hence the phase of the 30 Hz AM on the RF carrier is constant irrespective of the direction of observation relative to the DVOR ground station [13]. In the DVOR system, this 30 Hz AM on the carrier is thus referred to as the *reference signal*. The circular array "is driven" [8] at an RF that is 9960 Hz higher or lower than the main DVOR system RF carrier [3, 8, 13, 15]. The circular array is scanned electronically at a 30 Hz rate to simulate a rotating antenna [3, 8, 13, 15].

Consider Figure 2-4 which a top-view illustration of a DVOR ground station antenna array.

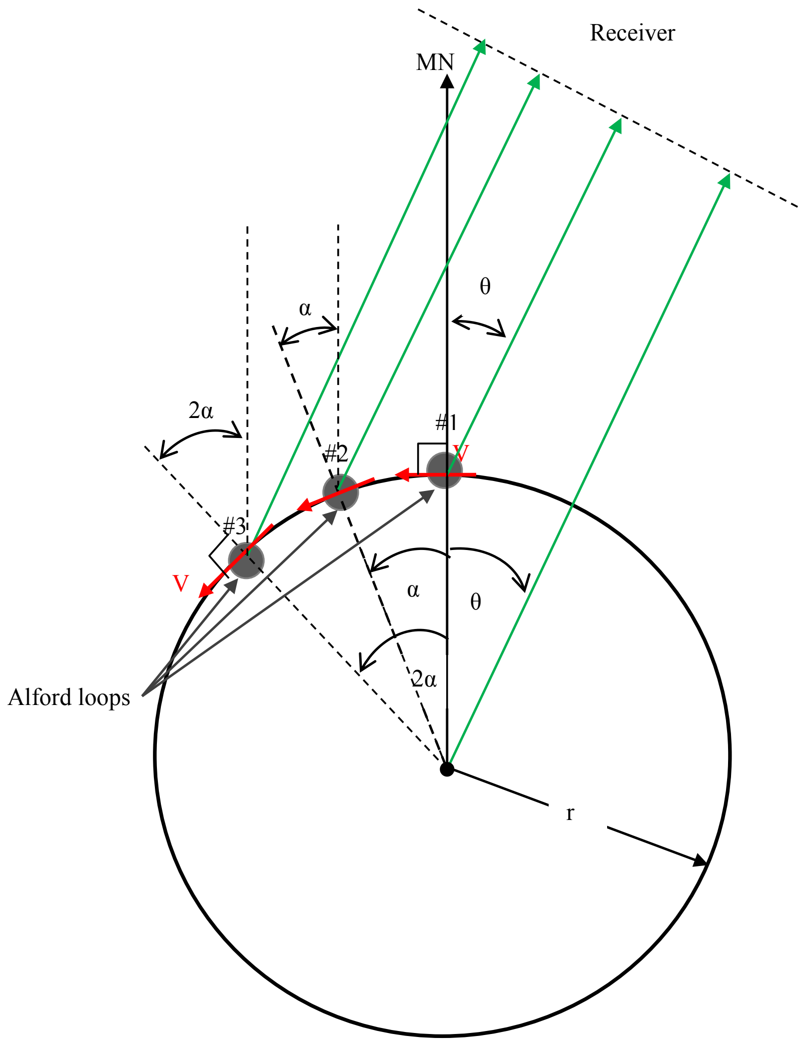

Figure 2-4. Operational Principle of DVOR Configuration I.

Alford loops #1, #2, #3 etc. are fed sequentially with an fc ± 9960 Hz RF signal. The feed process in the DVOR is by means of a distributor unit. The distributor has an arm that rotates at 1800 revolutions per minute (rpm). When the distributor arm is aligned with the feed point of an Alford loop (say #2 in Figure 2-4), the feed arm excites the Alford loop (#2) with maximum sideband RF while #1 and #3 receive no RF. As the distributor arm progresses counterclockwise away from the Alford loop (#2), the RF supplied to the next antenna on its path (#3) increases gradually while that supplied to previous Alford loop (#2) falls gradually. Maximum RF is supplied to #3 when the distributor arm is aligned with #3 at which point no RF is supplied to #2. A so-called *blending function* controls the exact amount of RF supplied to an Alford loop of the DVOR antenna array as a function of the position of the arm of the distributor. [13, 15]

The operation of the DVOR system is based on the Doppler Effect. As the array is scanned towards an airborne receiver a positive Doppler shift will be observed in the receiver. Conversely as the array is scanned away from the receiver a negative Doppler shift will be observed in the receiver. This effect produces a 30 Hz FM on the sideband signal. The phase of this 30 Hz FM varies with the bearing of the receiver from the DVOR ground station. Thus this 30 Hz FM signal on the sideband signal is called the *variable signal*. The phase lag of the 30 Hz FM variable signal from the 30 Hz AM reference signal is used to calculate the bearing of the receiver from the DVOR ground station relative to MN. In the absence of any error, this phase lag is exactly equal to the true bearing of the receiver/aircraft from the DVOR ground station. [13, 15]

The mathematical development of the generation of the 30 Hz FM signal as given in [8] is as follows: Consider the DVOR antenna array, and receiver shown in Figure 2-4. The scan rate of 30 revolutions per second (rps) simulates an antenna moving at velocity (V) such that

$$V = 30r \text{ [m/s]} \qquad (2\text{-}3)$$

Where:

r = radius of antenna array, [meters]

The effective component of the velocities in the direction of the receiver/aircraft for Alford loops #1, #2, #3 etc. in Figure 2-3 are given by:

$V_{s,1} = V\cos(0 + \theta)$, [m/s]

$V_{s,2} = V\cos(1\alpha + \theta)$, [m/s]

$V_{s,3} = V\cos(2\alpha + \theta)$, [m/s]

.
.
.

$V_{s,50} = V\cos(49\alpha + \theta)$, [m/s]

Or generally as:

$V_{s,i} = V\cos([i-1]\alpha + \theta)$, [m/s] (2-4)

Where:

$i = 1, 2, 3\ldots N$

N = number of antennas in the circular array

θ = bearing of aircraft (measured clockwise from MN) from DVOR station, [degrees]

The instantaneous angular position (α) of the "rotating antenna" (Alford loops #1, #2, #3 etc.) is given by the product of the angular velocity (scan rate of DVOR antenna array) i.e. 30 rps, and the instantaneous times of excitation;

$\alpha = 2\pi\,(30)\,(\Delta t)$, [rad]

$2\alpha = 2\pi\,(30)\,(2\Delta t)$, [rad]

Δt = time step between excitation of antennas of array, [seconds] given by,

$\Delta t = 1/\,(30 \mathrm{x} N)$

The Doppler frequency shifts ($\Delta f_{s,i}$) associated with the velocities in (2-4) are given by

$\Delta f_{s,i} = V_{s,i} / \lambda$, [Hz] where antenna index i = 1, 2… N (2-5)

Given that the circular array is excited with an RF of f_u Hz, the frequency modulated f_u can be expressed as,

$s[i] = \cos(2\pi(f_u + \Delta f_{s,i})[(i-1)\Delta t])$ i = 1, 2 ,…, N (2-6)

The subscript "u" in f_u is used in reference to the fact that f_u is the frequency of an upper sideband (AM) signal fed into the circular antenna array of the DVOR ground station. Thus the bearing of the aircraft (θ) is the phase of the FM on f_u. Note that a lower sideband of the AM signal could also be used. A few points about the DVOR system are stated below.

1. The bearing of the receiver aircraft is computed as the difference between the phases of the 30 Hz AM reference signal and the 30 Hz FM variable signal.
2. However as stated earlier and as can be inferred from the mathematical development above, in the absence of any error, the bearing of the receiver/aircraft is equal to the phase of the 30 Hz FM variable signal.
3. From 1 and 2 above, it can be deduced that phase of the 30 Hz AM reference signal is zero.

The analysis of the DVOR ground station in this thesis (new OUNPPM) is based on an alternative development given in [13]. Consider the DVOR antenna array shown in Figure 2-5.

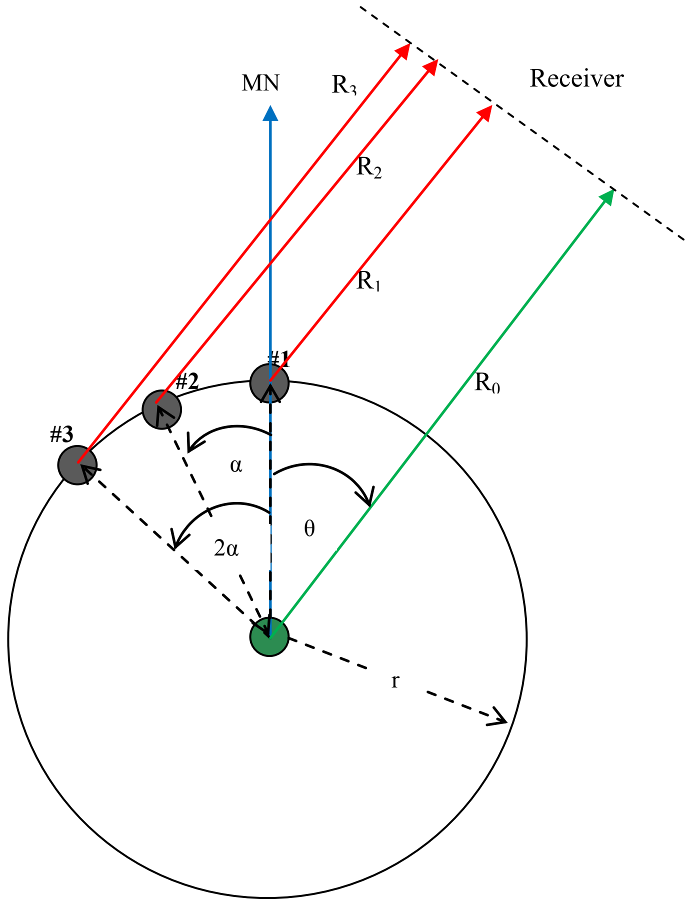

Figure 2-5. Operational Principle of DVOR Configuration II.

For the purpose of this analysis, the sideband signal that arrives at the receiver from the circular antenna array (#1, #2, etc. in Figure 2-5) can be expressed as

$s(t) = A(t)\cos[\omega_u (t-\Delta t)]$, [V] (2-7)

Where:

$A(t)$ = Amplitude of signal, [V]

Δt = transit time of signal from antenna to receiver [seconds]

$\omega_u = 2\pi f_u$, [rad/s]

$f_u = f + 9960$ Hz

Where:

$f = 108.00$ MHz to 117.95 MHz

Re-expressing (2-7) in discrete form,

$s[i] = A[i]\cos(\omega_u t - \omega_u \Delta t_i)$ (2-8)

Where:

i = index of sideband antenna (i.e, $i = 1, 2, 3, \ldots, N$)

$\Delta t_i = R_i/c$, [s] (2-9)

Where:

R_i = Distance from antenna "i" to receiver antenna

c = free-space propagation constant = 3e8 m/s

$\omega_u \Delta t_i = 2\pi f_u (R_i/c) = kR_i$, [rad] (2-10)

Where:

k = Wave number (i.e., phase constant), [rad/m]

The ranges of antennas #1, #2, etc. from the receiver are given by

$R_1 = R_0 - r\cos(\theta)$, [meters]

$R_2 = R_0 - r\cos(\alpha + \theta)$, [meters]

$R_3 = R_0 - r\cos(2\alpha + \theta)$, [meters]

Or generally as:

$R_i = R_0 - r\cos([i-1]\alpha + \theta)$, [meters] (2-11)

Where:

R_0 = Distance from center of the array (center antenna) to the receiver.

Substituting (2-10) and (2-11) into (2-8),

$s[i] = A[i]\cos(\omega_u [i-1]\Delta t - k[R_0 - r\cos([i-1]\alpha + \theta)])$ (2-12)

If the antennas (#1, #2, #3 etc.) shown in Figure 2-3 are excited starting at #1, then

$\alpha = \omega_m \Delta t$, [rad] (2-13)

$\omega_m = 2\pi (30)$, [rad/s] (2-14)

Δt = time step between excitation of sideband antennas = 1/ (30N)

Where:

N= number of sideband antennas.

By substituting (2-13) and (2-14) into (2-12) and expressing as a continuous signal,

$s[t] = A[t]\cos(\omega_u t - k[R_0 - r\cos(\omega_m t + \theta)])$ (2-15)

From (2-15), and similar to the earlier development, the DVOR variable signal is a 30 Hz FM on the sideband. The phase (θ) of this 30 Hz FM tone is equal to the bearing of the receiver from the station.

A CVOR receiver is used to process the DVOR signal [3, 8, 13]. The DVOR signal must therefore be similar to the CVOR signal as given in (2-1). The following properties of the DVOR system ground station ensure this compatibility.

1) The circular sideband antenna array has a radius of approximately 22 ft. in order that a maximum frequency deviation of ± 480 Hz is produced in the DVOR system FM signal as with the CVOR signal [8, 13].
2) In the CVOR system bearing is computed as the phase lag of variable signal from the reference signal; therefore the DVOR sideband array is scanned in the counterclockwise sense since the 30 Hz AM and 30 Hz FM have interchanged roles in the DVOR. [13]

The type of DVOR described above is referred to as the Single Sideband (SSB) DVOR. This is because only one sideband component is supplied to the sideband antennas.

The antenna array structure of the DVOR introduces errors in the bearings computed by the airborne receiver. As can be observed in of Figure 2-5 the sideband RF from the different sideband antennas traverse over different lengths of counterpoise. Whilst some sideband antennas will have a large counterpoise between them and the aircraft for a reflection from the counterpoise, only reflections from the ground for some other sideband antennas will arrive at the aircraft/receiver. Therefore a sideband signal of varying amplitude will be detected at the receiver. This effect, known as the "counterpoise eccentricity effect" [15] impresses a 30 Hz AM on the sideband signal. This 30 Hz AM intermodulates the DVOR reference signal leading to significant bearing errors. [13, 15]

In order to minimize the SSB DVOR counterpoise error, a variant of the DVOR namely the Double Sideband (DSB) DVOR simultaneously scans two (2) sidebands at diametrically opposite antennas of the circular antenna array [8, 15]. This scheme almost nulls the 30 Hz AM due to the counterpoise effect.

2.1.3 Alford Loop Field Pattern. Figure 2-6 illustrates the radiation pattern of an Alford loop in principal planes (x-z and y-z).

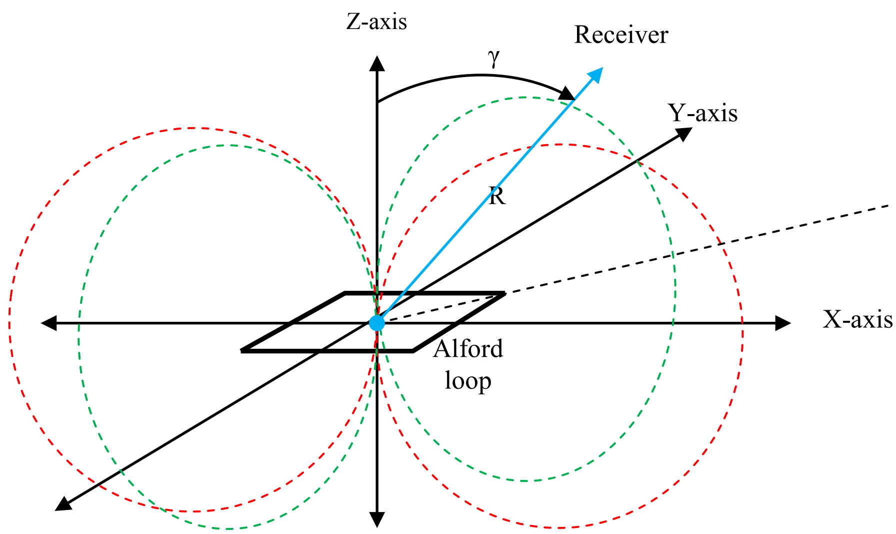

Figure 2-6. Alford loop antenna pattern. This Figure was adapted from [11].

For an Alford loop located in the X-Y plane as shown in Figure 2-6, its pattern is omni-directional in the azimuth plane. From [11] at a wavelength (λ) of at least eight times the length (l) of the side of the Alford loop, the intensity of the E-field radiated from the Alford loop at an observation point (in the far field) R distance units from the center of the loop can be approximated by,

$$E = 8I_0\pi^2 l^2 \sin\gamma / (R\lambda) \tag{2-16}$$

Where:

I_0 = Excitation current [A]

γ = Zenith angle of observation point (see Figure 2-6).

R = Range of observation point from center of Alford loop (see Figure 2-6).

2.2 High Frequency Electromagnetic Scattering Techniques

2.2.1 Physical Optics (PO). PO is a technique employed in determining the field that will be received at an observation point when a high frequency source radiates with a scatterer (e.g., building, etc.) in its field-of-view. The total field at an observation point is calculated as the sum of the field which arrives at the observation point directly, and a scattered field which is determined by applying radiation integrals to the currents induced on the scatterer surface by the source field. The induced currents are computed by assuming the scatterer to be a perfect electrical conductor (PEC) and infinite in size. This approximation introduces large errors in regions where the contribution of another field, (e.g. the diffracted field contribution not modeled by PO theory to the total field is significant). Another situation where PO modeling is limited is where PO predicts zero fields in regions shadowed by the scatterer. Fields at only observation points not shadowed by the scatterer can be determined using PO. PO has an advantage of been applicable in determining fields at other directions apart from those along directions of specified by the law of reflection. [16]

PO was applied in computing the multipath fields (i.e., ray 11) in the OUNPPM as shown in Figure 1-2.

2.2.2 Physical Theory of Diffraction (PTD). PTD is a high frequency electromagnetic scattering analysis technique that corrects for the inaccuracies inherent in the PO method. This correction is achieved by refining the PO formulation of the currents induced on the scatterer surface from which the scattered fields are computed. The PTD induced fields are decomposed into a uniform field which is computed as the approximate PO field which will be induced in a plane of infinite extent tangent to the illuminated face of the scatterer, and a non-uniform field to account for the deviation of the surface of the scattering object from the flat infinite tangent plane assumed in computing the uniform field [17]. PTD was not applied in the OUNPPM.

2.2.3 Geometrical Optics (GO). In GO rays similar to those used to describe the propagation of light are used to characterize the high-frequency electromagnetic field from a source received at an observation point. This section is somewhat detailed because the geometrical theory of diffraction and the uniform geometrical theory of diffraction which are discussed in sections 2.3.4 and 2.3.5 are both extensions of GO. In GO an incident ray defines the line-of-sight (LOS) field from the source to the observation point. In cases where the source illuminates a scatterer additional rays namely reflected, refracted, and transmitted rays are included in the total field observed at the field point to account for effects introduced by the interaction between the source field and the interface between the medium through which the electromagnetic field is propagating and the scatterer. [18]

Each GO ray is oriented perpendicular to the wave front of the electromagnetic field e.g., direct, reflected, etc. that it represents, and passes through the point on an infinitesimal area on the wave front from which the “dominate contribution” to radiated field emanates [16]. The GO ray traces paths dictated by Fermat’s Principle which states that each GO ray will traverse through the path from the source to the field point that optimizes (minimizes) its transit time [18]. The laws of reflection, refraction, and transmission at the interface between two media are derived from this form of Fermat's Principle [16, 18].

Characterization of the amplitude of a GO field/ray at an observation point is achieved by considering the bundle of rays which surround the wave front whose "energy transport" is directed along the central GO ray labeled "Paraxial ray" in Figure 2-7. From the principle of energy conservation, a field of constant energy propagates along such a ray-tube. The intensity of the radiated field at a point in space is therefore the ratio of this constant energy flowing through the ray tube and the cross-section area (wave front area) at the desired observation point. With the field intensity on a reference wave front (W_0) known, geometrical relations between the area of W_0 and the wave front (W_s) at the observation point (P in Figure 2-7), and the distance of separation between the wave fronts can be applied to determine the field intensity at the observation point P. [16, 18, 19]

The electric field intensity at P is given [16, 18, 19] by

$$|\mathbf{E}(P)| = |\mathbf{E}(O)|\sqrt{\frac{\rho_1\rho_2}{(\rho_1 + s)(\rho_2 + s)}} \tag{2-17}$$

Where:

|E (O)| = Field intensity on reference wave front, [V/m]

ρ_1 = Principal radius of curvature of the reference wave front in first principal plane, [m]

ρ_2 = Principal radius of curvature of the reference wave front in second principal plane, [m]

s = Distance of P from reference wave front, [m]

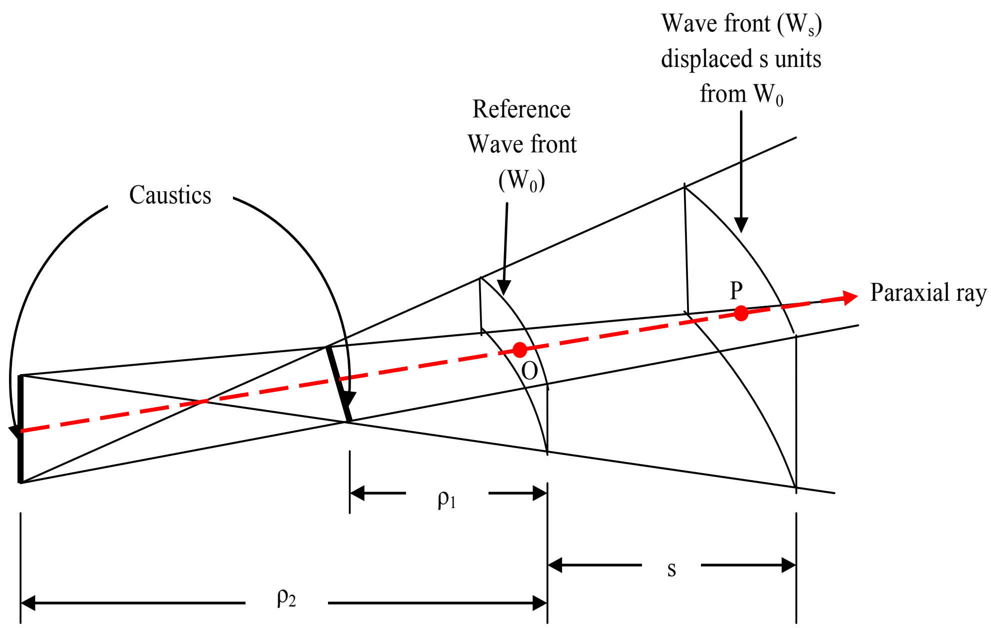

Figure 2-7. Ray-tube (Redrawn from [16]).

On the lines labeled caustics in Figure 2-7, GO predicts infinite field intensities and therefore GO cannot be used on such lines [16, 18, 19]. The phase of the GO ray/field at an observation point is equal to the product of the wave number in the medium of propagation, and the distance of the observation point from the point where the phase is referenced to zero. [16, 18, 19]

Determining the GO reflected field at an observation point is a 4-step process. From [16, 18, 19] the steps are as follows:

1) First, the point of reflection on the scatterer is determined by applying the law of reflection.

2) Next, the electromagnetic field (amplitude and phase) incident on the reflection point is determined by applying the concept of constant energy in a ray bundle with the electromagnetic field at the source being the reference.
3) Third, the complex reflection coefficient derived by imposing boundary conditions at the interface is calculated and then multiplied by the incident field to produce the reflected field exiting the reflection point. The reflection coefficient depends on the properties of the scatterer in the neighborhood of the point of reflection.
4) Finally the concept of constant energy in a ray tube is applied, with the reflected field in step 3 being the reference to obtain the field at the observation point.

As illustrated in Figure 2-8 and Figure 2-9, when a high frequency field illuminates a finite wedge or a wedge with a curved surface, the field distribution around the wedge is partitioned into regions illuminated by different GO rays or ray combinations [16, 18]. In the regions labeled "shadow region" in Figure 2-8 and Figure 2-9, GO predicts a zero field [16, 18]. These regions are said to be completely shadowed. It can also be inferred from the ray-tube amplitude characterization used in GO, that discontinuities will exist across the boundaries that separate the shadow and lit regions [16].

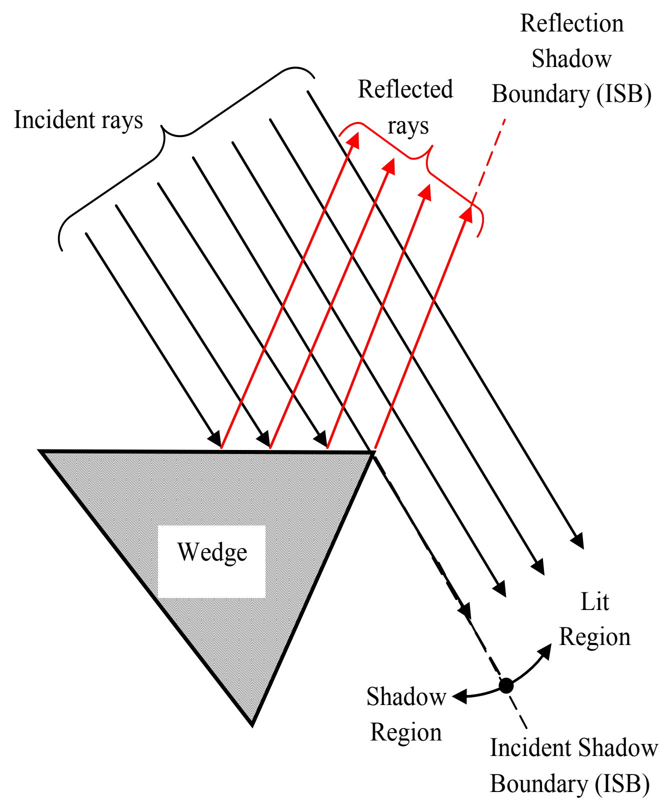

Figure 2-8. GO illumination of a straight finite wedge. Figure was redrawn from [16].

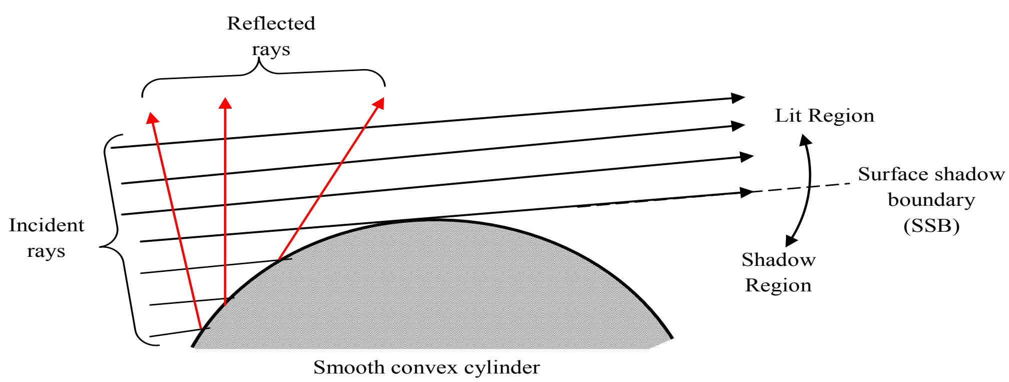

Figure 2-9. GO illumination of a curved surface (Figure was redrawn from [16])

In both the old OUNPPM and the new OUNPPM, the fields represented by rays 1, 2, 5, 6, 7, and 10 (i.e., all rays except those diffracted from edge) in Figure 1-1 were modeled using GO. A detailed description of the steps followed in computing the GO field is given in Chapter 3.

2.2.4 Geometrical Theory of Diffraction (GTD). For illumination of an infinite scatterer by a high-frequency electromagnetic (EM) source, the GO approximation produces an accurate prediction of the total field at any observation point [16, 18]. However, GO fails to account for effects that result when a high-frequency field illuminates a finite scatterer [16, 18]. For instance, GO's prediction of a zero field in the shadow zones (shown in Figure 2-8 and Figure 2-9) is inaccurate. Joseph Keller improved the accuracy of GO by incorporating diffracted rays to account for the diffracted field that is known to exist everywhere around a finite wedge which contains an edge or vertex when it is illuminated by an EM field [16, 18, 19]. Diffracted fields are also produced when a high frequency EM field is incident on a curved surface or any kind of edge or surface discontinuity. The underlying theory known as the Geometrical Theory of Diffraction (GTD) defines the amplitude and phase of the diffracted ray at an observation point, and the path it (diffracted ray) traces from the source to the observation point [16, 18, 19]. The GTD field at an observation point is the sum of the GO field and the contributions from all the diffracted rays predicted by GTD [16, 18, 19].

The points on the scatterer from where the diffracted rays emanate are determined by applying Keller's Law of Diffraction which is derived from Fermat's Principle. For an edge, Keller's Law states that the angle of incidence between the incident ray and the tangent at the point of diffraction is equal to the angle of diffraction between diffracted ray and the tangent to the edge at the diffraction point. The angle of incidence is measured in the plane that contains the incident ray and the tangent to the edge at the point of diffraction whilst the angle of diffraction is measured in the plane that contains the diffracted ray and the tangent to the edge at the point of diffraction. For a convex surface the angle of incidence and angle of diffraction are referenced from the tangential plane to the surface at the point of diffraction. [16, 18, 19]

Figures 2-10 illustrates Keller's Law. For normal incidence on a straight edge a disk shaped envelope of diffracted rays results whilst oblique incidence produces a conical family of diffracted rays. [16, 18, 19]

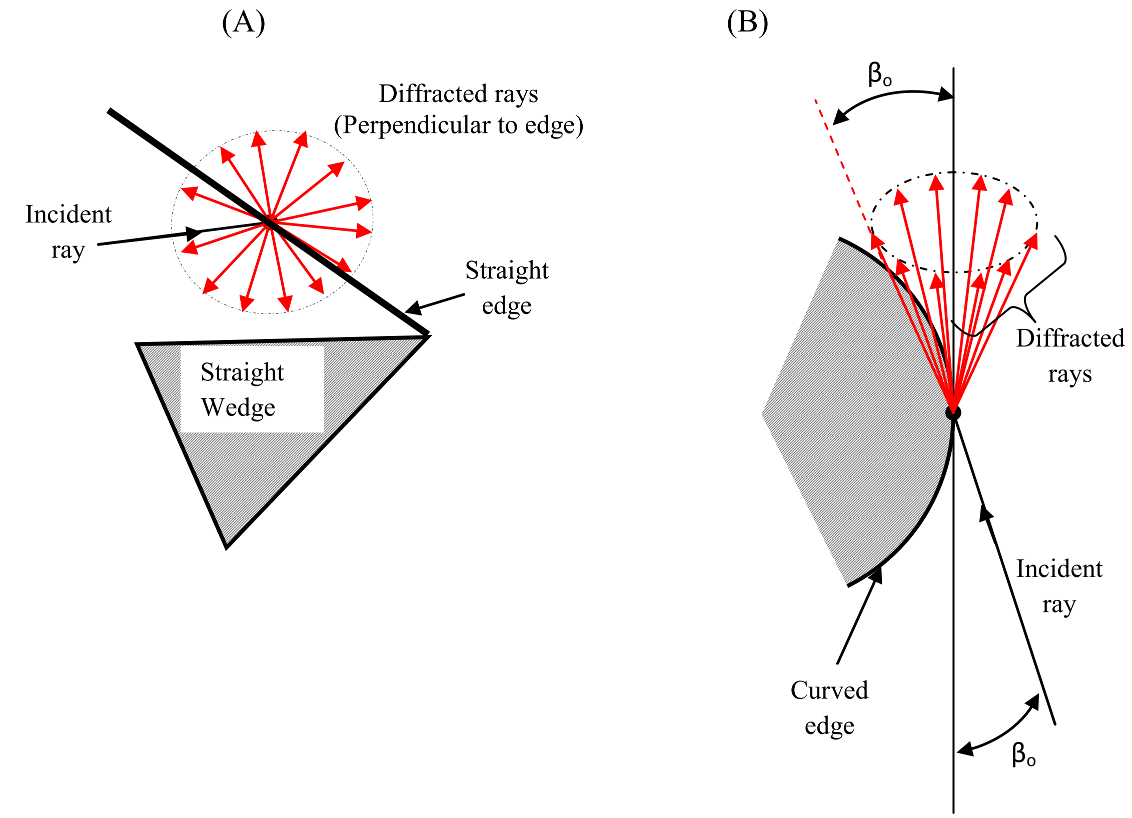

Figure 2-10. Illustration of Keller's Law for normal incidence (A) and oblique incidence (B). The figures were redrawn from [15].

To determine the diffracted field corresponding to a single diffracted ray, the EM field incident on the diffraction point is multiplied by a diffraction coefficient to produce the field exiting the diffraction point. The same energy conservation in a ray-tube principle described in the section on GO is applied to the diffracted field exiting the diffraction point to determine the diffracted field at the desired observation point. GTD's reliance on the ray-tube principle implies that just as with GO, GTD fails at observation points that coincide with singular points/lines (caustics) along the ray-tube. The phase of a diffracted ray at the observation point is equal to the sum of the phase value at the reference (diffraction point) and the product of the wave number and range of the observation point from the diffraction point. [16, 18, 19]

In the transition regions around the reflection shadow boundary (RSB) and incidence shadow boundary (ISB), GTD's prediction of the diffracted field is inaccurate. The RSB and ISB are shown on Figure 2-11 for a plane wave incidence on a straight wedge. In the GTD/UTD community the faces of the wedge are "arbitrarily" referred to as o-face and n-face so that specific reference can be made to either face without resort to verbose descriptions e.g., to distinguish between the illuminated and non-illuminated faces of the wedge. At directions/angles of observation (referenced from the o-face of the wedge) greater than the RSB (ray B in Figure 2-11), no reflected ray from the illuminated face of the wedge exists. Similarly at directions of observation (referenced from the face of the wedge) greater than the ISB (ray C in Figure 2-11), neither a reflected nor a direct ray from the source exists. [16, 18, 19]

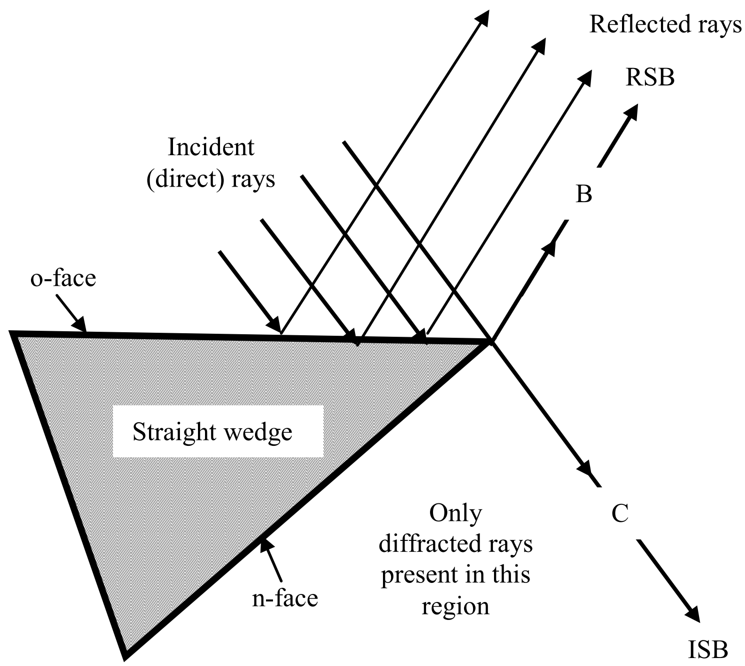

Figure 2-11. RSB and ISB for plane wave incidence on a straight wedge.

GTD is discontinuous across the RSB and ISB. This defect is due to the fact that GTD diffraction coefficients were derived by comparing ray-form diffraction formulations with expansions of the exact diffraction solutions that are themselves invalid in these regions. [18, 19]

The uniform geometrical theory of diffraction (UTD), which is an improvement over GTD which is ultimately used in the OUNPPM, is described next.

2.2.5 Uniform Geometrical Theory of Diffraction (UTD). The UTD field for a high frequency source radiating with a scatterer in its field-of-view is the sum of the GO field, and the diffracted field predicted by UTD. However unlike GTD, UTD yields accurate field predictions even in the transition regions. The path traced by the UTD diffracted ray is also defined by Keller's Law of Edge Diffraction. UTD also characterizes the amplitude of its diffracted ray/field by employing the principle of energy conservation in a ray-tube, and therefore also fails at caustics. The phase of the diffracted field at an observation point is the product of the wave number and the range of the observation point from the phase reference. Unlike GTD, the UTD diffraction coefficient incorporates a transition function. It is this function that bounds the UTD field in the transition regions, and also enforces continuity across the RSB and ISB. [16, 18, 20]

The UTD model can be either 2-D or 3-D depending on the configuration or scenario being modeled. The old CVOR/DVOR model of the old OUNPPM is based on 2-D UTD, and the new CVOR/DVOR model of the new OUNPPM (developed in this thesis) is based on 3-D UTD.

2.2.5.1 2-D UTD. For a UTD edge model to qualify as a valid 2-D model the following conditions must hold:

1) The magnitude of the field from the source e.g., antenna, must be constant along the entire length of the edge [18].
2) The phase of the source field must also be constant along the edge [18].
3) Polarization of the source field must be parallel to the edge [18].

In the old CVOR/DVOR model of the old OUNPPM, the CVOR/DVOR ground station was modeled as a single point source centered above a circular PEC counterpoise. Thus conditions 1 and 2 above are satisfied. Since the CVOR/DVOR antenna is horizontally polarized condition 3 is also satisfied, and thus applying 2-D UTD in the old CVOR/DVOR model was justifiable. However as mentioned hitherto, the CVOR/DVOR ground station model used in the old OUNPPM was an oversimplification of the actual CVOR/DVOR ground station configuration. Figure 2-12 shows an example 2-D UTD problem of normal incidence of a cylindrical wave on a straight edge. In Figure 2-12 the edge is along the Z-axis and it is assumed the wedge (shaded region) is infinite along the Z-axis (i.e., at Q_i going into the page). The regions around the ISB and RSB are called transition regions.

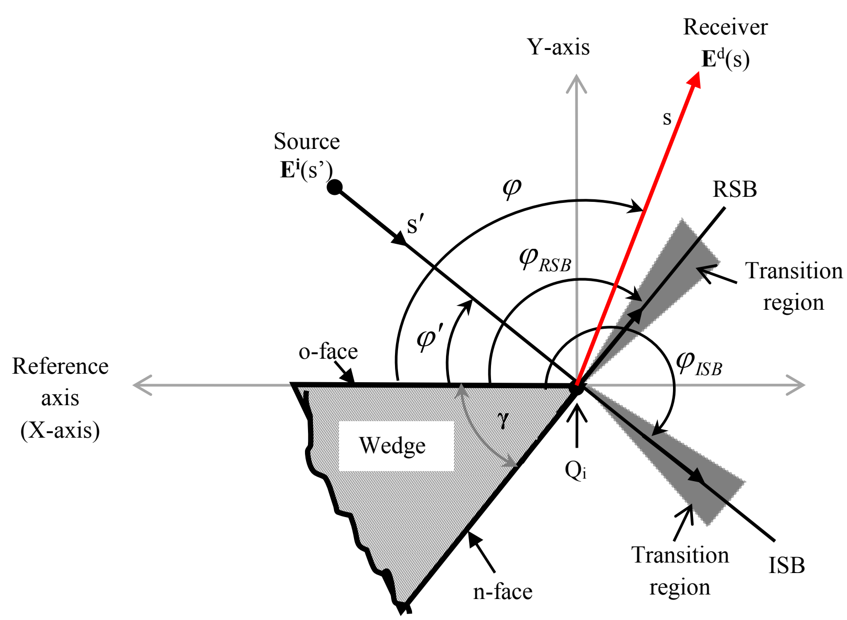

Figure 2-12. 2-D diffraction by a wedge (This figure was redrawn from [18]).

From [18] the diffracted field from point Q_i for the case illustrated in Figure 2-12 is given by

$$E^{d}(s) = E^{i}(Q_{i}) D_{s,h} \frac{e^{-jks}}{\sqrt{s}}, \text{ [V/m]} \tag{2-18}$$

Where:

$E^{d}(Q_{i})$ = incident field at point of diffraction (Q_i), [V/m]

s = range of receiver/field point from diffraction point (Q_i), [meters]

$D_{s,\,h}$ = soft/hard scalar diffraction coefficient, [meters$^{0.5}$]

The 2-D (scalar) UTD diffraction coefficient assuming incidence on a PEC edge is given [18] by $D_{s,h}(L^{i}, L^{ro}, L^{m}, \varphi, \varphi', n) = D_{1} + D_{2} \pm (D_{3} + D_{4})$, [meters$^{0.5}$] (2-19)

Where the "+" and "$-$" of $\pm$ above are used for vertical (hard) polarization and horizontal (soft) polarization respectively, and

$$D_{1} = \frac{-e^{j\pi/4}}{2n\sqrt{2\pi}\sqrt{k}} \cot\left[\frac{\pi + (\varphi - \varphi')}{2n}\right] F\left[kL^{i} a^{+}(\varphi - \varphi')\right], \text{ [meters}^{0.5}\text{]}$$

$$D_{2} = \frac{-e^{j\pi/4}}{2n\sqrt{2\pi}\sqrt{k}} \cot\left[\frac{\pi - (\varphi - \varphi')}{2n}\right] F\left[kL^{i} a^{-}(\varphi - \varphi')\right], \text{ [meters}^{0.5}\text{]}$$

$$D_{3} = \frac{-e^{j\pi/4}}{2n\sqrt{2\pi}\sqrt{k}} \cot\left[\frac{\pi + (\varphi - \varphi')}{2n}\right] F\left[kL^{m} a^{+}(\varphi - \varphi')\right], \text{ [meters}^{0.5}\text{]}$$

$$D_{4} = \frac{-e^{j\pi/4}}{2n\sqrt{2\pi}\sqrt{k}} \cot\left[\frac{\pi - (\varphi - \varphi')}{2n}\right] F\left[kL^{ro} a^{-}(\varphi - \varphi')\right], \text{ [meters}^{0.5}\text{]}$$

Where:

φ' = angle between the incident ray and the o-face (Figure 2-12), [rad]

φ = angle between the diffracted ray and the o-face (Figure 2-12), [rad]

k = wave number in medium of propagation, [rad/m]

Where from [16, 18, 20]

n = wedge factor given by $\gamma = (2\text{-}n)\,\pi$, where γ is the interior angle between the o-face and n-face of the wedge.

F[x] = transition function for real argument x given by

$$F[x] = 2j\left|\sqrt{x}\right|e^{jx}\int_{\left|\sqrt{x}\right|}^{\infty} e^{-j\tau^2}\,d\tau$$

(2-20)

$$a^{\pm}(\varphi \pm \varphi') = 2\cos^2\left(\frac{2N^{\pm}\pi n \pm (\varphi \pm \varphi')}{2}\right)$$

(2-21)

Where:

$$N^{\pm} = \text{INTEGER}\left(\frac{\pm\pi + (\varphi \pm \varphi')}{2n}\right) \qquad (2\text{-}22)$$

The INTEGER function in $N^{\pm}$ above is to the closest integer.

For the present case of cylindrical wave incidence on a straight edge, the *distance parameters* L^{i}, L^{ro}, and L^{rn} are given [18] by

$L^{i} = ss' / (s+s')$, [meters] (2-23)

$L^{ro,\,rn} = \rho^{ro,\,rn}\, s / (\rho^{ro,\,rn} + s)$, [meters]

(2-24)

Where:

s = range from diffraction point to observation point.

s′ = distance from source point to diffraction point.

$\rho^{ro,\,rn} = (a_{o,\,n}\cos\theta_{o,\,n}\, s') / (a_{o,\,n}\cos\theta_{o,\,n} + 2s')$, [meters]

Where:

$a_{o,\,n}$= “radii of curvature of o-face and n-face, respectively, at the point of diffraction”[18], [meters].

$\theta_{o,\,n}$= angles between the incident ray and the normal at the diffraction point on the o- and n- faces respectively.

2.2.5.2 3-D UTD. For oblique incidence on an edge, and for incidence on a curved edge where the source of the wave is not located on the axis of symmetry of the curved edge, that is if such an axis exists for the edge in question, or when properties of the incident wave are such that its phase and amplitude are not constant along the edge, 3-D UTD should be applied [18]. Apart from the reference antenna of the DVOR ground station which is centered above the counterpoise, and thus could be modeled via 2-D UTD, all other antennas of actual CVOR/DVOR ground stations are offset from the center of the counterpoise, and thus can only be accurately modeled using 3-D UTD. In the new CVOR/DVOR model of the new OUNPPM, 3-D UTD has been applied to model the CVOR/DVOR ground station. In 3-D UTD modeling, it is more appropriate to adopt a “ray-fixed coordinate system” [18] in which planes parallel and perpendicular to the incident and diffracted rays are defined [16, 18, 20]. The ray-fixed coordinate system enables analysis for arbitrary incidence aspect angles and polarizations [18]. Figure 2-13 illustrates 3-D diffraction from a curved edge, and the important vectors of the ray-fixed coordinate system.

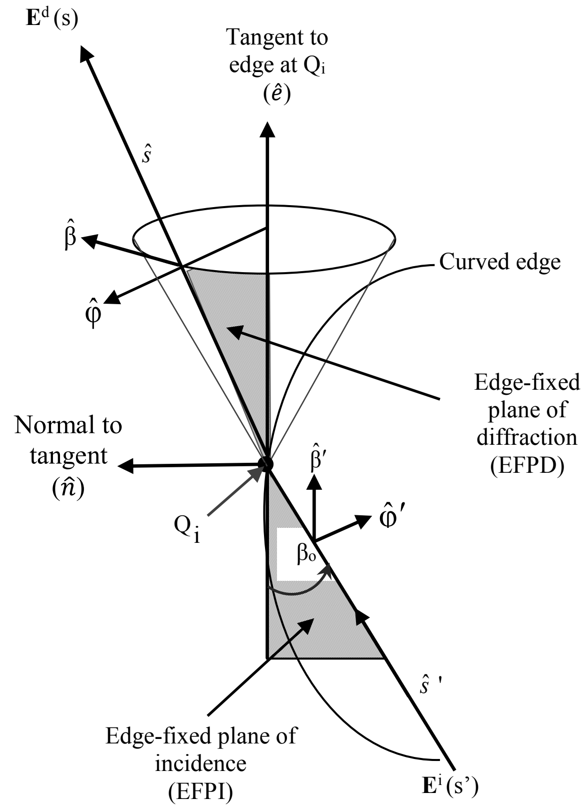

(A)

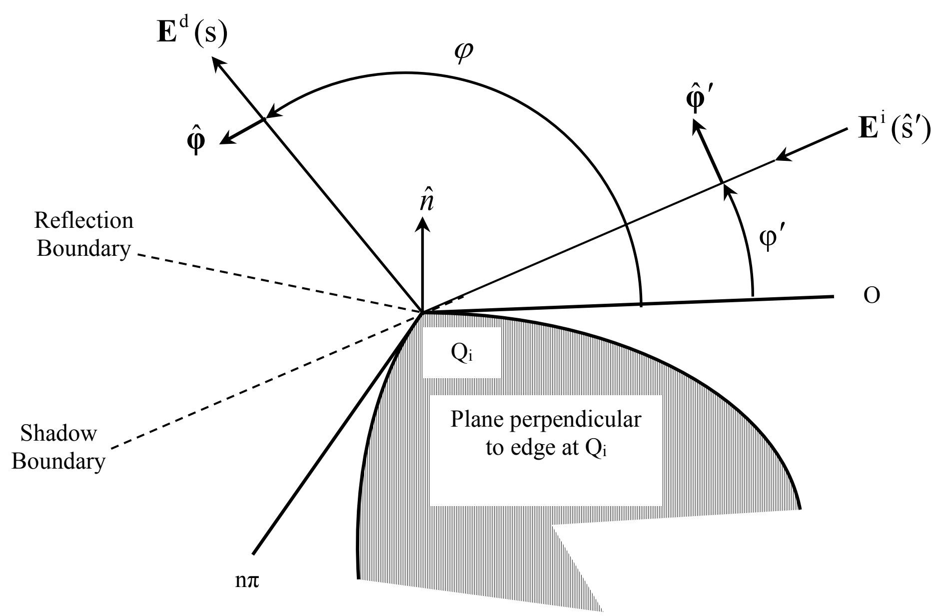

(B)

Figure 2-13. Oblique incidence on a curved edge (Figure was redrawn from [20]).

The definitions of some essential geometric planes in 3-D UTD scattering analysis as given in [16, 18, 20] and depicted in Figure 2-13 are as follows:

- Edge- fixed plane of incidence (EFPI): Plane in which the incident ray ($\hat{s}'$) at the diffraction point (Q_i) and tangent ($\hat{e}$) to the curved edge at the diffraction point are coplanar.
- Edge- fixed plane of diffraction (EFPD): Plane in which diffracted ray ($\hat{s}$) from Q_i and $\hat{e}$ are coplanar.
- Normal plane of incidence: Plane which contains the incident ray ($\hat{s}'$) and the normal ($\hat{n}$) to the edge at Q_i.
- Normal plane of diffraction: Plane which contains the diffracted ray ($\hat{s}$) and $\hat{n}$.

In Figure 2-13 the unit vectors $\hat{\boldsymbol{\varphi}}'$ and $\hat{\boldsymbol{\beta}}'$ are unit vectors perpendicular and parallel respectively to the EFPI whilst $\hat{\boldsymbol{\varphi}}$ and $\hat{\boldsymbol{\beta}}$ are the unit vectors perpendicular and parallel respectively the EFPD. The incident ray and the diffracted ray are represented in Figure 2-13 by $\hat{\mathbf{s}}'$ and $\hat{\mathbf{s}}$ respectively. The unit vectors $\hat{\mathbf{s}}', \hat{\boldsymbol{\beta}}', \hat{\boldsymbol{\varphi}}', \hat{\mathbf{s}}, \hat{\boldsymbol{\beta}}, \hat{\boldsymbol{\varphi}}$ define the ray-fixed coordinate system. The relations between the aforementioned unit vectors are given in [16, 18 and 20] by

$$\hat{\boldsymbol{\beta}}' = \hat{\mathbf{s}}' \times \hat{\boldsymbol{\varphi}}' \tag{2-25}$$

$$\hat{\boldsymbol{\beta}} = \hat{\mathbf{s}} \times \hat{\boldsymbol{\varphi}} \tag{2-26}$$

With the ray-fixed co-ordinate system defined, the **E**- field diffracted from the edge is given in [20] as,

$$\mathbf{E}^{\mathbf{d}}(\mathrm{s}) = \mathbf{E}^{\mathbf{i}}(\mathrm{Q}_{\mathrm{i}})\overline{\mathbf{D}}\sqrt{\frac{\rho}{\mathrm{s}(\rho+\mathrm{s})}}\mathrm{e}^{-\mathrm{jks}}, \quad [\mathrm{V/m}] \tag{2-27}$$

Where:

$\mathbf{E}^{i}(Q_i)$ = Incident **E**-field vector field at the diffraction point, [V/m]

$\overline{\mathbf{D}}$ = dyadic diffraction coefficient, [meters$^{0.5}$] and is given in [16, 18, 20] as

$$\overline{\mathbf{D}} = -\hat{\boldsymbol{\beta}}'\hat{\boldsymbol{\beta}}\, D_s - \hat{\boldsymbol{\varphi}}'\hat{\boldsymbol{\varphi}}\, D_h \tag{2-28}$$

The scalar soft and hard diffraction coefficients D_s and D_h are given in [16, 18, 20] by

$$D_{s,h}(\varphi,\varphi',\beta_o,n) =$$

$$\frac{-e^{-j\frac{\pi}{4}}}{2n\sqrt{2\pi}\sqrt{k}\sin\beta_o}\left\{\left[\cot\left(\frac{\pi+(\varphi-\varphi')}{2n}\right)F\left[kL^{i}a^{+}(\varphi-\varphi')\right]+\cot\left(\frac{\pi-(\varphi-\varphi')}{2n}\right)F\left[kL^{i}a^{-}(\varphi-\varphi')\right]\right]\right.$$

$$\pm$$

$$\left.\left[\cot\left(\frac{\pi+(\varphi+\varphi')}{2n}\right)F\left[kL^{ro}a^{+}(\varphi+\varphi')\right]+\cot\left(\frac{\pi-(\varphi+\varphi')}{2n}\right)F\left[kL^{m}a^{-}(\varphi+\varphi')\right]\right]\right\} \tag{2-29}$$

The $\sin\beta_o$ term included in the denominator of the common multiplier term in (2-29) is to account for arbitrary angles of incidence in the EFPI [18]. Thus in the 2-D UTD case $\sin\beta_o = 1$. The $a^{\pm}$ functions have the same definitions as in the 2-D UTD case as previously shown in (2-21). The distance parameters for the 3-D case must however be computed from their general forms given in [16] by

$$L^{i} = \frac{s(\rho_e^{i}+s)\rho_1^{i}\rho_2^{i}\sin^2\beta_o}{\rho_e^{i}(\rho_1^{i}+s)(\rho_2^{i}+s)}, \text{ [meters]} \tag{2-30}$$

$$L^{ro,m} = \frac{s(\rho_e^{ro,m}+s)\rho_1^{ro,m}\rho_2^{ro,m}\sin^2\beta_o}{\rho_e^{ro,m}(\rho_1^{ro,m}+s)(\rho_2^{ro,m}+s)}, \text{ [meters]} \tag{2-31}$$

Where:

ρ_e^i = radius of curvature of incident wave-front in EFPI, [m]

ρ_1^i = radius of curvature of the incident wave-front in EFPI, [m]

ρ_2^i = radius of curvature of the incident wave-front in plane normal to EFPI, [m]

$\rho_{1,2}^{ro,rn}$ = principle radii of curvature of reflected wave-front for o-face and n-face, [m]

s = distance from diffraction point to field point, [m]

β_o = angle of incidence in EFPI.

The caustic distance (ρ) in (2-27) is a measure of the displacement of the second caustic of the diffracted ray from the one at the diffraction point, and is reckoned positive in the direction opposite to the direction of propagation of the diffracted ray [18, 20]. The caustic distance (ρ) is given in [18, 20] by

$$\frac{1}{\rho} = \frac{1}{\rho_e^i} - \frac{\hat{n} \bullet (\hat{s}' - \hat{s})}{a \sin^2 \beta_o} \tag{2-32}$$

Where:

a = radius of curved edge at the point of diffraction, [m].

$\hat{n}$ = normal to edge at diffraction point. All other terms retain previous meanings.

As mentioned earlier 3-D UTD was applied in the new OUNPPM to model the fields from the CVOR/DVOR ground station to the receiver/aircraft and the scatterer. The 3-D UTD fields arriving at the scatterer are subsequently input into a PO scattering model which computes the field from the scatterer to the receiver/aircraft.

2.3.6 Method of Equivalent Currents (MEC). Although MEC was not implemented, it will be discussed briefly. The MEC extends the applicability of UTD to caustic regions. From [18], for diffraction by an edge of finite length, MEC achieves this capability through a 4-step process as follows:

1. First, an expression for the diffracted field that will be received at the desired observation point is formulated by applying radiation integrals to the line current (unknown) flowing through a hypothetical infinite line source placed along the edge from which the diffracted field emanates.

2. Next UTD is applied to determine the diffracted field at the desired observation point by assuming that the edge is of infinite length.

3. The expression in step 1 should be equal to the UTD-diffracted field computed in 2. Therefore, by equating the expression in step 1 with the diffracted field in step 2, the line current can be determined.

4. Finally the field diffracted from the finite edge can be computed by integrating the line current (determined in step 3) over the extent of the edge.

From [18] the equivalent electric, $\mathbf{I}^{\mathbf{e}}$ and magnetic, $\mathbf{I}^{\mathbf{m}}$ currents employed in determining the diffracted field for horizontal and vertical polarizations respectively can be expressed respectively as,

$$I^{e}(\zeta) = -\frac{\left(\hat{e}^{i} \bullet \hat{e}\right)}{Z\sin\beta_{o}} E^{i}(\zeta)\sqrt{\frac{8\pi}{k}}e^{-j\pi/4}D_{s}(\zeta) \tag{2-31}$$

$$I^{m}(\zeta) = -\frac{\hat{e}^{i} \bullet \left(\hat{e} \times \hat{s}'\right)}{\sin\beta_{o}} E^{i}(\zeta)\sqrt{\frac{8\pi}{k}}e^{-j\pi/4}D_{h}(\zeta) \tag{2-32}$$

Where:

$\hat{\mathbf{e}}^{\mathbf{i}}$, $\hat{\mathbf{e}}$ are the polarization unit vector and the vector parallel to the edge respectively. The $\mathbf{E}$-field incident on the edge is $\mathbf{E}^{\mathbf{i}}(\zeta)$ and Z is the intrinsic impedance in the medium of propagation.

$D_{s,h}(\zeta)$: = As given in (2-29)

MEC can only be applied at observation directions away from the transition zones [16]. It is recommended that in future improvement work on the OUNPPM, MEC should be applied in modeling the center antenna of the DVOR for observation directions close to the zenith (axis of counterpoise). In this axial region, caustics of the diffracted rays from the edge of the counterpoise occur, and thus UTD fails.

CHAPTER 3: DEVELOPMENT OF CVOR/DVOR ERROR MODEL

3.1 Structure of CVOR/DVOR Model

This chapter outlines the development of the CVOR ground station, DVOR ground station, and CVOR/DVOR receiver models. Modeling of the ground stations consists of determining the fields radiated by the ground stations' antennas using 3-D UTD. The composite 3-D UTD fields are processed by the CVOR/DVOR receiver models. The main output datum of interest from the CVOR/DVOR receiver is the bearing error. As a software tool, analysis techniques that allow the fast and accurate determination of the bearing error are employed in CVOR/DVOR receiver model. Thus although in practice the same receiver is used in the airborne segment of both the CVOR and DVOR systems, different analysis methods are applied processing the CVOR and DVOR signals in the new OUNPPM. As can be seen in the overview section on the operational principles of the CVOR and DVOR, although the composite signals in space of CVOR and DVOR systems are the same, the ground stations operate differently. The receiver model of the new CVOR/DVOR model exploits the underlying operational principles of the CVOR and DVOR ground stations to obtain a simple means of obtaining the bearing information.

For either a CVOR or DVOR operating at a fixed frequency in the 108-117.95 MHz frequency band, with antennas mounted at a given height above a counterpoise of specific size which itself is elevated at a height above the ground, the model developed in this thesis predicts errors caused by adjusting CVOR/DVOR ground station parameters considering multipath for a given flight profile. The ground is defined by its constitutive parameters and classified as a perfect electrically conducting (PEC), desert, sea-water, or snow medium. The structure of the model is depicted in Figure 3-1.

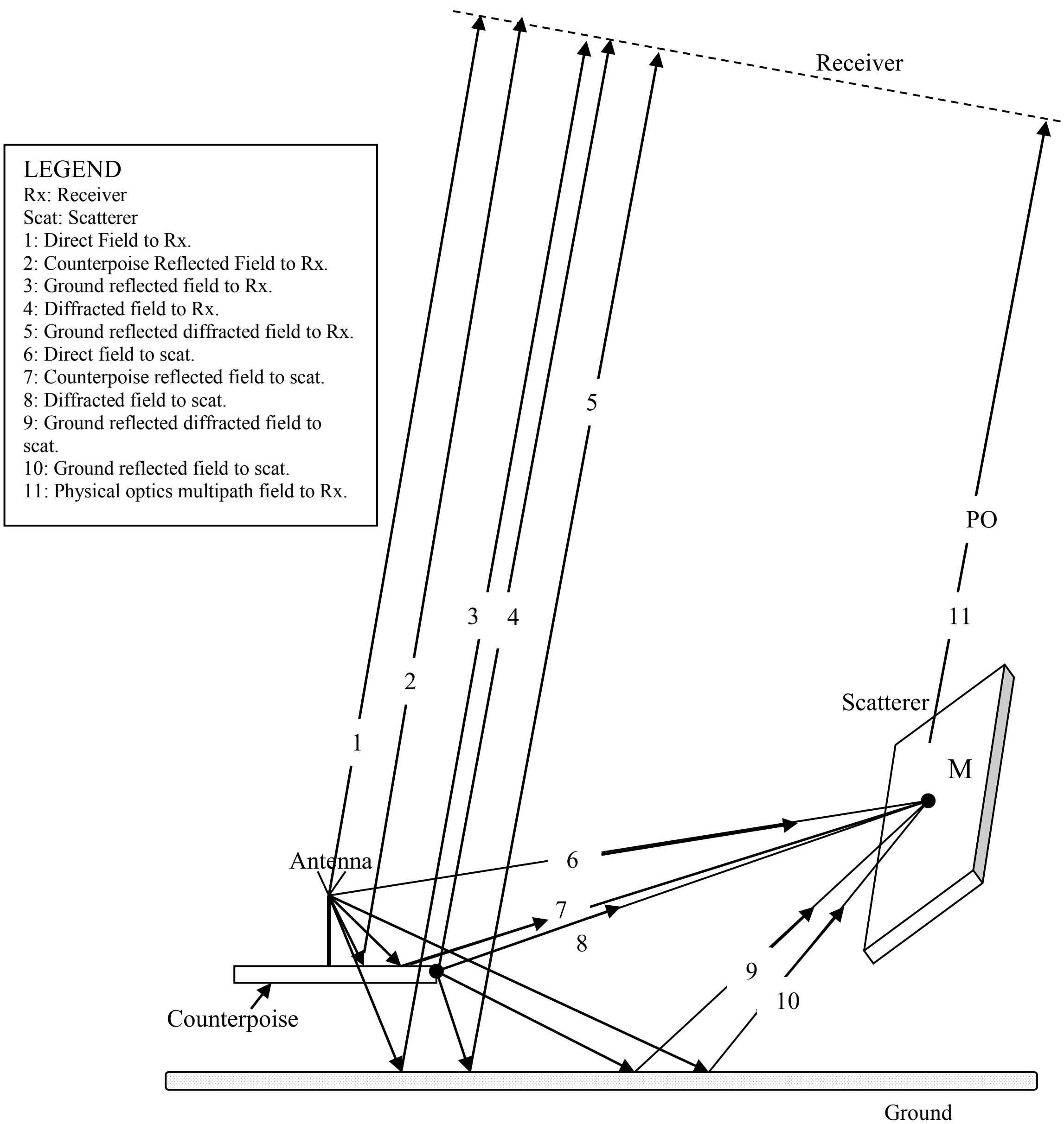

*Figure 3-1.*CVOR/DVOR error model (not to scale).

Fields represented by rays 1-11 in Figure 3-1 were modeled in the new CVOR/DVOR model of the new OUNPPM developed in this thesis.

3.2 Coordinate System

The coordinate system adopted in this software model is shown in Figure 3-2. The elevation (U) of the ground terrain at the CVOR/DVOR ground station, and the elevation (W) of the ground terrain at the scatterer location (W) are referenced from Mean Sea Level (MSL) which is coincident with the X-Y plane. The elevation of the counterpoise (H_c) above ground is referenced from the surface of the local ground at the CVOR/DVOR ground station. The height (H_A) of the antenna is referenced from the surface of the counterpoise. The Y-axis of the coordinate system is parallel to the Magnetic North (MN) azimuth

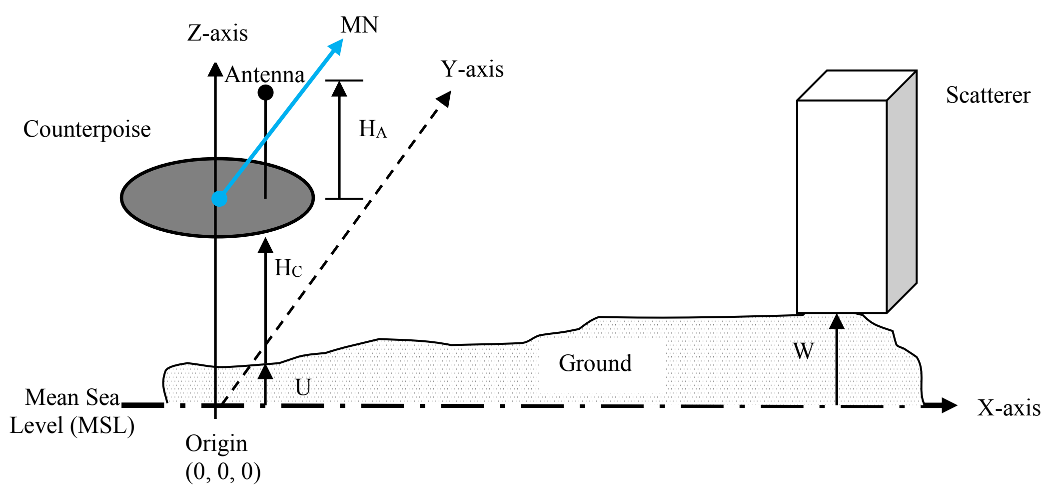

Figure 3-2. Coordinate system adopted in CVOR/DVOR model.

3.2.1 Computation of 3-D UTD Fields. The assumptions in the CVOR/DVOR ground station models are as follows;

1. The CVOR/DVOR counterpoise is a smooth, circular, flat perfect electrical conductor.
2. The local ground is smooth and homogeneous.
3. Coupling between antennas is not modeled.

Each antenna is assumed to be excited with unit amplitude, zero phase voltage. Modulation indices are applied later on in the receiver model to adjust for the difference between the carrier and sideband transmitter RF powers input into the ground station antennas in the case of the DVOR ground station. The constituent fields of the 3-D UTD field for a single CVOR/DVOR Alford loop are shown in Figure 3-1. For a single CVOR/DVOR ground station antenna, the 3-D UTD field ($\mathbf{E}_{UTD}$) from the antenna that will be received at an observation point is given by

$$\mathbf{E}_{UTD} = \mathbf{E}_{1,2}^{GO} + \mathbf{E}_{3}^{GO} + \mathbf{E}_{4}^{D} + \mathbf{E}_{5}^{D} \tag{3-1}$$

Where:

$\mathbf{E}_{1,2}^{GO}$ = GO field; *not* reflected from ground (sum of fields 1 and 2 in Figure 3-1)

$\mathbf{E}_{3}^{GO}$ = Ground reflected GO field (field 3 in Figure 3-1)

$\mathbf{E}_{4}^{D}$ = 3-D UTD diffracted field from counterpoise (field 4 in Figure 3-1)

$\mathbf{E}_{5}^{D}$ = ground reflected diffracted field (Field 5 in Figure 3-1)

Note that equation (3-1) does not include multipath from any scatterer in the vicinity of the CVOR/DVOR station. Although fields such as those represented by rays 2, 3, 4 and 5 in Figure 3-1 are multipath fields, throughout this document the term “multipath” will exclusively refer to the PO field (ray 11 in Figure 3-1) arriving at the receiver/aircraft from any scatterer(s) in the vicinity of the CVOR/DVOR ground station.

The steps for computing the GO field and the 3-D UTD diffracted fields are outlined in sections 3.2.1.1 and 3.2.1.2 below. As mentioned in section 1.3, the fields represented by rays 6-9 in Figure 3-1 are used by the existing Physical Optics Scattering Model to compute multipath field ($\mathbf{E}_{PO,\ SCAT}$) from the scatterer. $\mathbf{E}_{PO,\ SCAT}$ is represented by ray 11 in Figure 3-1. Thus for a CVOR/DVOR antenna radiating in the presence of a scatterer (e.g., building), the total field that would arrive the receiver is given by,

$$\mathbf{E}_{TOTAL} = \mathbf{E}_{UTD} + \mathbf{E}_{PO,SCAT} \tag{3-2}$$

3.2.1.1 Computation of GO Field from the Station to the Receiver ($\mathbf{E}_{1,2}^{GO} + \mathbf{E}_{3}^{GO}$). The pertinent GO fields from the station to the receiver (no multipath from scatterer) are shown in Figure 3-3. "A" represents a real CVOR/DVOR Alford loop antenna. "B" is a virtual source to account for the imaging of "A" below the counterpoise. Thus the field from "B" accounts for the reflected field from the counterpoise that arrives at the receiver. Sources "C" and "D" are images of "A" and "B" respectively below the ground. The composite of the fields from C and D at the observation point constitutes the ground reflected GO field.

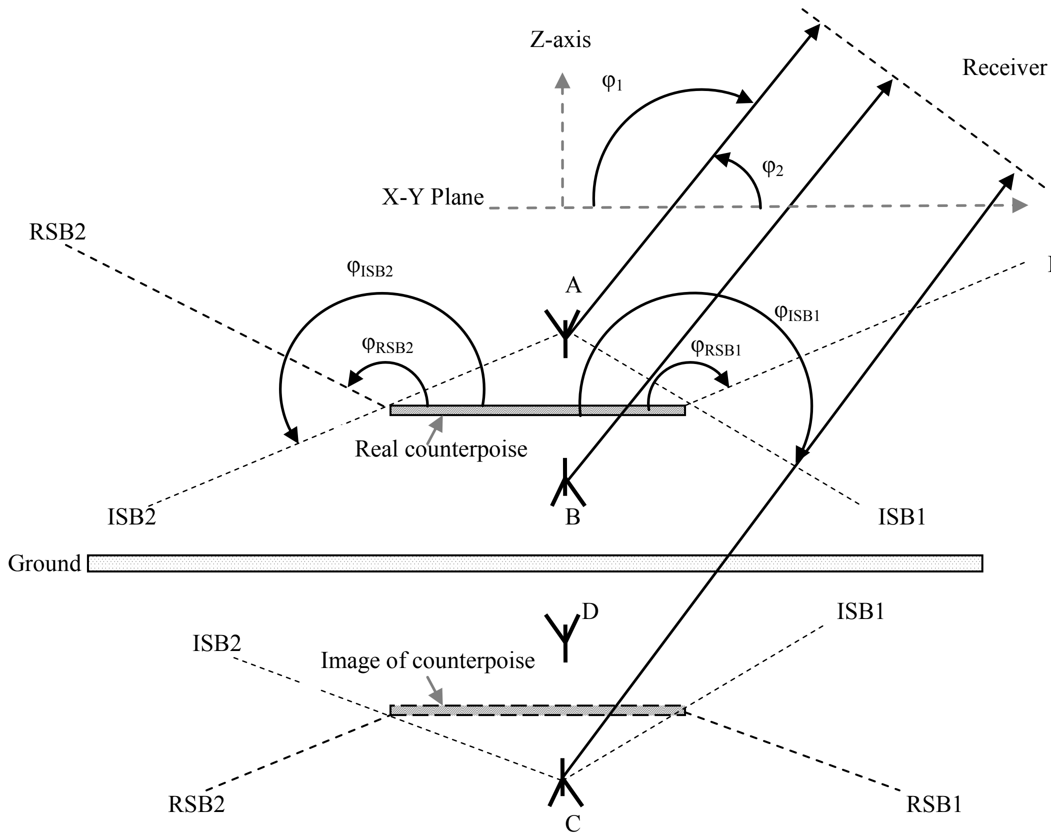

Figure 3-3. CVOR/DVOR antenna on a counterpoise over ground.

The following are the steps in determining the GO field.

1) With the position of the antenna above the counterpoise known, the angular positions of the reflection and incidence shadow boundaries RSB1, ISB1, RSB2 and ISB2 as shown in Figure 3-3 are determined. For a given direction of observation/receiver position, the angular positions of the RSBs and ISBs would determine which fields (from A, B and C) will illuminate at the receiver. "D" is only included in Figure 3-3 for completeness. No contribution from "D" will arrive at the receiver for any receiver position. The GO field distribution for the

geometry illustrated in Figure 3-3 is tabulated in Table 3-1 and Table 3-2. “AND” and “OR” in Table 3-1 and Table 3-2 are the Boolean “AND” and “OR” operators.

Table 3-1

Direct GO field distribution

Receiver Position (φ_1, φ_2)	Field from “A” present	Field from “B” present
($\varphi_1 <\ _{RSB1}$) AND ($\varphi_2 < \varphi_{RSB2}$)	YES	YES
($\varphi_{RSB1} < \varphi_1 < \varphi_{ISB1}$) OR ($\varphi_{RSB2} < \varphi_2 < \varphi_{ISB2}$)	YES	NO
($\varphi_1 > \varphi_{ISB1}$) AND ($\varphi_2 > \varphi_{ISB2}$)	NO	NO

Table 3-2

Ground reflected GO field distribution

Receiver Position (ϕ_1, ϕ_2)	Field from “C” present	Field from “D” present
((360 – φ_1)< φ_{ISB1}) OR ((360 – φ_2)< φ_{ISB2})	YES	NO
((360 – φ_1)> φ_{ISB1}) OR((360 – φ_2)> φ_{ISB2})	NO	NO

For example, for the specific scenario of Figure 3-3, (($\varphi_1 < \varphi_{RSB1}$) AND ($\varphi_2 < \varphi_{RSB2}$)) and also ((360 – $\varphi_1 > \varphi_{RSB1}$) AND (360 – $\varphi_2 > \varphi_{RSB2}$)), and therefore *only* fields from A and B will illuminate the receiver.

2) The distance of the receiver from antennas A, B, and C in Figure 3-3 are then computed using the same geometry of Figure 3-4.

$$R_{ctp} = R_o - H_c\cos\gamma, \text{ [meters]} \quad (3\text{-}3)$$

$$R_x = R_{ctp} - d\cos\varphi_2, \text{ [meters]} \quad (3\text{-}4)$$

$$R_A = R_x - H_A\cos\gamma, \text{ [meters]} \quad (3\text{-}5)$$

$R_B = R_x + H_A\cos\gamma$, [meters] (3-6)

$R_C = R_x + 2(H_A + H_C)\cos\gamma$, [meters] (3-7)

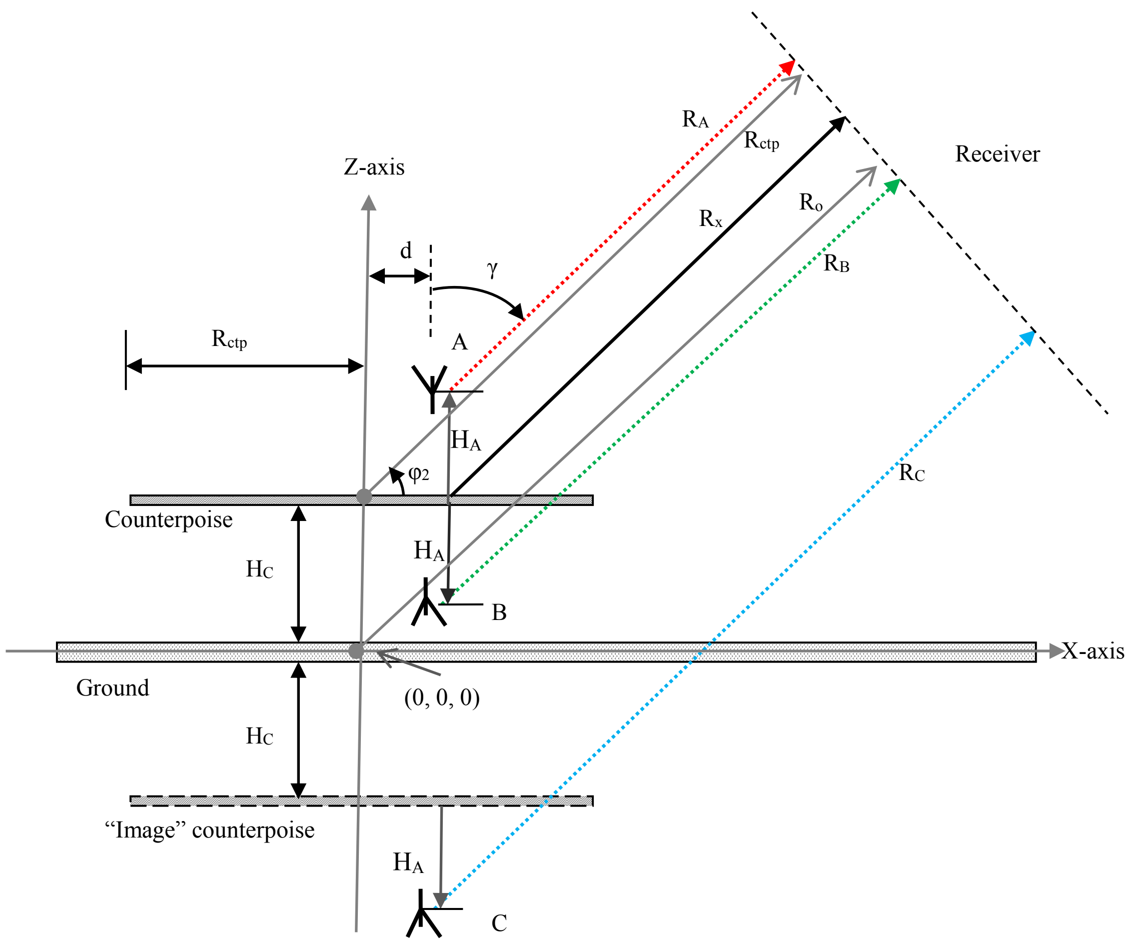

Figure 3-4. Range parameters for computing direct and ground reflected GO fields.

3) The total GO field, $\mathbf{E}^{GO}$ (sum of 1, 2 and 3 in Figure 3-1) from the station to the receiver is given by,

$$\mathbf{E}^{GO} = \mathbf{E}_1^{GO} + \mathbf{E}_2^{GO} + \mathbf{E}_3^{GO} \quad (3\text{-}8)$$

Where:

$$\mathbf{E}_1^{GO} = \sin\gamma \frac{e^{-jkR_A}}{R_A} \tag{3-9}$$

$$\mathbf{E}_2^{GO} = \mathbf{\Gamma}_{\perp,\ CTP} \sin\gamma \frac{e^{-jkR_B}}{R_B} \tag{3-10}$$

$$\mathbf{E}_3^{GO} = \mathbf{\Gamma}_{\perp,GROUND}(\omega, \delta_3, \varepsilon, \sigma) \sin\gamma \frac{e^{-jkR_C}}{R_C} \tag{3-11}$$

$\mathbf{\Gamma}_{\perp,\ CTP}$ = Horizontal polarization reflection coefficient for counterpoise.

Counterpoise is PEC, and therefore $\mathbf{\Gamma}_{\perp,\ CTP} = -1$.

$\mathbf{\Gamma}_{\perp,GROUND}(\omega, \delta_3, \varepsilon, \sigma)$ = Horizontal polarization reflection coefficient of the terrain/ground. In consistency with the notation of chapter 1, δ_3 is the angle the incident ray that produces reflected ray 3 makes with the ground/terrain.

3.2.1.2 Computation of 3-D UTD Diffracted Field from Station to the Receiver $(\mathbf{E}_4^D + \mathbf{E}_5^D)$. The 3-D UTD diffracted fields that arrive at the receiver include the fields represented by rays 4 and 5 in Figure 3-1. Ray 4 is the diffracted field from the edge of the counterpoise that arrives at the receiver via a direct LOS path, whilst ray 5 is the diffracted field that arrives at the receiver after being reflected from the ground. Figure 3-5 illustrates the important parameters needed in computing the 3-D UTD diffracted field.

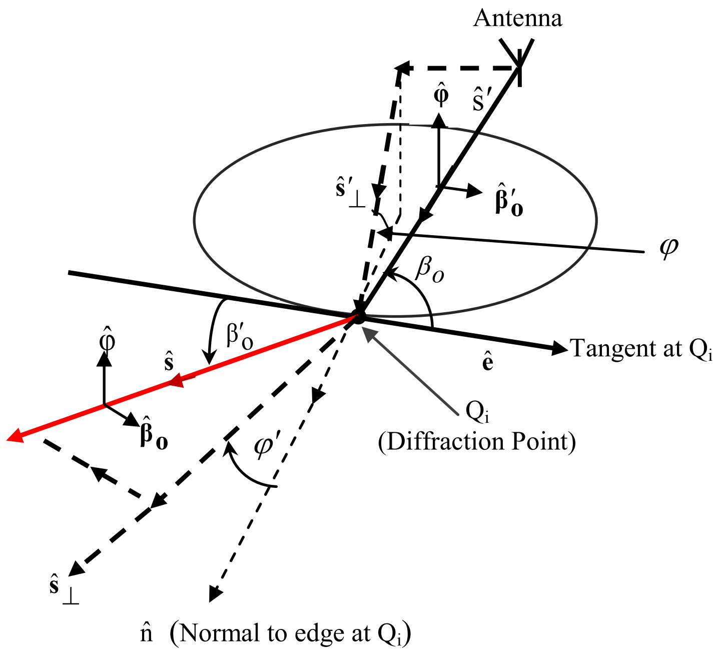

Figure 3-5. Parameters for computing 3-D UTD diffracted field.

The diffracted field from the counterpoise is computed by applying (2-27). The steps in computing the direct (LOS) 3-D UTD diffracted field are as follows;

1) Determine the locations of the diffraction points along the edge of the counterpoise. Each diffraction point such as Q_i in Figure 3-5 must satisfy Keller's Law of Edge Diffraction;

$$\beta'_o = \beta_o \quad \Rightarrow \quad \hat{\mathbf{s}}' \bullet \hat{\mathbf{e}} = \hat{\mathbf{s}} \bullet \hat{\mathbf{e}} \tag{3-12}$$

Manipulation of (3-9) yields a 6th -order polynomial equation. See Appendix B.

2) Compute the horizontally polarized component of the field incident on Q_i. From [18], the incident field $\mathbf{E}^i$ at Q_i can be computed by

$$\mathbf{E}^{i}\left(Q_i\right) = \cos\varphi \frac{e^{-jks'}}{s'} \hat{\psi} \bullet \hat{\beta}'_o \quad (3\text{-}13)$$

Where:

$\hat{\boldsymbol{\psi}}$ = Unit vector parallel to polarization of antenna.

$\mathbf{s}'$ = Distance from source point to Q_i.

$\hat{\boldsymbol{\beta}}'_{\mathbf{o}}$ = Vector parallel to EFPI. From [16, 18, 20]

$$\hat{\boldsymbol{\beta}}'_{\mathbf{o}} = \hat{\boldsymbol{\varphi}}' \times \hat{\mathbf{s}}' \quad (3\text{-}14)$$

Where:

From [18],

$$\hat{\boldsymbol{\varphi}}' = \frac{-\hat{\mathbf{e}} \times \hat{\mathbf{s}}'}{\left|\hat{\mathbf{e}} \times \hat{\mathbf{s}}'\right|} \quad (3\text{-}15)$$

3) From [18] the distance parameters of (2-30) and (2-31) for spherical wave incidence (as from the Alford loop) on a half-plane with flat faces, for observations in the far-field simplify to

$$L^{i,\,ro,\,rn} = s'\sin^2\beta_o \quad (3\text{-}16)$$

Where:

s′= Distance from antenna to diffraction point Q_i on edge of counterpoise.

β_o = Angle between incident ray and tangent to the edge at the diffraction point in the EFPI; See Figure 3-5.

4) Compute the soft diffraction coefficient, D_s by using (2-29). The Fresnel integral in this model is computed by using a routine given in [18]. The angles ϕ' and ϕ are

measured in normal plane of incidence, and the normal plane of diffraction respectively. These planes were defined in section 2.3.5.2.

5) Compute the diffracted field by applying (2-27).
6) The total diffracted field is the sum of diffracted fields from all diffraction points (Q_i) that were determined in step 1.
7) The ground reflected diffracted field was computed by applying steps 1-6 above to the image counterpoise and the image antenna “C” as shown in Figure 3-6. That is, it was assumed that antenna is now located at the position of “C” and the counterpoise is the image counterpoise. The position of the receiver however remains unchanged. With reference to Figure 3-6, the ground reflected diffracted field emanates from Q_i’ on the image counterpoise. The diffracted field from Q_i’ to the observation point is computed as if the ground were absent. This diffracted field is subsequently multiplied by the ground reflection coefficient to obtain the ground reflected diffracted field. The total ground reflected diffracted field is obtained by superposing all the contributions from the edge of the image counterpoise.

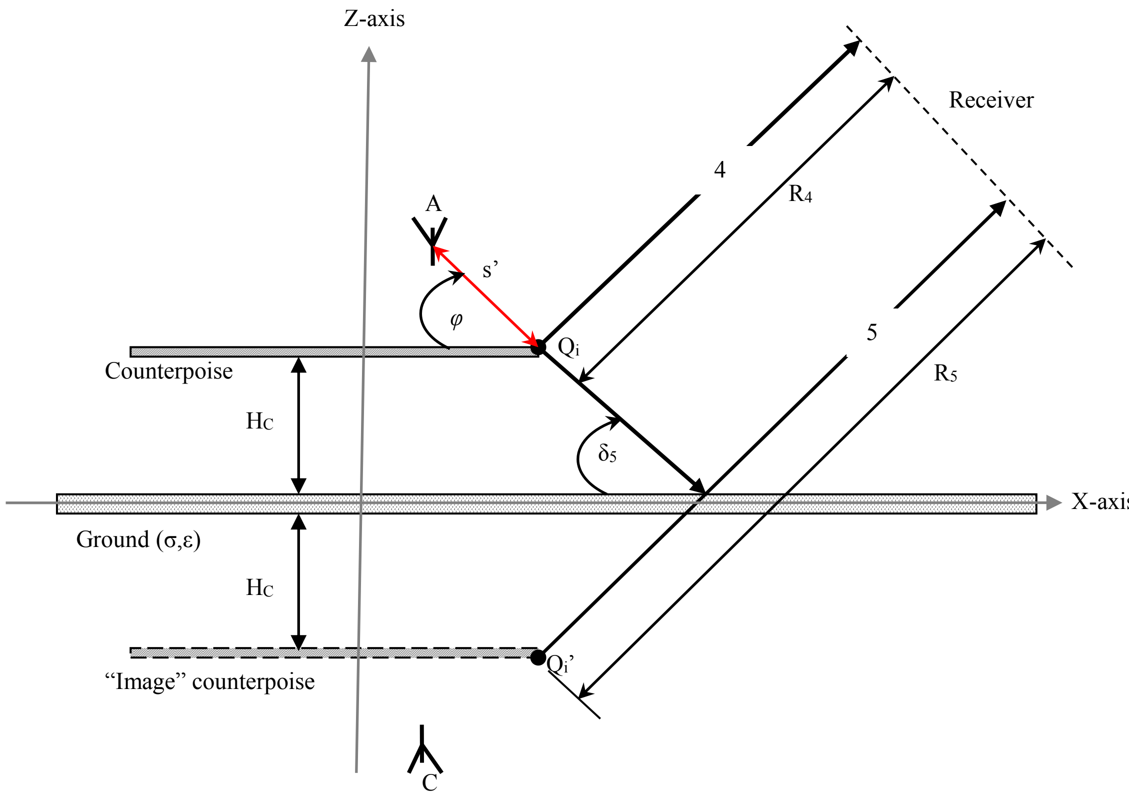

Figure 3-6. Geometry for computing diffracted and ground reflected diffracted field.

With reference to Figure 3-6 the total diffracted field to the observation point is given by,

$$\mathbf{E}^D = \mathbf{E}_4^D + \mathbf{E}_5^D \tag{3-17}$$

Where:

$$\mathbf{E}_4^D = \cos\varphi \frac{e^{-jks'}}{s'} D_s \sqrt{\rho} \frac{1}{R_4} e^{-jkR_4} \tag{3-18}$$

$$\mathbf{E}_5^D = \mathbf{\Gamma}_\perp(\omega, \delta_5, \sigma, \varepsilon) \cos\varphi \frac{e^{-jks'}}{s'} D_s \sqrt{\rho'} \frac{1}{R_5} e^{-jkR_5} \tag{3-19}$$

All terms retain their previously defined meanings and ρ' refers to the diffraction caustic distance associated with diffraction points such as Q_i' located on the image counterpoise.

3.2.1.3 Scattering Model. As already mentioned in section 1.2, multipath fields are computed using an existing Physical Optics (PO) model in the old OUNPPM. In the PO scattering model, each scattering structure is modeled using PEC plates. Each plate structure is decomposed into a number of smaller pieces, and the total field scattered from the structure is computed by superposition of the PO fields from all the constituent pieces of the scatterer [4]. In order to compute the scattered field from the each piece, the 3-D UTD field that arrives at that piece must be determined and input into the PO model [4]. Thus the 3-D UTD field that arrives at the scatterer piece is given by,

$$\mathbf{E}_{UTD,\,INPUT} = \mathbf{E}_{6,7}^{GO} + \mathbf{E}_{8}^{D} + \mathbf{E}_{10}^{GO} + \mathbf{E}_{9}^{D} \tag{3-20}$$

Where:

$\mathbf{E}_{6,7}^{GO}$ = GO field; *not* reflected from ground (sum of fields 6 and 7 in Figure 3-1)

$\mathbf{E}_{8}^{D}$ = 3-D UTD diffracted field from counterpoise (field 8 in Figure 3-1)

$\mathbf{E}_{10}^{GO}$ = Ground reflected GO field (field 10 in Figure 3-1)

$\mathbf{E}_{9}^{D}$ = Ground reflected diffracted field (Field 9 in Figure 3-1)

In the PO model, $\mathbf{E}_{UTD,\,INPUT}$ of equation (3-20) is used to compute the currents induced on the surface of that scatterer piece [4]. Radiation integrals are subsequently applied to these induced currents to determine the multipath (PO) field that will arrive at the aircraft [4]. If the PO model is represented by a transfer function H_{PO}, the PO scattered field $\mathbf{E}_{PO,\,SCAT}$ is given [4] by,

$$\mathbf{E}_{11}^{PO} = \mathrm{H}_{\mathrm{PO}}(\mathbf{E}_{UTD,\, INPUT}) \tag{3-21}$$

3.2.1.4 Receiver Processing of CVOR Signal. A few details about the operational principles of the CVOR ground station will be repeated here to clarify the method that has been applied in the new OUNPPM to process the CVOR signals. In the CVOR ground station, the main RF carrier signal amplitude modulated with the 9960 Hz FM sub-carrier, and the double sideband suppressed carrier signals (DSB-SC) sideband RF signals are radiated simultaneously from the four (4) CVOR ground station antennas. Equal power of the amplitude modulated main RF carrier is input into and radiated from the NW, NE, SW, and SE antennas of station. On the contrary, two (2) DSB-SC signals namely the “positive sine” [10] and “negative cosine” [10] are supplied respectively to the NW-SE and NE-SW antenna pairs. The antennas of each pair are excited out of phase with their respective DSB-SC signal. The 9960 FM sub-carrier, the positive sine DSB-SC and negative cosine DSB-SC signals are generated by the goniometer so that there is a fixed phase difference between 30 Hz AM signal on the DSB-SC signal and the 30 Hz FM signal on the 9960 sub-carrier input into each antenna. This fixed phase relationship is maintained in the radiated fields.

A CVOR analysis method known as the *audio-phase concept* [10] was implemented in the new CVOR model of the new OUNPPM. In the VOR community, the term *audio-phase* is generally used to refer to the phase difference between the recovered/demodulated variable and reference signals. The audio-phase concept enables the determination of the bearing of a receiver by

- Analyzing the radiation pattern of the DSB-SC signals radiated from the CVOR ground station antennas. The pattern from each individual antenna will be referred to as a *lobe*. Thus the CVOR station DSB-SC radiation pattern is made up of the NW lobe, NE lobe, SW lobe and SE lobe. [10]
- Analyzing the phase difference that exists between the 30 Hz AM tone on each DSB-SC and the 30 Hz reference signal FM on the sub-carrier radiated from each of the antennas of the CVOR ground station. This phase difference is also referred to as *audio-phase*. Thus the meaning of the term *audio-phase* could be slightly different depending on the context in which it is used. [10]

The recovered 30 Hz AM on the positive sine DSB-SC signal radiated from the NW antenna lags the 30 Hz reference FM signal by 315 degrees. Thus the NW lobe will have a constant audio-phase of –315 degrees. Since the SE Alford loop is excited with a DSB-SC signal whose phase lags the positive sine DSB-SC signal input into the NW antenna by 180 degrees, the 30 Hz AM on it will lag the 30 Hz FM reference signal by 135 electrical degrees. Thus the SE lobe will therefore have a constant audio-phase of –135 degrees. By similar considerations, the NE lobe has constant audio-phase of –45 degrees and the SW lobe has an audio-phase of –225 degrees. [10]

Figure 3-7 illustrates the DSB-SC radiation pattern of the CVOR, and the audio-phase of the lobes of the radiation pattern. The NW and SE lobes constitute a pair which in this analysis will be referred NW-SE lobe pair, and similarly the NE and SW lobes constitute the NE-SW lobe pair. From Figure 3-7, it can be deduced that an aircraft located at any bearing (θ) from the ground station will detect at most only one lobe of each of the lobe pairs. Thus at no bearing angle will a receiver detect both of the lobes of a lobe-pair. For instance, an aircraft located at $\theta = 0^{o}$ (MN) will detect equal amplitudes of fields from the NW and NE lobes. However audio-phases of –315 degrees and –45 degrees, representing the audio-phases of NW and NE lobes respectively will be detected at MN. The contributions from the NW and NE antennas can be represented by two (2) phasors of equal magnitudes but whose phases are equal to the phases of their respective audio-phases. Vector addition of these two (2) phasors would produce a phasor whose phase is exactly equal to the bearing (0 degrees) at MN. [10]

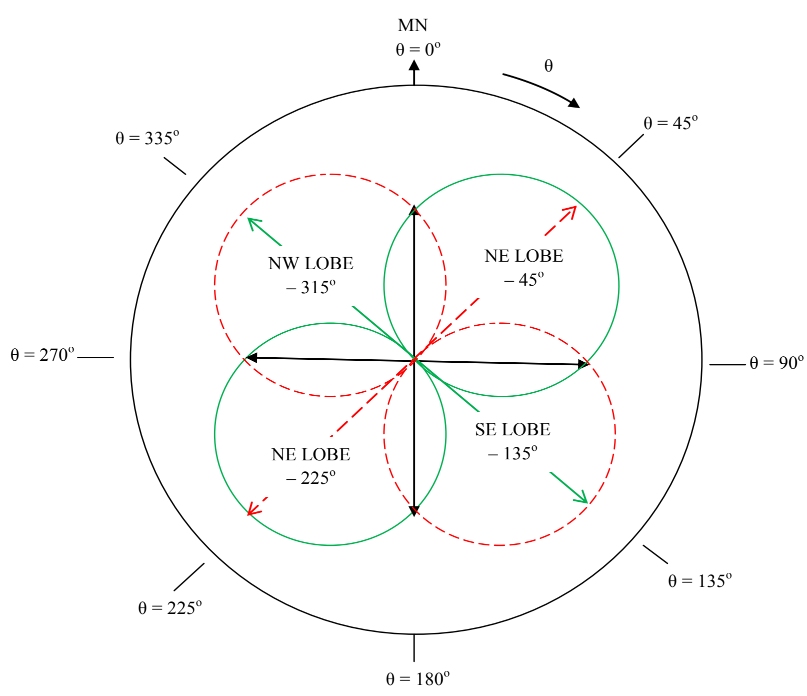

Figure 3-7. DSB-SC radiation pattern of CVOR ground station antenna array showing the audio-phases of lobes of the radiation pattern. This Figure was redrawn from [10].

To further clarify the procedure followed in applying the audio-phase concept to compute the bearing of an aircraft, the audio-phase concept will be applied to compute the bearing of an aircraft located at a bearing of 20 degrees from the CVOR ground station. As shown in Figure 3-8, an aircraft located at a bearing of 20 degrees from the CVOR ground station will detect only the NW and NE lobes. However unlike the $\theta = 0$ degrees case, different magnitudes of DSB-SC signal radiated fields from the NW-SE and NE-SW antenna pairs will be received at $\theta = 20$ degrees. The magnitudes of the NW-SE and NE-SW fields are proportional to the lengths of the vectors OB ($E_{NW\text{-}SE}$) and OA ($E_{NE\text{-}SW}$) respectively in Figure 3-8. $E_{NW\text{-}SE}$ and $E_{NE\text{-}SW}$ will be assigned phases of – 315 and – 45 degrees respectively. Addition of these phasors to obtain the bearing is also illustrated in Figure 3-8. In the phasor diagram, the phases of the $E_{NW\text{-}SE}$ and $E_{NE\text{-}SW}$ phasors are measured from a vector ("Reference") which in this analysis should be taken to be the phasor representing the 30 Hz FM (reference signal) on the 9960 Hz sub-carrier.

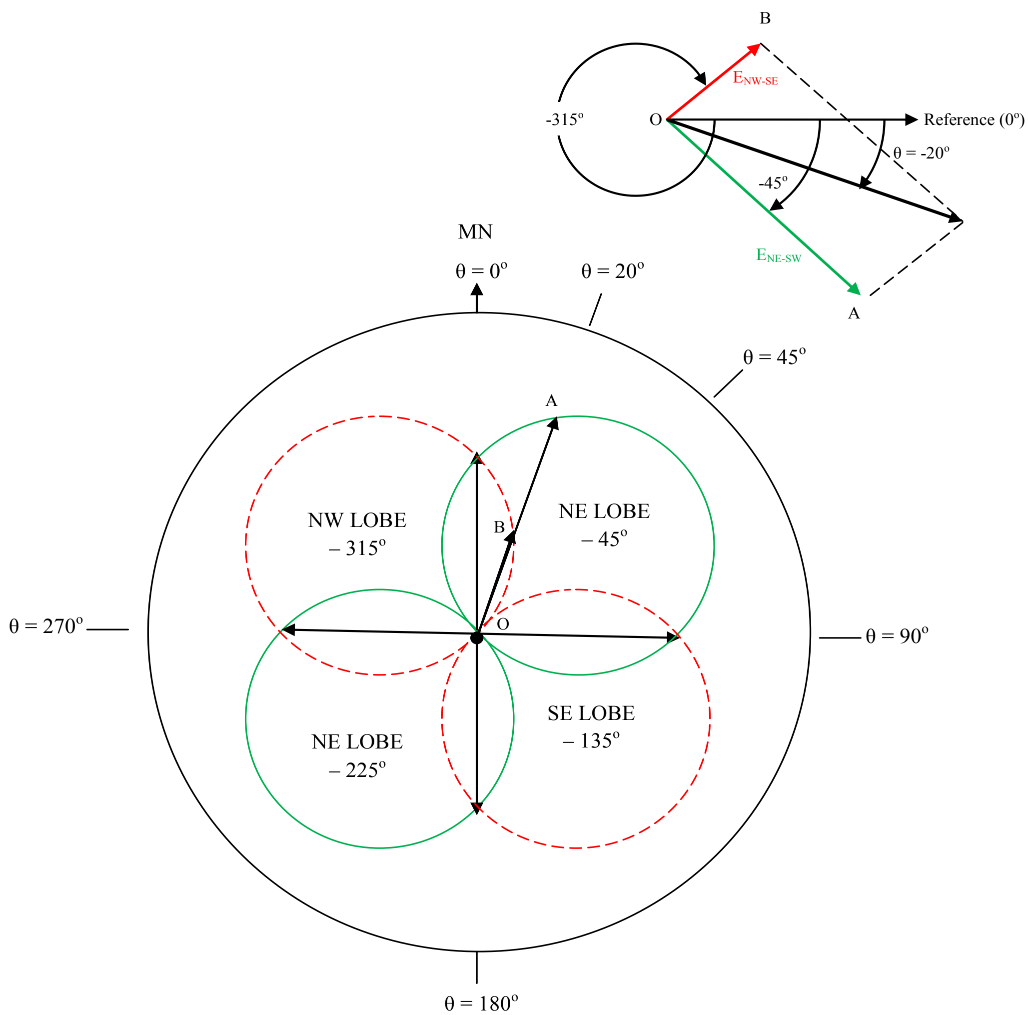

Figure 3-8. Audio-phase concept of aircraft located at a bearing of 20 degrees from a CVOR ground station. This Figure was redrawn and adapted from [10].

From the above explanation on the audio-phase concept, it can be deduced that the only information needed to compute the bearing of an aircraft/receiver are the following;

- The absolute magnitude of the DSB-SC radiated fields from the NW-SE and the NE-SW antenna pairs that will arrive at the aircraft/receiver.

- The true bearing (θ_{true}) of the aircraft/receiver. With θ_{true} known, the audio-phase(s) that will be received from the NW-SE and/or the NE-SW lobe pairs can be obtained from Figure 3-7 or Table 3-3 below.

Table 3-3

Audio-phase distribution around CVOR ground station

Receiver Location (θ_{true}) [degrees]	Audio-phase of NW-SE Lobe Pair (α_1) [degrees]	Audio-phase of NE-SE Lobe Pair (α_2) [degrees]
$0 \leq \theta \leq 45$ $315 \leq \theta < 360$	-315	-45
$45 < \theta \leq 135$	-135	-45
$135 < \theta \leq 225$	-135	-225
$225 < \theta < 360$	-315	-225

A brief note on the fields from the CVOR station that will arrive at the aircraft will be given here. Figure 3-9 depicts the fields from a CVOR station operating in the presence of a scatterer.

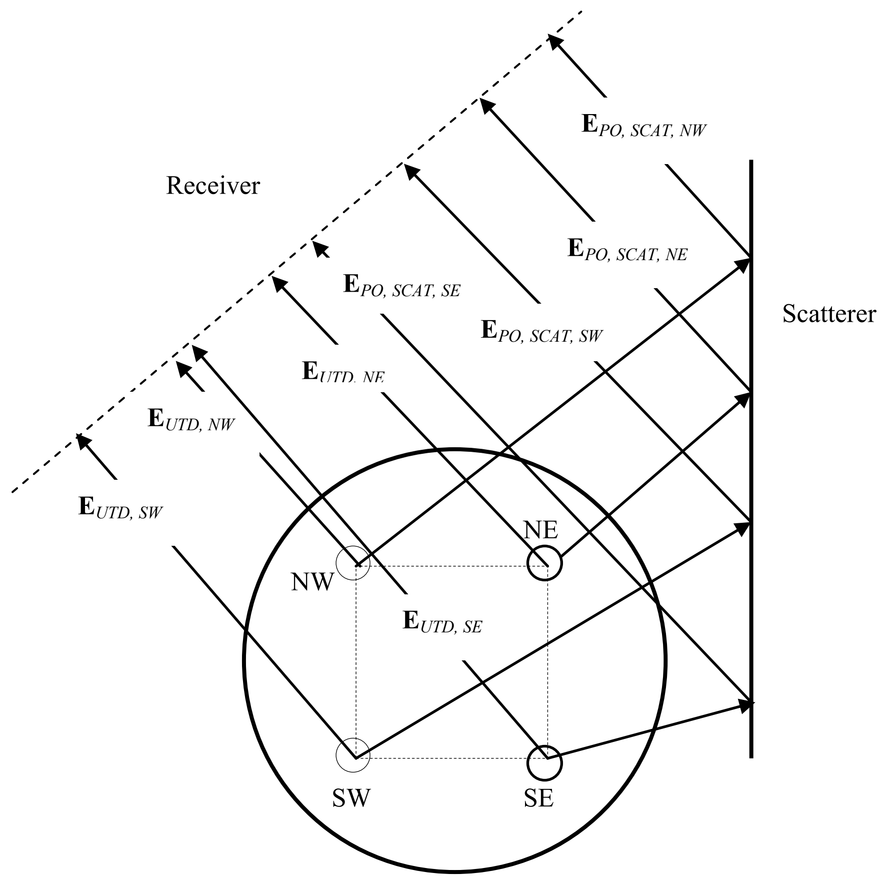

Figure 3-9. A CVOR ground station illustrating fields from antennas and a scatterer.

The DSB-SC fields due to the NW, SE, NE, and SW CVOR ground station antennas were computed by applying equation (3-2). From equation (3-2) these fields are given by,

$$\mathbf{E}_{TOTAL,\,NE} = \mathbf{E}_{UTD,\,NE} + \mathbf{E}_{PO,SCAT,\,NE} \tag{3-22}$$

$$\mathbf{E}_{TOTAL,\,SW} = \mathbf{E}_{UTD,\,SW} + \mathbf{E}_{PO,SCAT,\,SW} \tag{3-23}$$

$$\mathbf{E}_{TOTAL,\,NW} = \mathbf{E}_{UTD,\,NW} + \mathbf{E}_{PO,SCAT,\,NW} \tag{3-24}$$

$$\mathbf{E}_{TOTAL,\,SE} = \mathbf{E}_{UTD,\,SE} + \mathbf{E}_{PO,SCAT,\,SE} \tag{3-25}$$

As mentioned above the NW and SE antennas constitute a pair, and the NE and SW antennas form another pair. The elements of each pair (NW-SE and NE-SW) are fed 180 electrical degrees out of phase with one DSB-SC signal. In the field computation routine of this thesis, all the CVOR station antennas was assumed to be excited with voltages of equal amplitude and phase. Hence in order to account for the fact that the antennas of each pair are actually fed out-of-phase, the composite DSB-SC fields from the NW-SE and NE-SW pairs are computed by subtracting the fields due to the antennas of each pair. Thus,

$$\mathbf{E}_{TOTAL,\ NE-SW} = \mathbf{E}_{TOTAL,\ NE} - \mathbf{E}_{TOTAL,\ SW},\ [\text{V/m}] \tag{3-26}$$

$$E_{TOTAL,\ NE-SW} = \left|\mathbf{E}_{TOTAL,\ NE-SW}\right|,\ [\text{V/m}] \tag{3-27}$$

$$\mathbf{E}_{TOTAL,\ NW-SE} = \mathbf{E}_{TOTAL,\ NW} - \mathbf{E}_{TOTAL,\ SE},\ [\text{V/m}] \tag{3-28}$$

$$E_{TOTAL,\ NW-SE} = \left|\mathbf{E}_{TOTAL,\ NW-SE}\right|,\ [\text{V/m}] \tag{3-29}$$

Having computed $E_{TOTAL,\ NE\text{-}SW}$ and $E_{TOTAL,\ NW\text{-}SE}$ that arrive at the receiver, the audio-phase concept computes the bearing ($\theta_{COMPUTED}$) of the receiver as,

$$\theta_{COMPUTED} = \text{Argument}\ [(E_{TOTAL,\ NW\text{-}SE})\ e^{j\alpha 1} + (E_{TOTAL,\ NE\text{-}SW})\ e^{j\alpha 2}],\ [\text{degrees}] \tag{3-30}$$

Where:

α_1, α_2 = audio-phase of NW/SE and NE/SW antenna fields at a simulated bearing of θ_{true} from the CVOR station (Table 3-1). Note that in (3-30) these audio-phases should be converted to radians.

$E_{TOTAL,\ NW\text{-}SE}$ = Magnitude of NW-SE antenna pair field at a simulated bearing of θ_{true}

$E_{TOTAL,\ NE\text{-}SW}$ = Magnitude of NE-SW antenna pair field at a simulated bearing of θ_{true}

The bearing error, θ_{error} is then given by,

$$\theta_{\text{error}} = \theta_{COMPUTED} - \theta_{\text{true}} \tag{3-31}$$

It should be noted that in the above analysis it has been assumed that the audio-phases as given in Table 3-1 are maintained in space. Since each audio-phase is the phase of the recovered 30 Hz AM on the DSB-SC signal fed into a CVOR ground station antenna relative to the phase of the 30 Hz AM on the main carrier RF signal fed into the same antenna, it is can be assumed that any phase distortion in the 30 Hz AM on the DSB-SC signal, will also be observed in the phase of the 30 Hz on the main carrier RF signal, and thus the relative phase between the two will be maintained.

3.2.1.5 Receiving Processing of DVOR Signal. The alternative development of the DVOR in section 2.1.2 was implemented in the DVOR receiver model of the new OUNPPM. In this new DVOR receiver model, a model was first developed for the SSB DVOR and then systematically extended to the DSB DVOR by superposing two (2) SSB DVORs excited synchronously from two diagonally opposite antennas of the DVOR circular antenna array. The following points about the operational principle of the DVOR system will be repeated here to enhance the understanding of this section.

1. The bearing of the receiver from the DVOR ground station is computed as the phase lag of the variable signal from the reference signal.
2. In the absence of errors, the phase of the variable signal is exactly equal to the bearing of the receiver. From 1 above it can be inferred then that the phase of the DVOR reference signal in an ideal (no error) system should be zero.

3. However due to errors intrinsic in the DVOR ground station, reflections off the local terrain, and multipath from structures in the vicinity of the DVOR ground station, the phase of the DVOR variable signal will be distorted and thus will not be equal to the true bearing of the receiver. The phase of the reference signal will also be distorted, and will therefore not be equal to zero.

The DVOR receiver processing technique outlined in this section involves the determination of the phases of the variable and reference signals. The flow-chart of Figure 3-10 illustrates the steps followed in processing fields from a SSB DVOR system to obtain the bearing of the receiver/aircraft from the DVOR ground station.

The first step (*Block A* of Figure 3-10) is to compute the fields arriving at the receiver/aircraft from the DVOR ground station and any scatterer(s) in the vicinity of the ground station. Although a detailed explanation of how to compute these fields was given previously, a few points will be repeated here for clarity. Consider the top-view of an SSB DVOR ground station antenna array radiating in the presence of a scatterer as illustrated in Figure 3-11. In Figure 3-11, the sideband antennas configured in a circular antenna are labeled #1 through #50. The center antenna is labeled #0. $\mathbf{E}_{TOTAL}$ of equation (3-2) has been indexed in this analysis to specify the antenna’s whose field is being referred to. For instance the total field due to the center antenna arriving at the receiver is given by,

$$\mathbf{E}_{TOTAL}[0] = \mathbf{E}_{UTD}[0] + \mathbf{E}_{PO,SCAT}[0] \text{, [V/m]} \qquad (3\text{-}32)$$

similarly the fields from elements of the circular antenna array (circular array) are given by,

$$\mathbf{E}_{TOTAL}[i] = \mathbf{E}_{UTD}[i] + \mathbf{E}_{PO,SCAT}[i], \;\; i = 1, 2, \ldots, 50., \text{[V/m]} \tag{3-33}$$

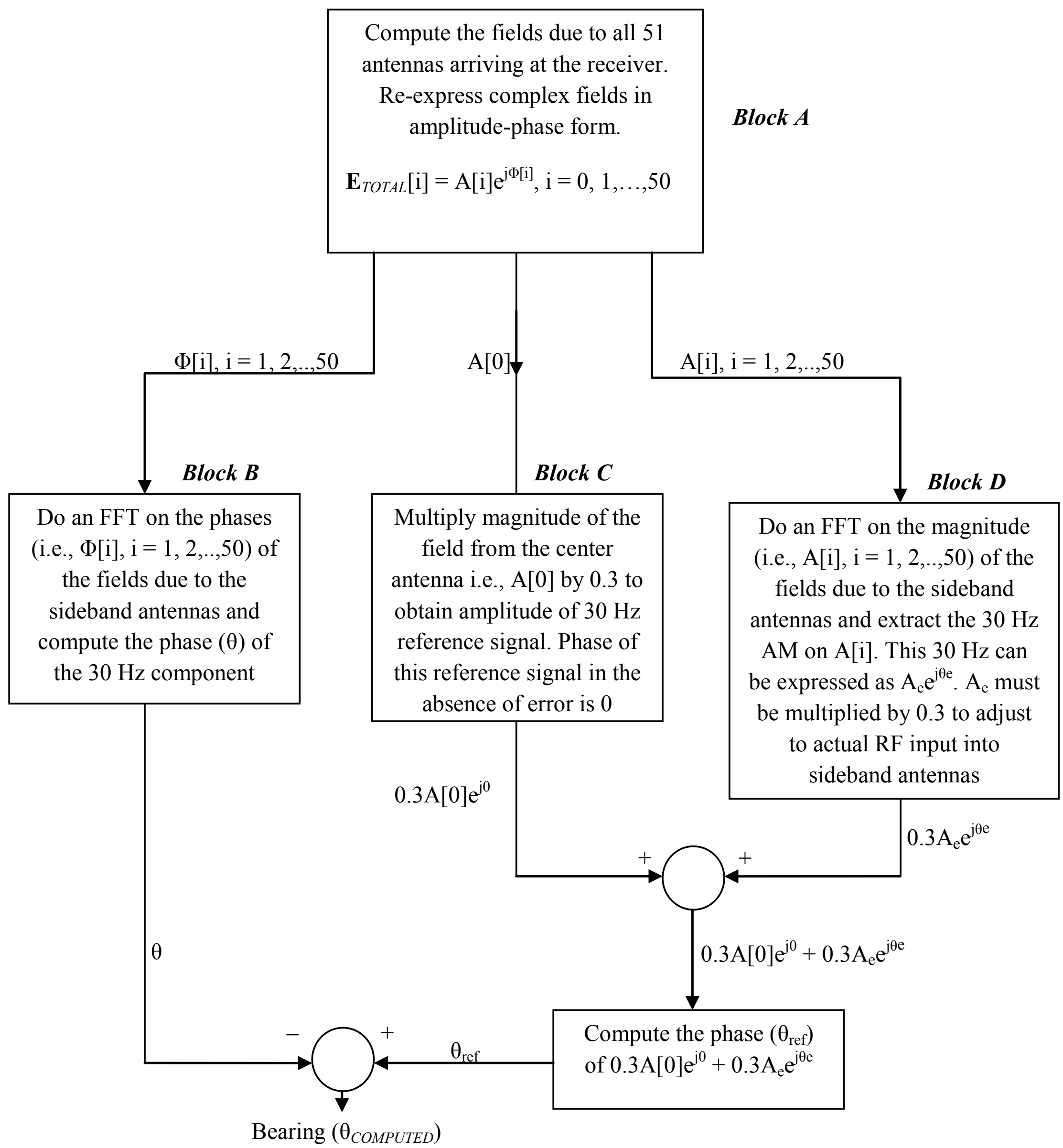

Figure 3-10. Flow-chart of technique applied in processing SSB DVOR signals.

The indexed vector of fields in equation (3-33) constitutes the FM sub-carrier (sideband), where in this SSB DVOR model it has been assumed that the antennas are excited sequentially from antennas #1 to #50 (see Figure 3-11).

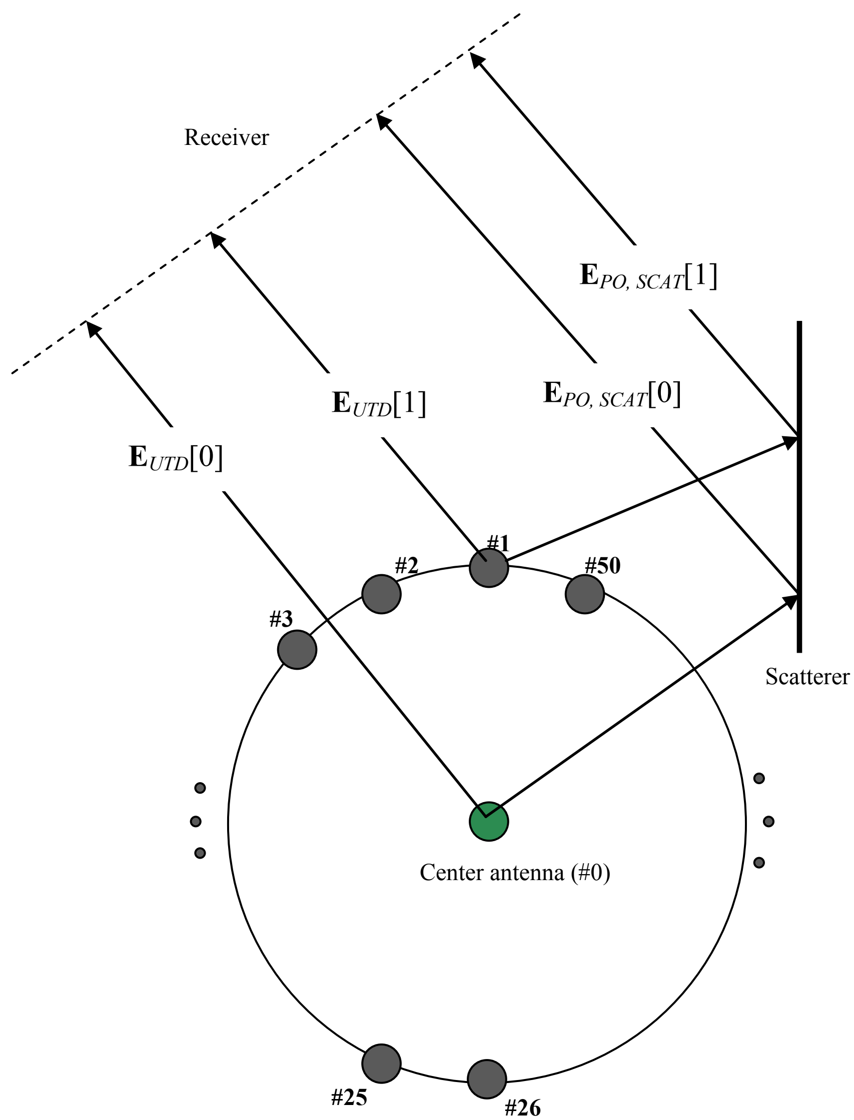

Legend

$\mathbf{E}_{UTD}[i]$ = Composite of rays 1, 2, 3, 4, and 5 of Figure 3-1 due to ith antenna

$\mathbf{E}_{PO,\ SCAT}[i]$ = Multipath field (ray 11 of Figure 3-1) due to field from ith antenna

Figure 3-11. Top-view of SSB DVOR ground station showing scattering from a scatterer.

Only one cycle of sequential excitation of the circular array was used in this analysis. The vector of computed fields from all fifty-one (51) antennas – one (1) center antenna and fifty (50) sideband antennas, of the DVOR can be re-expressed in amplitude-phase form as,

$$\mathbf{E}_{TOTAL}[i] = A[i]e^{j\Phi[i]},\ i = 0, 1, \ldots, 50.,\ [V/m] \qquad (3\text{-}34)$$

Where:

$A[i]$ = Amplitude of the field from the i^{th} antenna at receiver, [V/m]

$\Phi[i]$ = Phase of the field from the i^{th} antenna at receiver, [rad]

The last fifty (50) elements of the indexed vector of fields given in equation (3-34) correspond with the elements of the vector given in equation (3-33), and constitute the FM sub-carrier. Thus the FM sub-carrier in discrete amplitude-phase form is given by,

$$\mathbf{E}_{TOTAL}[i] = A[i]e^{j\Phi[i]},\ \ i = 1, \ldots, 50.,\ [V/m] \qquad (3\text{-}35)$$

For the purposes of this analysis, equation (3-35) will be compared to a discrete form representation of equation (2-15) given below.

$$s[i] = A[i]\cos(\omega_u\,[i\text{-}1]\Delta t - k[R_0 - r\cos(\omega_m\,[i\text{-}1]\Delta t + \theta]),\quad i = 1, 2, 3\ldots 50.,\ [V] \qquad (3\text{-}36)$$

In equation (3-36),

$\omega_m = 2\pi(30)$, [rad/s]

θ = Phase of variable signal, [rad]. i.e., the phase of s[i] is modulated by ω_m tone. In an ideal system, θ is equal to the true bearing (θ_{true}) of the receiver.

Δt = switching time between 50 antennas of circular array given by

$\Delta t = 1/\ (30x50)$ [seconds],

All the other variables retain their meanings in (2-15).

The index “i” in equation (3-36) specifies both the antenna and its time of excitation. Thus sideband/circular array antenna #i (for i = 1, 2,…, 50) is excited at the time instant given by $[i-1]\Delta t$.

Equation (3-35) and equation (3-36) are equivalent and therefore,

$$\Phi[i] = k[R_0 - r\cos(\omega_m [i-1]\Delta t + \theta]), \quad i = 1, 2, 3\ldots 50., [\text{rad}] \tag{3-37}$$

From equation (3-37) it can be deduced that the phase (θ) of the variable signal is the phase of the ω_m component of the phases, $\Phi[i]$ of the fields due to the sideband antennas of the DVOR ground station. Thus as shown in *Block B* of Figure 3-11, Fast Fourier Transform (FFT) techniques are applied to extract the phase (θ) of the 30 Hz component of $\Phi[i]$ ($i = 1, 2, 3,\ldots,50$).

In order to determine the bearing of the receiver/aircraft from the DVOR ground station the phase of the reference signal must also be determined. The reference signal is AM on the main RF carrier signal (from the center antenna) to a depth of 30 per cent. The amplitude of the 30 Hz reference signal is therefore 0.3 of the absolute magnitude of the field due to the center antenna of the DVOR ground station. The phase of this 30 Hz reference signal under ideal conditions is zero. Thus as shown in Figure 3-11, the output of *Block C* which is the undistorted 30 Hz reference signal can expressed as,

$$m(t) = 0.3A[0]\cos\omega_m t \tag{3-38}$$

Where:

$A[0]$ = Magnitude of field due to center antenna of DVOR station.

All other terms retain their previously assigned meanings.

As was mentioned in the overview of the operation of the SSB DVOR system, due to the eccentricity of the counterpoise, there is a 30 Hz AM imposed on the sideband signal (from the antennas of the circular array). This 30 Hz AM intermodulates the "main" 30 Hz reference signal on the main RF carrier signal, and thus distorts it. FFT techniques are applied to extract the 30 Hz AM on the absolute magnitudes, A[i] (i = 1, 2,…,50) of the fields from the circular array. This operation is effected in *Block D* of Figure 3-11. This spurious 30 Hz AM on the sideband signal can be expressed as,

$$n(t) = 0.3A_e \cos(\omega_m t + \theta_e) \qquad (3\text{-}39)$$

Where:

A_e = Amplitude of the 30 Hz AM signal on the sideband

θ_e = Amplitude of the 30 Hz AM signal on the sideband

The factor of 0.3 on the right-hand side of equation (3-39) has been used to adjust for the fact that the fields from the DVOR station antennas were computed by assuming that they were all with excited with equal RF power inputs, whilst in the actual DVOR ground station, the fed RF power fed into the circular array (sideband antennas) is 30% of the RF power that goes into the center antenna.

From [21] the resultant (distorted) 30 Hz reference signal is given by,

$$\hat{m}(t) = m(t) + n(t)\text{, [V]} \qquad (3\text{-}40)$$

Where:

m(t) = As given in equation (3-38)

n(t) = As given in equation (3-39)

Note that equation (3-34) is a generalization. Depending on the type of AM detection (i.e., square law, envelope detection, etc.), the formulation in equation (3-40) will be different. The phase (θ_{ref}) of the resultant 30 Hz AM reference signal, $\hat{m}(t)$ is given [21] by

$$\theta_{ref} = \tan^{-1}\left(\frac{\frac{0.3A_e}{0.3A[0]}\sin\theta_e}{1+\frac{0.3A_e}{0.3A[0]}\cos\theta_e} \right) \text{, [degrees]} \tag{3-41}$$

The computation of θ_{ref} is effected in *Block E* of Figure 3-10. The bearing of the receiver is then given by,

$$\theta_{COMPUTED} = \theta - \theta_{ref} \text{ , [degrees]} \tag{3-42}$$

With the true bearing (θ_{true}) of the receiver known, the bearing error is given by applying equation (3-31).

In summary, note the following about the method used in computing the bearing in the SSB DVOR,

- The 30 Hz FM variable signal is contained the phases, $\Phi[i]$ (for i = 1, 2,…, 50) of the fields due the antennas of the circular array of the DVOR.
- The spurious 30 Hz AM which distorts the main reference signal is contained in magnitudes, $A[i]$ (for i = 1, 2,…, 50) of the fields due the antennas of the circular array of the DVOR.

The DSB DVOR signal in space can be processed by analyzing it as a superposition of two SSB DVORs. The circular array of one of the DVORs is excited with sideband RF signal of frequency 9960 Hz higher than the DVOR center frequency, whilst the other is excited with a sideband RF signal whose frequency is 9960 Hz lower than the DVOR center frequency. The 2 SSB DVORs are scanned sequentially from diametrically opposite sides of the sideband antenna array. With reference to Figure 3-10, the circular antenna array of one of the constituent SSB DVORs is excited starting from #1 and proceeding counterclockwise through the to #50, whilst the second SSB DVOR is excited starting from #26 and proceeding counterclockwise through to #25. Note that in the case of the DSB DVOR however the sideband signal power inputs are 15% of the main RF carrier level. The bearing errors of the two SSB DVORs are summed to give the bearing error the composite DSB DVOR. Thus,

$$\theta_{error,total} = \theta_{error,\#1} + \theta_{error,\#26}\ , \text{[degrees]} \tag{3-43}$$

Where:

$\theta_{error,\#1}$ = Bearing error of SSB DVOR whose circular antenna array is excited starting from antenna #1, [degrees].

$\theta_{error,26}$ = Bearing error of SSB DVOR whose circular antenna array is excited starting from antenna #26, [degrees].

CHAPTER 4: TEST CONFIGURATIONS, RESULTS, AND VALIDATION OF CVOR/DVOR MODEL

4.1 Test Configurations and Results

In this section the capabilities of the new OUNPPM will be illustrated for specific CVOR/DVOR ground station and scatterer configurations simulated. Simulation scenarios, results, and performance analysis will be presented and discussed. The parameters of the CVOR/DVOR ground station configurations considered are as follows:

1) Radius of the counterpoise,
2) Height of counterpoise above the ground,
3) Height of the antenna above the counterpoise,
4) Ground type (e.g., PEC and snow medium)
5) Dimensions of scattering structure (i.e., Plate),
6) Separation distance between the scatterer and ground station, and
7) Orientation of the scatterer relative to radial from the ground station.

The main output parameters of interest from the CVOR/DVOR model of the new OUNPPM are the far zone electric field patterns of the CVOR/DVOR ground station antennas, and the bearing errors at the simulated aircraft location due to the configuration of the station, and a scattering structure near the CVOR/DVOR ground station. Each scattering structure is modeled as PEC. In all simulations the counterpoise is assumed to have no finite thickness.

4.2 Intrinsic Bearing Error of CVOR/DVOR Systems

In this test, both the old OUNPPM and the new OUNPPM were used to simulate the intrinsic bearing error of the CVOR and DVOR systems. The parameters of the CVOR and DVOR ground stations and flight profile are given in Table 4-1. Although as mentioned previously the CVOR/DVOR systems operate in the 112 MHz-117.95 MHz part of the band allocated for CVOR/DVOR systems, the simulations below were run at 108 MHz. This choice will not significantly affect the results. The model allows for selecting frequencies from 108 MHz – 117.95 MHz in 0.50 MHz increments. The intrinsic bearing error in both CVOR and DVOR systems that will be modeled by the OUNPPM (old and new) is mainly due to the counterpoise, the configuration of the CVOR/DVOR ground station antennas above the counterpoise, and reflection from the ground. The ground station antennas are assumed to operate independently of each other and therefore the effects of coupling between the antennas is not modeled. Ideal site conditions were assumed for this initial simulation i.e., no multipath from any scatterer was simulated. Thus in this simulation the field ($\mathbf{E}_{TOTAL}$) as given by equation (3-2) is equal to $\mathbf{E}_{UTD}$ of equation (3-1), i.e., $\mathbf{E}_{PO,\ SCAT}$ is equal to zero. With reference to Figure 3-1 only fields represented by rays 1, 2, 3, 4, and 5 are simulated. $\mathbf{E}_{TOTAL}$ due to all the CVOR and DVOR antennas are then processed following the steps outlined in section 3.2.1.4 and section 3.2.1.5 to compute the bearing of the receiver. The CVOR and DVOR bearing errors are then computed by applying equation (3-31) and equation (3-43) respectively.

Table 4-1

Test parameters for test 1

Parameter	Value
Frequency of operation	108 MHz
Diameter of CVOR/DVOR counterpoise	150 feet
Distance of CVOR ground station antennas from center of counterpoise (d)	22.5 electrical degrees at CVOR operating frequency, i.e., 0.56 feet
Distance of DVOR ground station sideband antennas from center of counterpoise (d)	22 feet
Height of counterpoise above terrain (H_C)	12 feet
Ground type	PEC
Height of antenna above counterpoise (H_A)	4 feet
Flight Type	Orbital (0 -360 degrees)
Flight Parameters	10 nmi from CVOR/DVOR ground station and an altitude of 3000 ft.

Figure 4-1 and Figure 4-2 show the CVOR ground station intrinsic error using the old and the new OUNPPM respectively. Whilst the old OUNPPM yields an identically zero bearing error for all the points in the fight profile, the new OUNPPM produces the expected octantal error with a peak to peak variation of about 0.8 degrees. The CVOR intrinsic error shown in Figure 4-2 is due to the displacement of the CVOR ground station antennas from the center of the counterpoise. The antennas are displaced from the center of the counterpoise in order to achieve the cardioid pattern required for the operation of the CVOR system. Due to the offset of the antennas from the center of the counterpoise however, the far zone azimuth radiation pattern of each CVOR ground station antenna is not a perfect circle, and consequently the CVOR ground station composite azimuth radiation pattern is not a perfect cardioid.

Figure 4-3 and Figure 4-4 present the intrinsic error of the DSB DVOR system using the old and new OUNPPM respectively. Just as in the case of the CVOR intrinsic error, the old OUNPPM produces a zero error for all azimuths of the flight profile. Although the new OUNPPM also produces an insignificant intrinsic error (almost zero), it can be observed that it is quadrantal (four peaks). Again this should be expected because the error of the SSB DVOR has a duantal (two peaks) [16] due to the counterpoise modulation on the sideband RF (i.e., from the circular antenna array), and since the new OUNPPM analyzes the DSB DVOR as a superposition of two SSB DVORs, an error profile with 4 peaks (quadrantal) is produced for the DSB DVOR. Thus the new OUNPPM produces results which are a more accurate representation of the intrinsic errors in actual CVOR/DVOR systems than the results produced by the old OUNPPM.

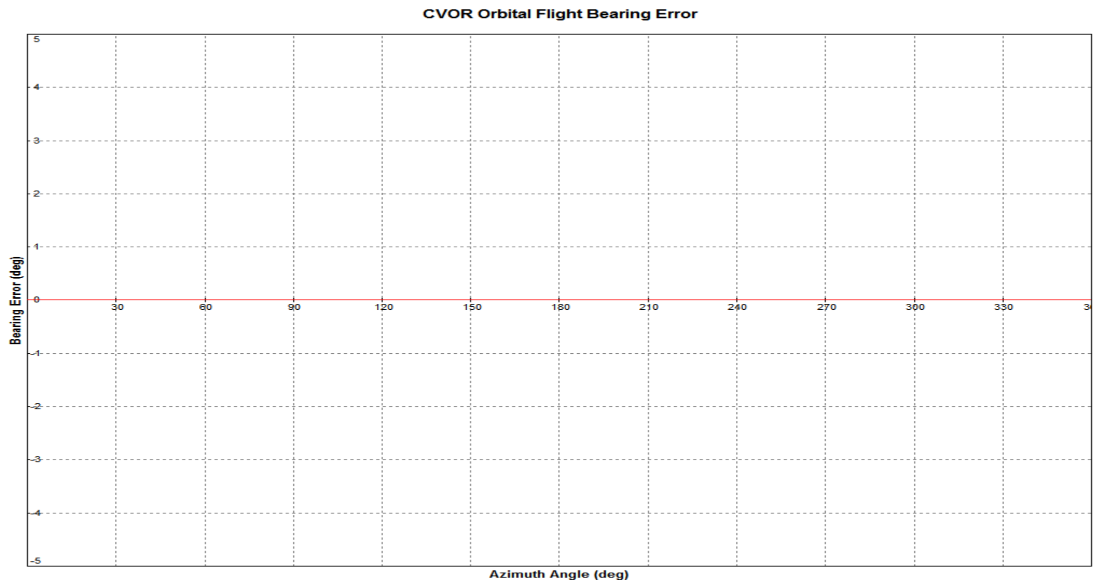

Figure 4-1. CVOR intrinsic error using old OUNPPM (i.e., zero error).

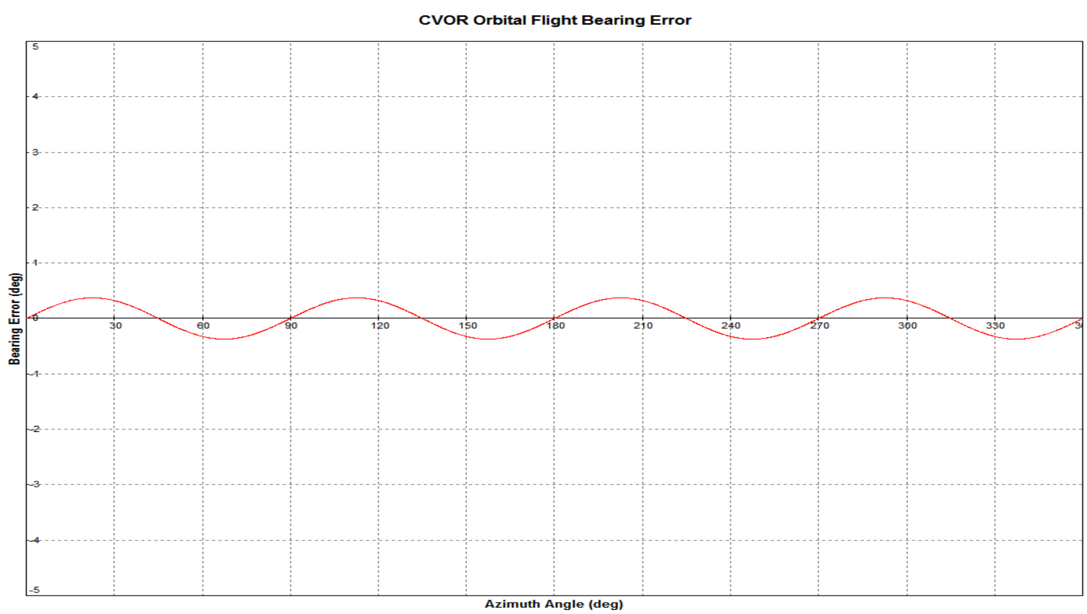

Figure 4-2. CVOR intrinsic error using new OUNPPM.

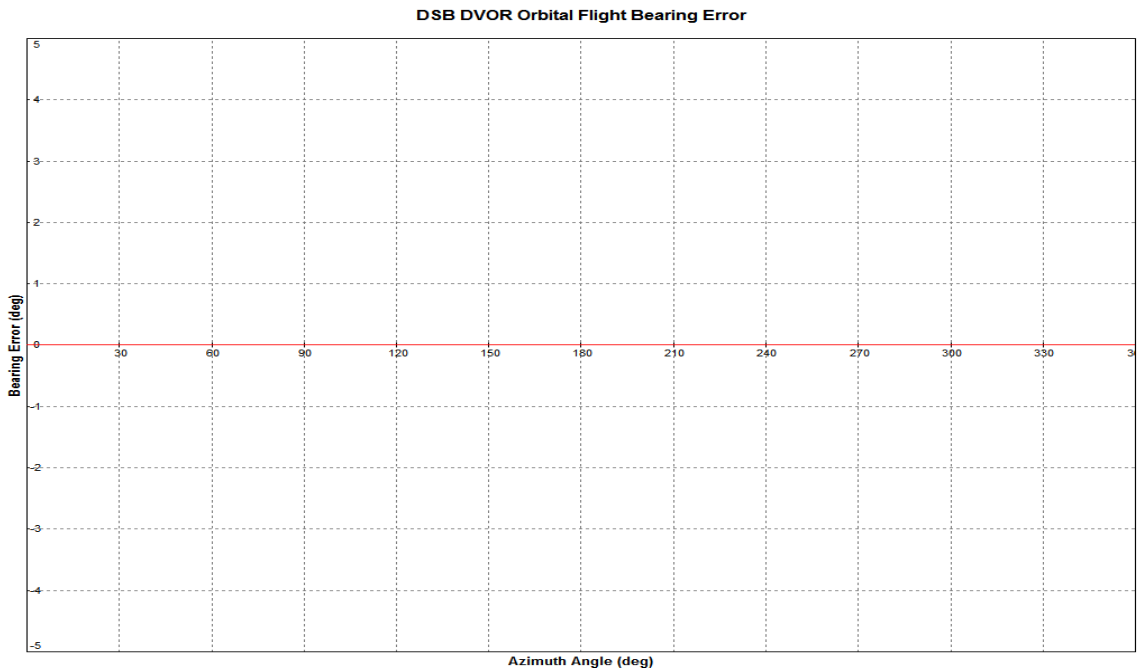

Figure 4-3. DSB DVOR intrinsic error using old OUNPPM (i.e., zero error).

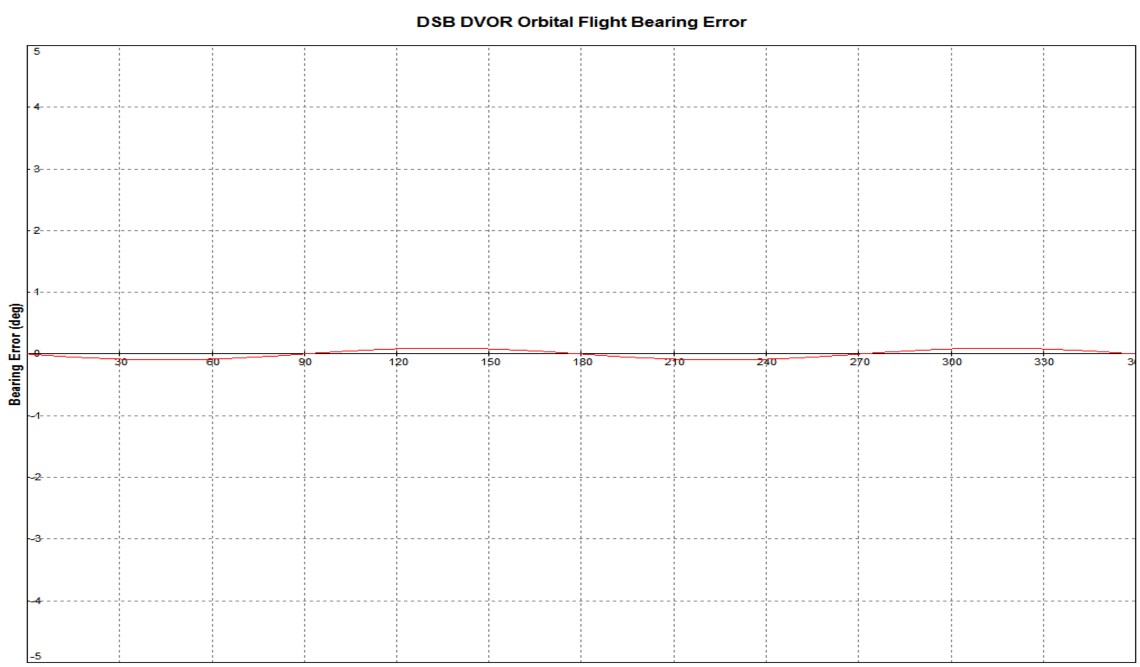

Figure 4-4. DSB DVOR intrinsic error using new OUNPPM.

4.3 Bearing Errors due to Multipath

4.3.1 Bearing Errors due to Multipath from a 100 ft by 100 ft Plate Scatterer Placed 600 ft North of the CVOR/DVOR Ground Station and Oriented Perpendicular to the North Radial. As stated in section 1.2 of this document, a major motivation for this thesis was to improve the accuracy of the OUNPPM in predicting bearing errors caused by scattering from structures located in the vicinity of the CVOR/DVOR ground stations. In this test the effects of multipath on the CVOR system and the DVOR system performance was simulated using the new OUNPPM with the old OUNPPM as a baseline. A 100 ft by 100 ft square PEC plate scatterer oriented perpendicular to the north radial of the ground station and located 600 feet from the CVOR /DVOR ground station is used in these simulations. All other CVOR/DVOR ground station parameters, and flight profile are the same as those given in Table 4-1. With reference to Figure 3-1, fields represented by rays 1-11 are all simulated. Thus the total field that arrives at the receiver is given by $\mathbf{E}_{TOTAL}$ of equation (3-2) where in this case $\mathbf{E}_{PO,\,SCAT}$ in (3-2) is not zero. For the CVOR, the audio-phase of concept of section 3.2.1.4 is applied to $\mathbf{E}_{TOTAL}$ from all the antennas to compute the bearing of the receiver. The bearing error is computed using equation (3-31). For the DSB DVOR, the bearing is computed by applying the DVOR receiver processing method outlined in 3.2.1.5 and the bearing error is computed via equation (3-43). The CVOR bearing errors simulated using the old OUNNPM and the new OUNPPM are presented in Figure 4-5 and Figure 4-6 respectively.

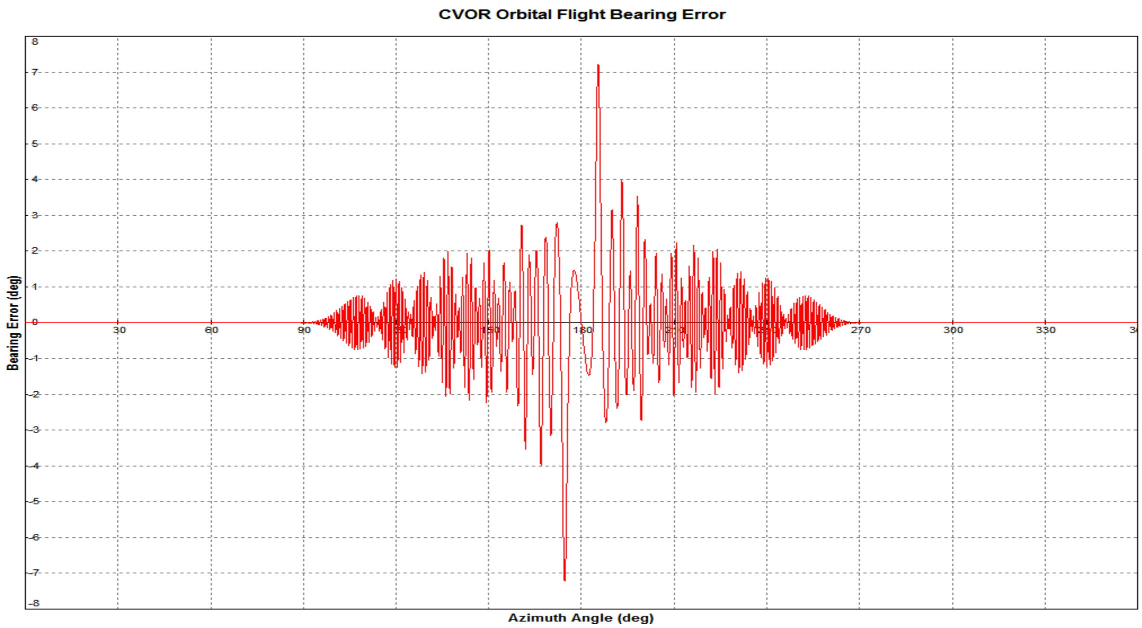

Figure 4-5. CVOR bearing error using old OUNPPM with 100 ft by 100 ft plate scatterer located 600 ft north of the ground station and oriented perpendicular to the north radial.

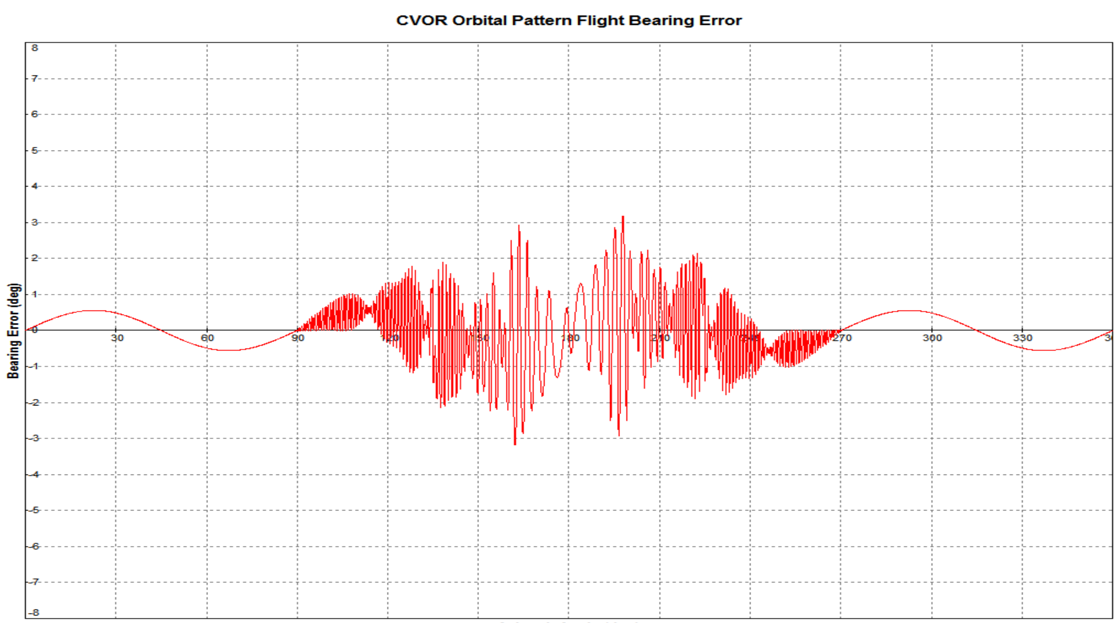

Figure 4-6. CVOR bearing error using new OUNPPM with 100 ft by 100 ft plate scatterer located 600 ft north of the station and oriented perpendicular to the north radial.

As shown in Figure 4-6 the new OUNPPM produces a maximum bearing error of approximately ±3 degrees for a CVOR ground station radiating in the presence of the scatterer whilst as presented in Figure 4-5 the old OUNPPM produces a maximum bearing error approximately ±7 degrees. Moreover between the 0 and 90 degrees azimuths, and between 270 and 360 degrees azimuths, the bearing error as simulated by new OUNPPM (Figure 4-6) is mainly the intrinsic CVOR station error. Based on earlier discussions given simulation 1, this intrinsic CVOR station error is absent between the 0 and 90 degrees, and 270 and 360 degrees azimuths with the simulation using the old OUNPPM as shown in Figure 4-5. As can be also seen in Figure 4-5 and Figure 4-6, the effect of the scatterer is more pronounced between the 90 and 270 degrees azimuths. Since the old OUNPPM was reported to erroneously predict higher bearing errors for the CVOR system, the results of the simulation in Figure 4-6 using the new OUNPPM points in the direction this improvement effort (thesis) was intended to achieve. To determine contribution of *only* the multipath (scatterer) to the CVOR bearing error in the new OUNPPM simulations, the results presented in Figure 4-6 were normalized with the CVOR intrinsic error of Figure 4-2. The normalized CVOR multipath error is presented in Figure 4-7 below. The normalized CVOR multipath error has a maximum of about ±3.5 degrees.

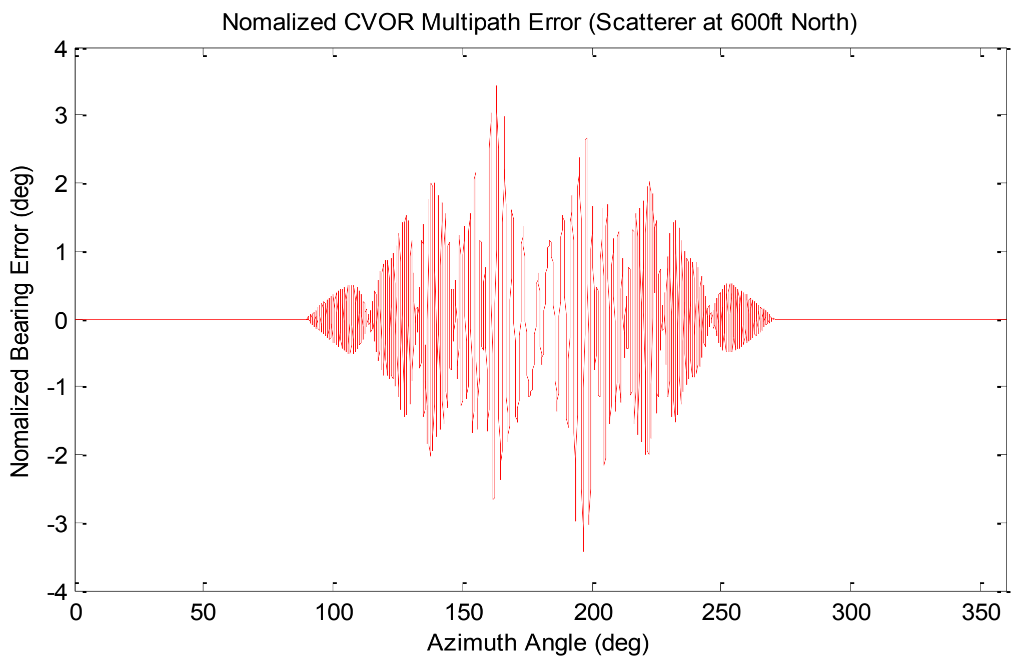

Figure 4-7. Normalized CVOR bearing error using new OUNPPM with 100 ft by 100 ft plate scatterer located 600 ft north of the station and oriented perpendicular to the north radial.

Next the old OUNPPM and new OUNPPM are used to simulate the bearing error of a DVOR station operating in the vicinity of the scatterer. The DVOR bearing errors simulated using the old OUNPPM as presented in Figure 4-8 provides a baseline for comparison with the DVOR bearing errors simulated with the new OUNPPM whose results are presented in Figure 4-9.

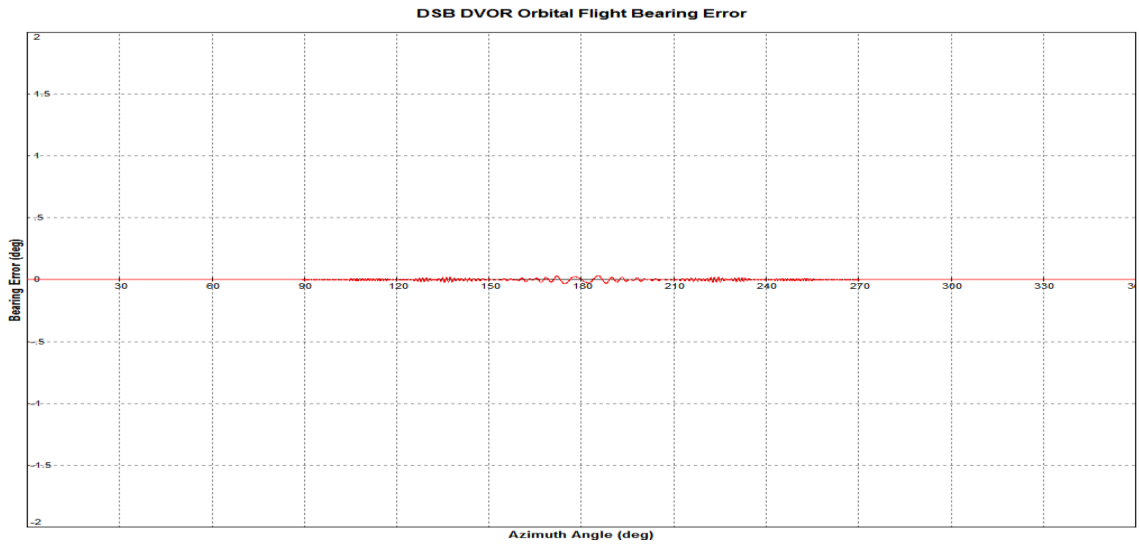

Figure 4-8. DSB DVOR bearing error using old OUNPPM with 100 ft by 100 ft plate scatterer located 600 ft north of the ground station and oriented perpendicular to the north radial.

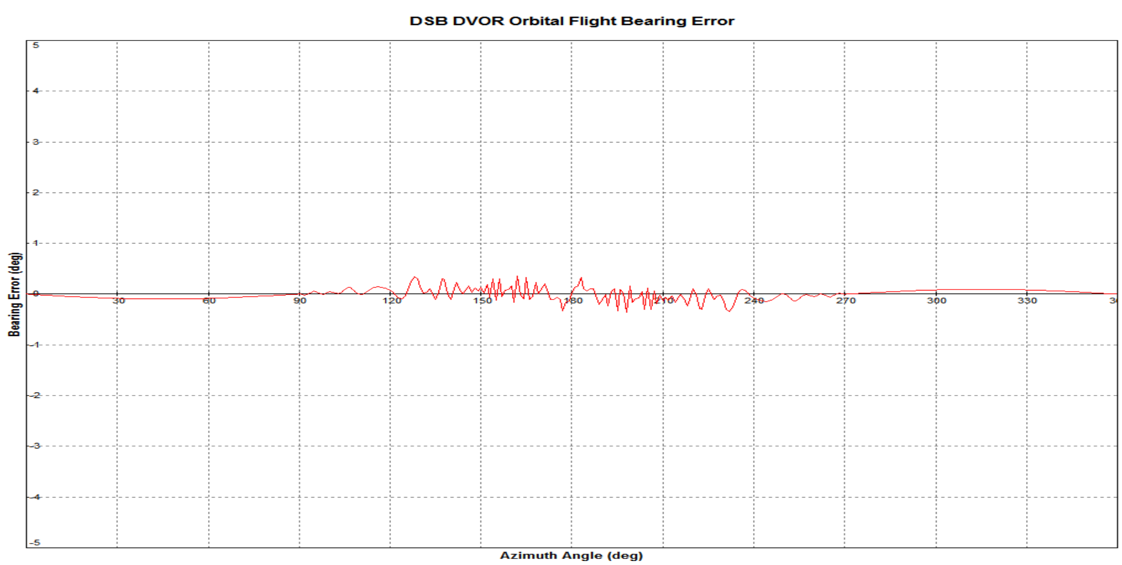

Figure 4-9. DSB DVOR bearing error using new OUNPPM with 100 ft by 100 ft plate scatterer located 600 ft north of the ground station and oriented perpendicular to the north radial.

The new OUNPPM produces a maximum bearing error of ±0.35 degrees as shown in Figure 4-9 for the DVOR system radiating in the presence of the scatterer compared to the less than ±0.05 degrees maximum bearing as shown in Figure 4-8 simulated with the old OUNPPM. Note that as with CVOR, the effect of the scatterer on the DVOR station performance is only dominant between the 90 and 270 degrees azimuths. The new OUNPPM simulation (Figure 4-9) also shows the intrinsic station error between the 0 and 90 degrees azimuths, and between the 270 and 360 degrees azimuths. However the old OUNPPM simulation (Figure 4-8) fails to show the intrinsic station error between the 0 and 90 degrees azimuths, and the 270 and 360 degrees. Since the old OUNPPM was reported to erroneously predict lower bearing errors for the DVOR system, the general trend of the results presented in Figure 4-8, and Figure 4-9 indicate that the performance of new OUNPPM points in the direction this improvement effort (thesis) was intended to achieve. The results of Figure 4-9 are normalized with the systematic error of Figure 4-4 in order to determine the contribution of the scatterer to the error presented in Figure 4-9. The normalized error is shown in Figure 4-10 below. This normalized DSB DVOR error has a maximum of ±0.35.

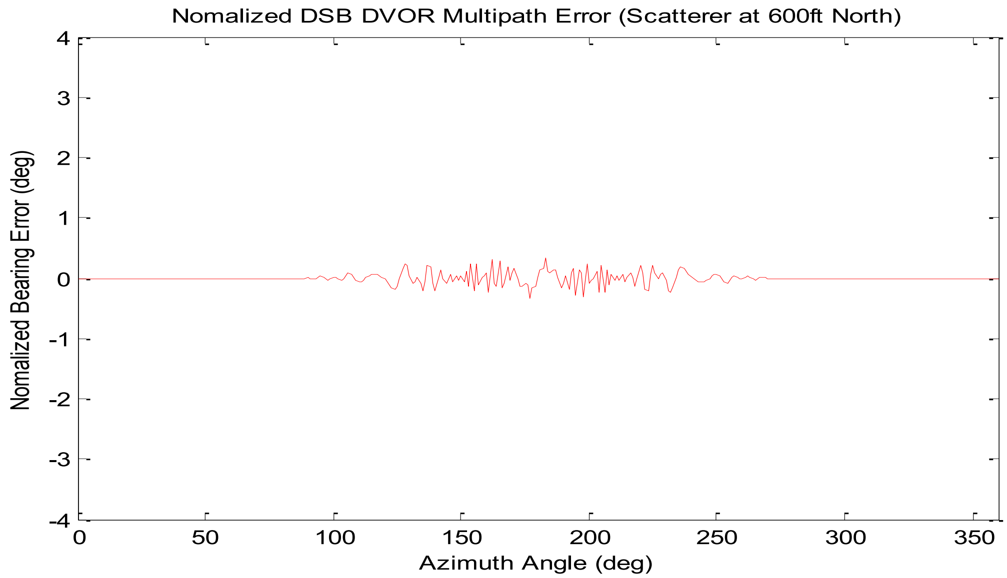

Figure 4-10. Normalized DSB DVOR bearing error using new OUNPPM with 100 ft by 100 ft plate scatterer located 600 ft north of the ground station and oriented perpendicular to the north radial.

4.3.2 Bearing Errors due to Multipath from a 100 ft by 100 ft Plate Scatterer Placed 1000 ft South of the CVOR/DVOR Ground Station and Oriented Perpendicular to the South Radial. The parameters of this test are similar to those of test 2, except that the position of the plate scatterer relative to the CVOR/DVOR ground station has been changed. In this test both the old and new OUNPPM are used to simulate CVOR and DVOR bearing errors due to a 100 feet by 100 feet plate placed 1000 feet south of the CVOR/DVOR ground station. With reference to Figure 3-1, fields represented by rays 1-11 are all simulated. The CVOR bearing error results of simulations using the old and new OUNPPM are presented in Figure 4-11 and Figure 4-12 respectively.

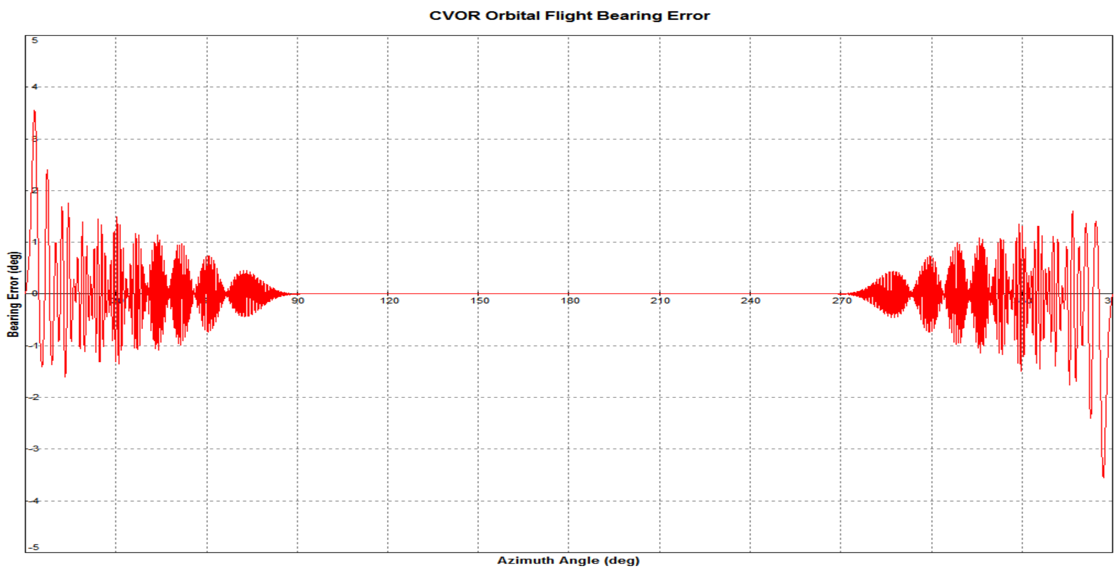

Figure 4-11. CVOR bearing error using old OUNPPM with 100 ft by 100 ft plate scatterer placed 1000 ft south of ground station and oriented perpendicular to south radial.

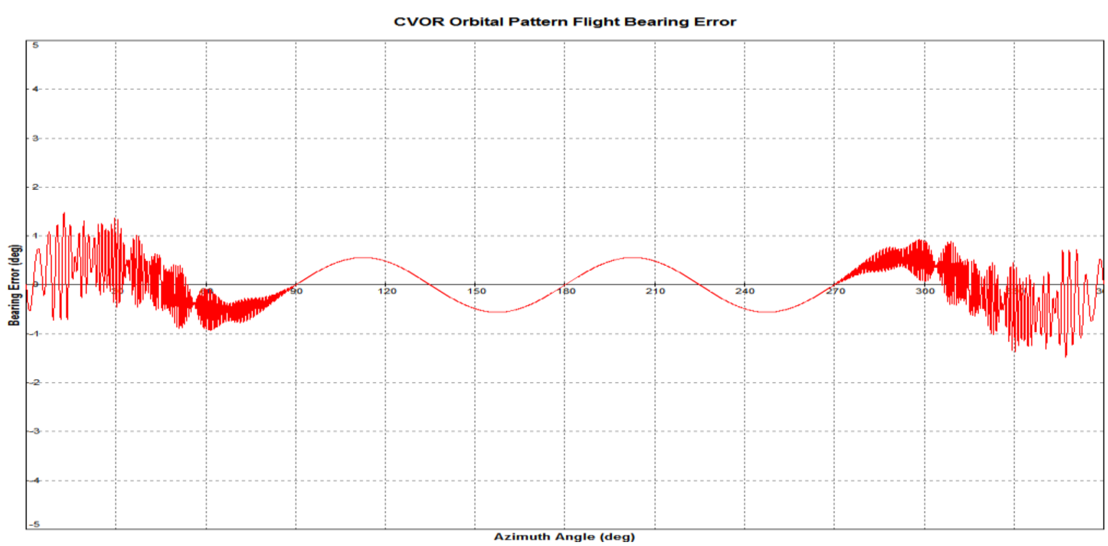

Figure 4-12. CVOR bearing error using new OUNPPM with 100 ft by 100 ft plate scatterer placed 1000 ft south of ground station and oriented perpendicular to south radial.

The simulation with the old OUNPPM (Figure 4-11) produces a CVOR peak bearing error of about 3.5 degrees at radials of approximately 3 degrees, and 357 degrees. The error is dominant between the 0 and 90 degrees, and 270 and 360 degrees radials. Between the 90 and 270 degrees, the bearing error is zero. The new OUNPPM simulation (Figure 4-12) however produces a peak CVOR bearing error of 1.5 degrees at radials of approximately 13 degrees and 347 degrees. As with the old OUNPPM simulation the bearing error is more dominant between the 0 and 90 degrees, and 270 and 360 degrees radials. However note that the bearing error between the 90 and 270 degrees radials in this case in not zero. Between the 90 and 270 degrees radials, the station exhibits the intrinsic CVOR system error. Hence again, the new OUNPPM produces a five-fold reduction in the CVOR error, and thus results are in consonance with what was expected from this improvement effort. As with previous cases the results of Figure 4-12 are normalized with the CVOR intrinsic error of Figure 4-2. The normalized multipath error with a peak of ±1.1 degrees is presented in Figure 4-13 below.

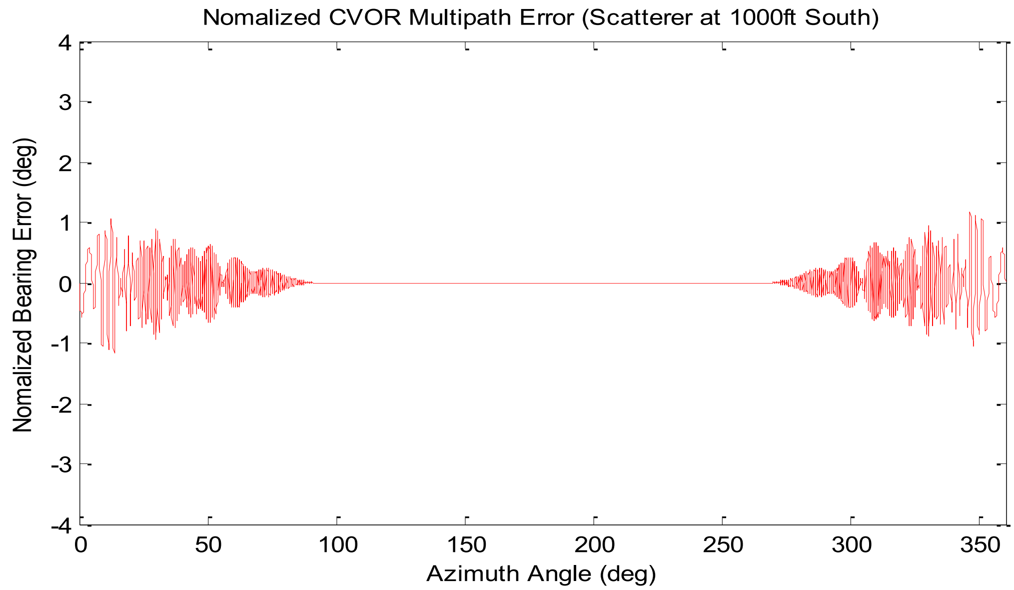

Figure 4-13. *Normalized* CVOR bearing error using new OUNPPM with 100 ft by 100 ft plate scatterer placed 1000 ft south of ground station and oriented perpendicular to south radial.

The DVOR bearing error results of simulations using the old and new OUNPPM are presented in Figure 4-14 and Figure 4-15 respectively.

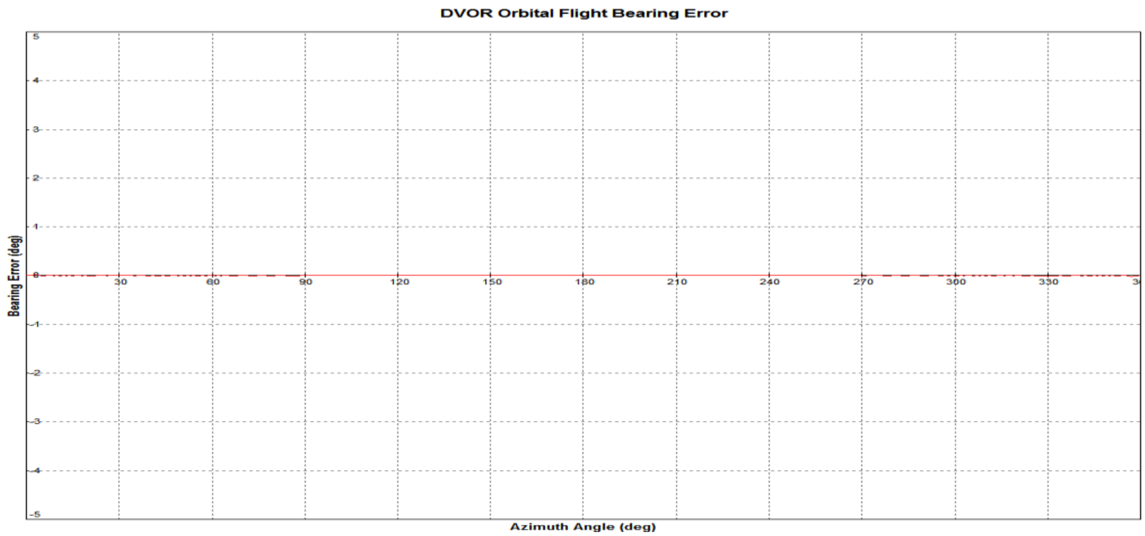

Figure 4-14. DSB DVOR bearing error using old OUNPPM with 100 ft by 100 ft plate scatterer placed 1000 ft south of ground station and oriented perpendicular to south radial.

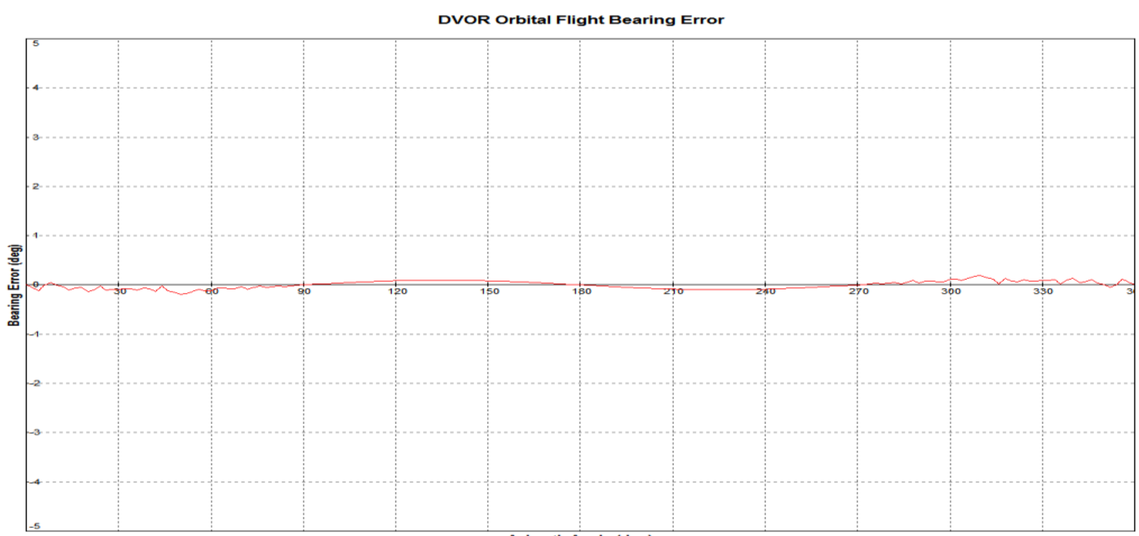

Figure 4-15. DSB DVOR bearing error using new OUNPPM with 100 ft by 100 ft plate scatterer placed 1000 ft south of ground station and oriented perpendicular to south radial

As shown in Figure 4-14 the old OUNPPM predicts a zero DSB DVOR bearing error between the 90 and 270 degrees azimuths and an insignificant error ripple between the 0 and 90 degrees azimuths, and the 270 and 360 degrees azimuths. The new OUNPPM on the other hand yields a maximum DSB DVOR bearing error of approximately ±0.2 degrees (Figure 4-15). The effect of the scatterer is present between the 0 and 90 degrees, and 270 and 360 degrees radials. Between the 90 and 270 degrees radials, the new OUNPPM exhibits the DVOR system intrinsic error. Akin with the results of simulation 2, the new OUNPPM produces a higher bearing error, as compared with the old OUNPPM simulation. The normalized DSB DVOR multipath error is presented in Figure 4-16 below. The maximum is about ±0.17 degrees.

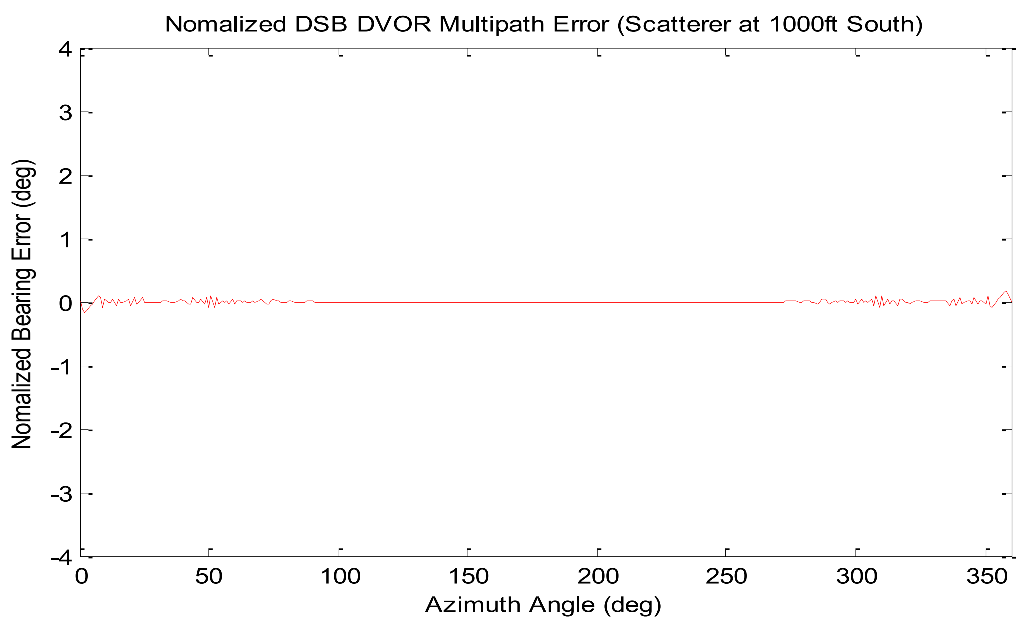

Figure 4-16. Normalized DSB DVOR bearing error using new OUNPPM with 100 ft by 100 ft plate scatterer placed 1000 ft south of ground station and oriented perpendicular to south radial.

4.3.3 New OUNPPM Simulation of Multipath for a CVOR Ground Station Mounted over Snow Covered Ground. The new OUNPPM was used in this test to simulate the CVOR system bearing error caused by multipath from a 100 ft by 100 ft plate scatterer placed 600 ft north of the CVOR ground station and oriented perpendicular to the north radial. However in this case the ground was assumed to be covered in snow. A relative electric permittivity of 15 and a conductivity of 10^{-4} S/m were assumed for snow. Thus, the ground reflection coefficient in this case will be different from the PEC case of simulation 3. With reference to Figure 3-1, rays 1-11 were simulated. The simulation results are shown in Figure 4-17 below.

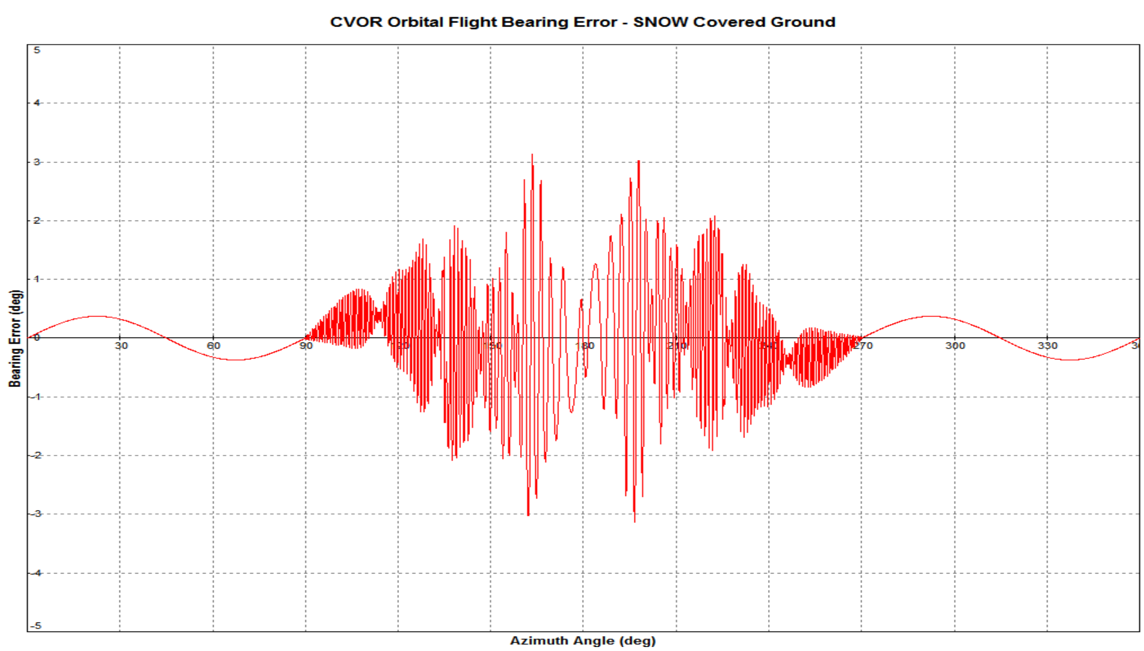

Figure 4-17. CVOR bearing error using new OUNPPM with 100 ft by 100 ft plate scatterer located 600 ft north of the ground station and oriented perpendicular to the north radial. The ground in the vicinity of the ground station is covered in snow.

The results for the snow covered ground in Figure 4-17 are not significantly different from the case where the ground was PEC (Figure 4-6). Both have a peak bearing error of about 3 degrees, and the error is more dominant between the 90 and 270 degrees azimuths. There are however a few subtle differences in the profiles of the of the error curves (snow and PEC). Note that since both the CVOR ground and scatterer are over the same medium (snow or PEC), changing the composition of the ground does not significantly change the magnitude of the bearing errors.

4.4 CVOR/DVOR Coverage Analysis

CVOR/DVOR coverage analysis was conducted to investigate the maximum distance from the CVOR/DVOR ground station at which the CVOR/DVOR ground station signal can be used for various configurations of CVOR/DVOR ground stations. This maximum distance at which the CVOR/DVOR signal level falls below the minimum detectable threshold depends on the configuration of the CVOR/DVOR ground station. For sites with many scatterers e.g., buildings, trees etc., the CVOR/DVOR system ground station counterpoise and antenna array are usually raised high above the terrain so as to reduce the effect multipath from the scatterers. Raising the CVOR/DVOR counterpoise, with the height of the Alford loops above the counterpoise maintained, however results in more lobes or nulls in far zone elevation plane pattern of the fields radiated from the CVOR/DVOR ground station. The formation of these additional lobes as the height of the counterpoise above the ground is increased is referred to as scalloping [25]. Scalloping is due to multipath from the ground. Scalloping and signal fading effects can combine to cause the CVOR/DVOR signal level to fall below the detection threshold at some flight points which coincide with the nulls. Increasing the size of the counterpoise reduces the degree of scalloping in the far zone electric field pattern. However supporting a very large counterpoise at high heights above the ground is not a simple task. Apart from the expense in building the supporting structure, large counterpoises can also be affected by high-speed winds.

The new OUNPPM can be used to determine the size of the counterpoise, and at what height it should be raised above the ground in order for the CVOR/DVOR ground station to be able to provide usable/detectable signals over its entire service volume. Figure 4-18 shows far zone radial flight radiation patterns at an altitude of 3500 feet above MSL, for different counterpoise heights above an infinite, PEC ground plane. A 150 foot diameter counterpoise was used in these simulations. In these coverage analyses, the field intensities are simulated for two diametrically opposite antennas each displaced 22 feet from the center of the counterpoise. The radial flight simulated is in the same vertical plane as the diametrically opposite antennas. The fields simulated in this test are those represented by rays 1-5 in Figure 3-1 or alternatively the field given in equation (3-1). Thus multipath field was simulated in this analysis.

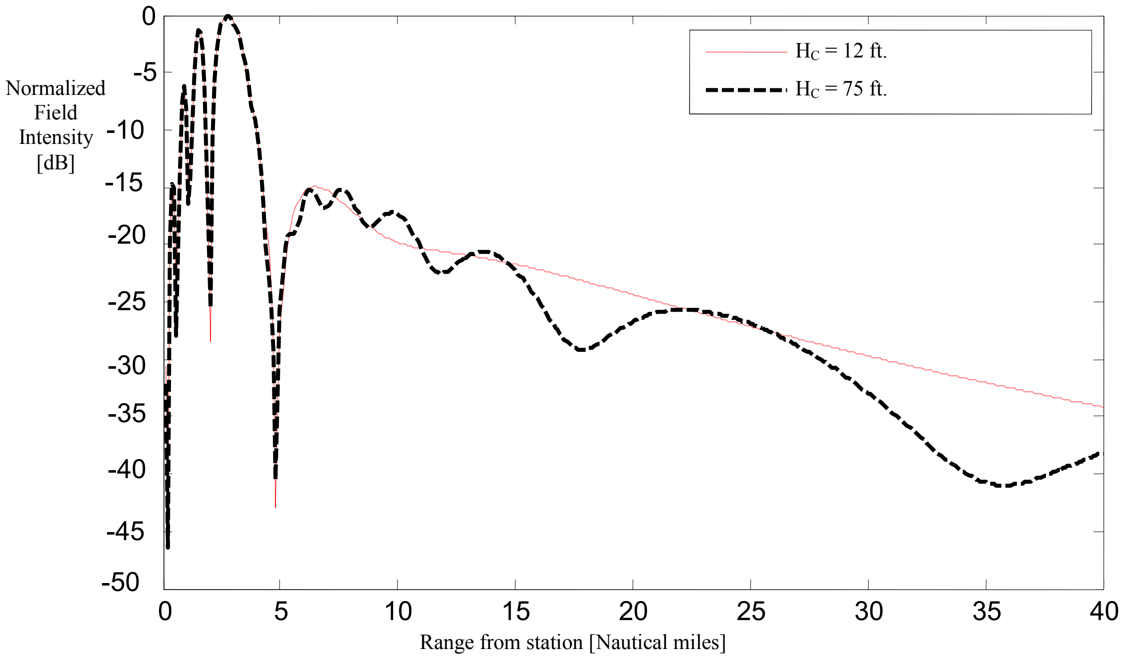

Figure 4-18. CVOR/DVOR radial flight pattern for counterpoise at different heights above a PEC, ground without scatterer.

The results presented in Figure 4-18 show that at a counterpoise elevation of 75 feet above terrain, there is more scalloping than at a counterpoise elevation of 12 feet. Therefore unless the CVOR/DVOR ground station site has scatterers so located that there interfere with the proper operation of the CVOR/DVOR system, a counterpoise raised 12 feet above MSL will be preferred to a counterpoise raised 75 feet above MSL.

However if the CVOR/DVOR site is such that the elevation of the counterpoise above ground must be 75 feet, the new OUNPPM can be used to determine what size of counterpoise will produce acceptable scalloping. Figure 4-19 presents the new OUNPPM simulation of the radial flight far zone electric field pattern for a CVOR/DVOR ground station with different sizes of counterpoise elevated 75 feet above the ground.

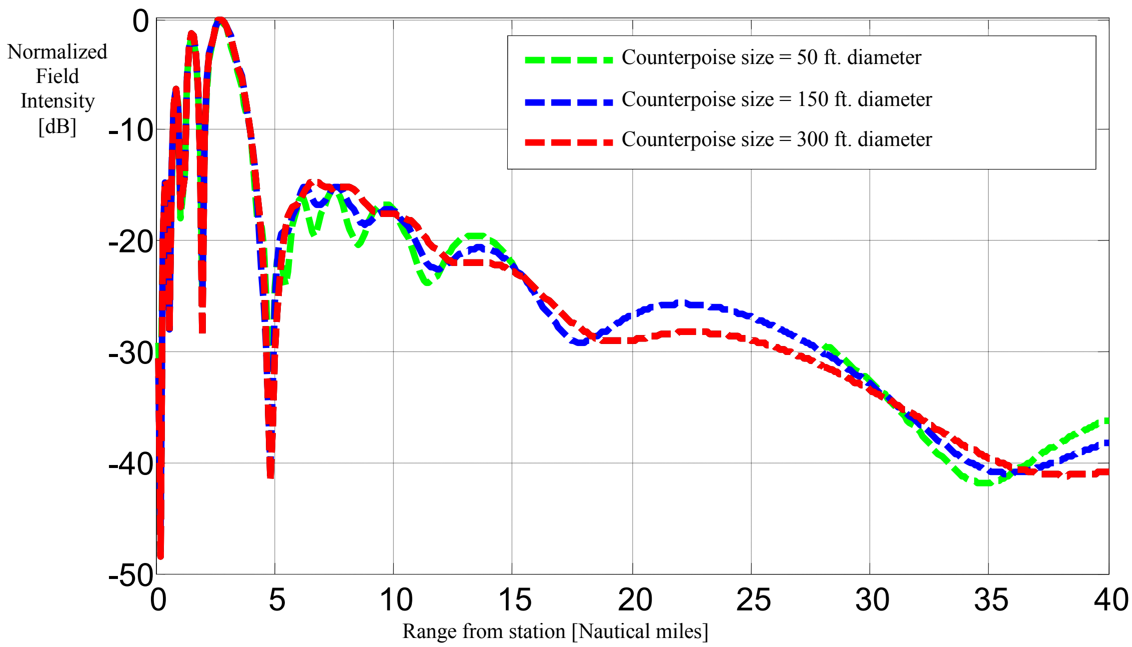

Figure 4-19. CVOR/DVOR ground station coverage for different counterpoise sizes at constant height above a PEC, ground.

As can be observed in Figure 4-19, a counterpoise of diameter 300 feet produces a relatively less scalloping as compared to counterpoises of 50 feet or 150 feet diameters.

4.5 Validation

This section outlines the validation of the new OUNPPM developed in this thesis. The inability to obtain actual field results from flight tests or CVOR/DVOR ground check monitors has restricted the validation of the new OUNPPM to other simulation means presented here. Validation of the new OUNPPM was carried out by using the Numerical Electromagnetics Code - Basic Scattering Code (NEC -BSC) version 4.2. The NEC-BSC is a “user-oriented computer code” [21] based on UTD, that can be used to predict the high frequency scattering of electromagnetic fields by scatterers in the field-of-view of a source e.g., antenna [21]. The scatterers in NEC-BSC are modeled as PEC structures [21]. Amongst other capabilities NEC-BSC can be also be used to investigate coupling between two or more electromagnetic field sources radiating in proximity [21].

In the development of the new OUNPPM, second order effects such as electromagnetic coupling between the Alford loops of the CVOR/DVOR ground station were not modeled. Therefore the CVOR/DVOR ground station antenna array consists of a group of “isolated” antennas radiating in the presence of a flat, circular counterpoise and an infinite ground. Hence the combined field at an observation point is the superposition of the fields from all the antennas of the CVOR/DVOR ground station antenna array. Thus validation for a single antenna therefore suffices for validation of the entire antenna array within the scope of this thesis. The PO scattering model previously used in the OUNPPM was not as validated using NEC-BSC since PO is different from UTD which is the high frequency electromagnetic technique on which NEC-BSC is based. In NEC-BSC simulations, the Alford loop antenna of the CVOR/DVOR ground station was modeled as an infinitesimal magnetic dipole. From [23], the far-zone electric field of a small loop antenna is equivalent to that infinitesimal magnetic dipole. The CVOR/DVOR counterpoise in NEC-BSC simulations was modeled as a flat polygonal plate with 24 sides. The following configurations will be validated.

4.5.1 Configuration 1: Single Alford Loop Centered 4 ft above a PEC Counterpoise in Free Space. This configuration as illustrated in Figure 4-20 represents the model of the DVOR ground system center antenna. The parameter of interest for this configuration is the elevation plane far zone radiation pattern. In the configuration of Figure 4-20 the CVOR ground stations is assumed to be suspended in free space. The elevation plane far zone radiation pattern of the configuration of Figure 4-20 are simulated using the new OUNPPM and the NEC-BSC, and then the results compared. The fields simulated in this validation are those represented by rays 1, 2, and 4 in Figure 3-1. The results are presented in Figure 4-21.

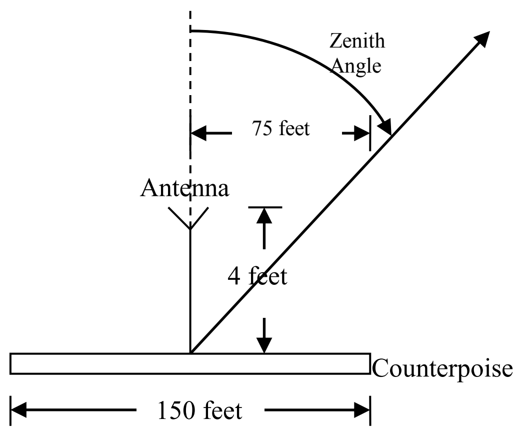

Figure 4-20. Side-view of an Alford loop centered 4ft above a PEC counterpoise in free space.

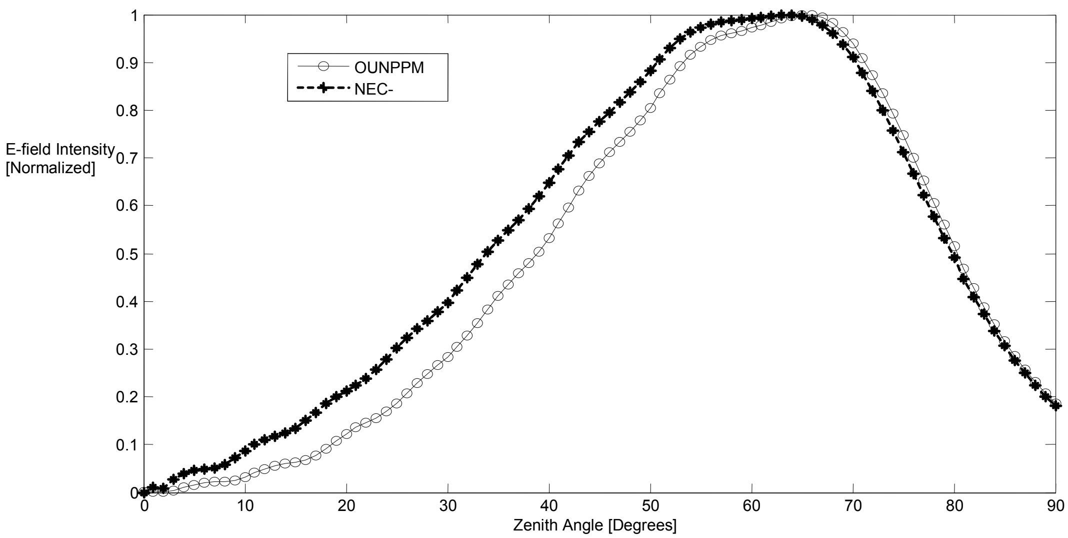

Figure 4-21. Normalized far zone electric field patterns for configuration of Figure 4-20.

Figure 4-21 shows good agreement between NEC-BSC and the new OUNPPM simulations. The variation between the new OUNPPM and NEC-BSC results is due to the shape of the counterpoise used in the NEC-BSC, and the new OUNPPM simulations. In the new OUNPPM, the counterpoise is modeled as a circular PEC plate. In the NEC-BSC simulations, the counterpoise is modeled as a 24-sided regular polygon. The 24-sided polygonal counterpoise model in the NEC-BSC simulations introduces the following effects which are absent in the circular counterpoise model of the new OUNPPM.

1. The corners of the polygon used in the NEC-BSC simulations produce corner-diffracted fields which are incorporated in NEC-BSC by applying corner diffraction terms.
2. The positions of the diffraction points along the edge of the counterpoise are different in the new OUNPPM and NEC-BSC.

4.5.2 Configuration 2: Alford Loop Raised 4 ft above, but Displaced 22 ft from the Center of the PEC Counterpoise. In the second configuration as shown in Figure 4-22, an Alford loop raised above, but displaced from the center of the counterpoise is modeled using both the new OUNNPM and NEC-BSC. This configuration is representative of any of the antennas of the CVOR ground station, and any of the antennas of the DVOR ground station circular antenna array. The new OUNPPM and NEC-BSC are used to simulate the far zone elevation plane radiation pattern of the configuration of Figure 4-22. The results of the simulations are presented in Figure 4-23.

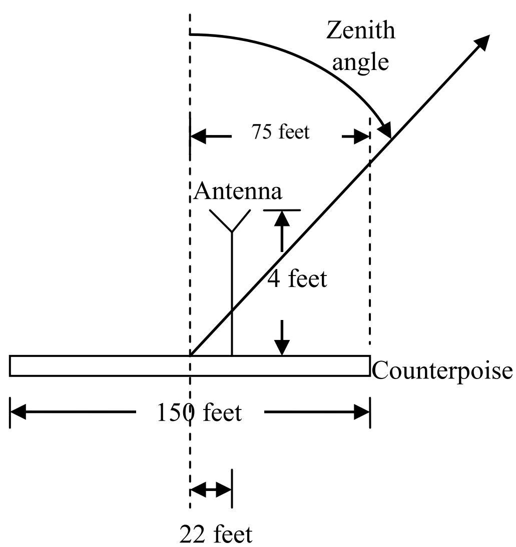

Figure 4-22. Side-view of an Alford loop raised 4 ft but displaced 22 ft from the center, and elevated above a PEC counterpoise in free space.

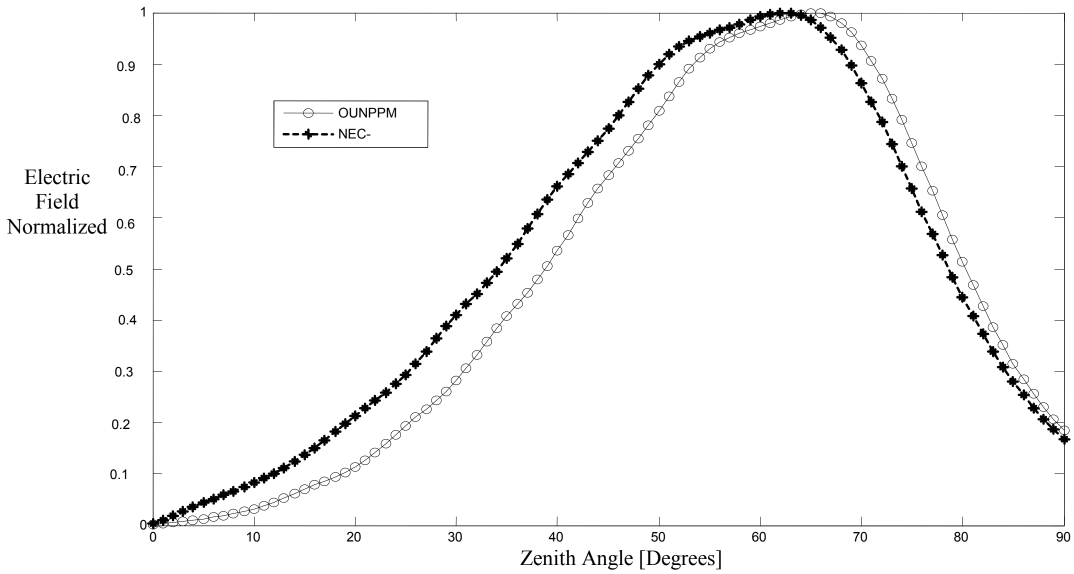

Figure 4-23. Normalized far zone electric field patterns for configuration of Figure 4-22.

As can be seen in the Figure 4-23, the new OUNPPM and NEC-BSC show good agreement. The reasons for the difference between the OUNPPM and NEC-BSC are the same as those given for results of simulating configuration 1.

4.5.3 Configuration 3: Single Alford Loop Centered 4 ft above a PEC Counterpoise Raised 12 ft above an Infinite PEC Ground. Next the new OUNPPM and NEC-BSC are used to simulate the far zone radiation pattern for the configurations shown in Figure 4-24. The configuration of Figure 4-24 is similar to that of Figure 4-20 except that in Figure 4-24 the CVOR/DVOR counterpoise is raised 12 feet above an infinite, flat PEC ground. Rays 1-5 in Figure 3-1 are simulated in this test. Thus there is no multipath from any scatterer. The results for simulating the configuration shown in Figure 4-24 are presented in Figure 4-25.

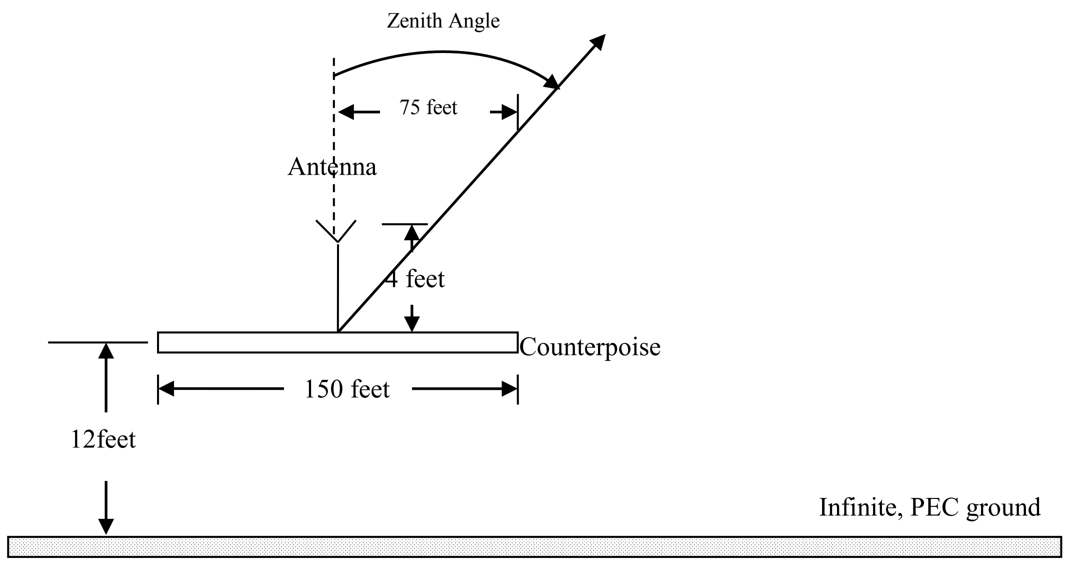

Figure 4-24. Side-view of an Alford loop centered above a counterpoise elevated above an infinite, PEC ground.

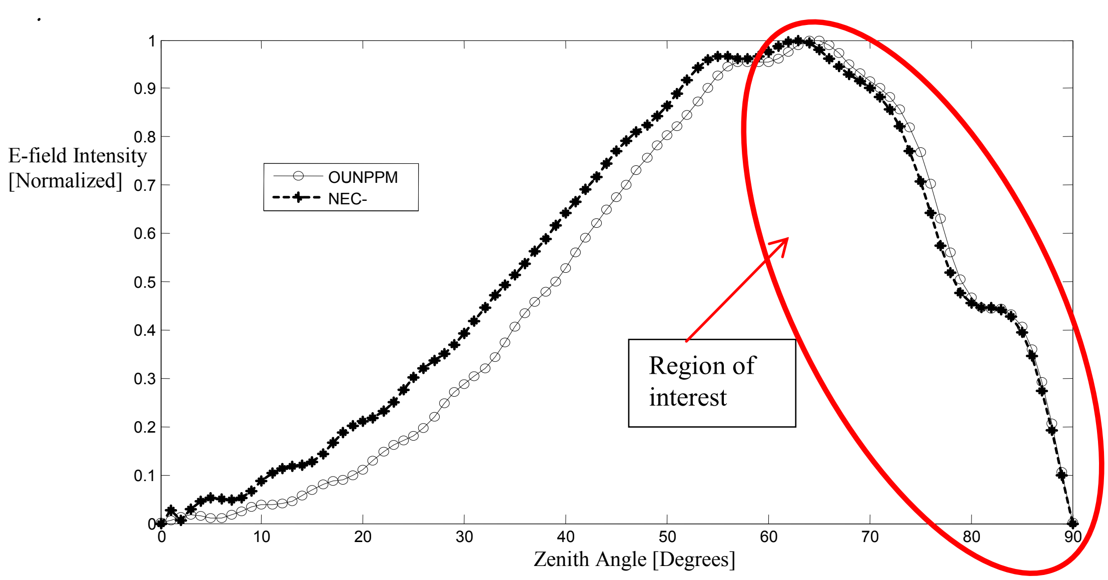

Figure 4-25. Normalized far zone electric field patterns for configuration shown in Figure 4-20, simulated with NEC-BSC and the new OUNPPM.

As can be seen in the Figure 4-25, the new OUNPPM and NEC-BSC show good agreement. The reasons for the difference between the OUNPPM and NEC-BSC are the same as those given for results of simulating configuration 1.

4.5.4 Configuration 4 - Single Alford loop Centered 4 ft above a PEC Counterpoise Raised 12 ft above an Infinite PEC Ground. The new OUNPPM and NEC-BSC are used to simulate the far zone radiation pattern for the configuration illustrated in Figure 4-26. The configuration of Figure 4-26 is similar to that of Figure 4-24 except that in Figure 4-26 the Alford loop is displaced 22 feet from the center of the counterpoise. Rays 1-5 in Figure 3-1 were simulated in this test. The results for simulating the configuration shown in Figure 4-26 are presented in Figure 4-27

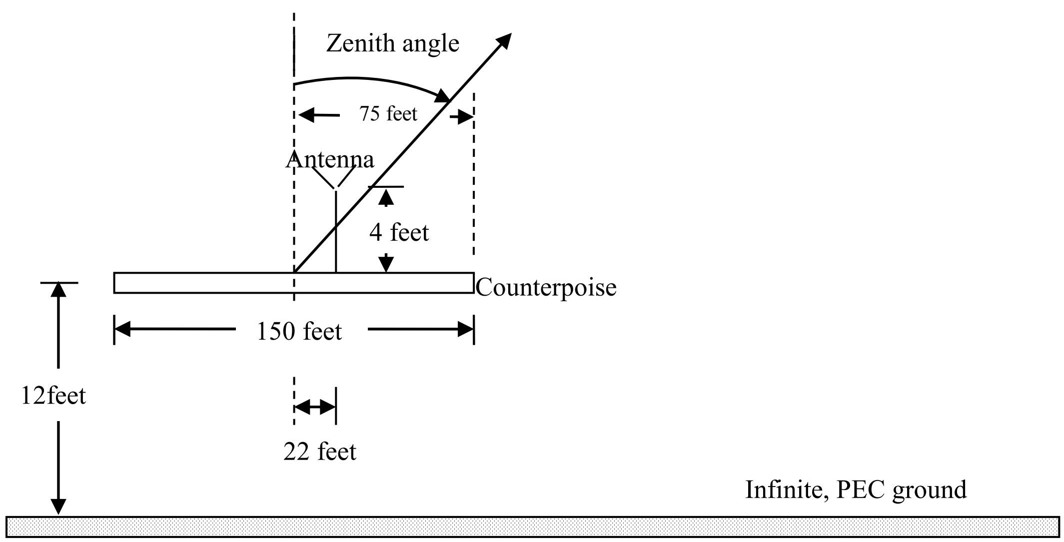

Figure 4-26. Side-view of an Alford loop displaced from the center and elevated above a PEC counterpoise which is elevated above an infinite, PEC ground.

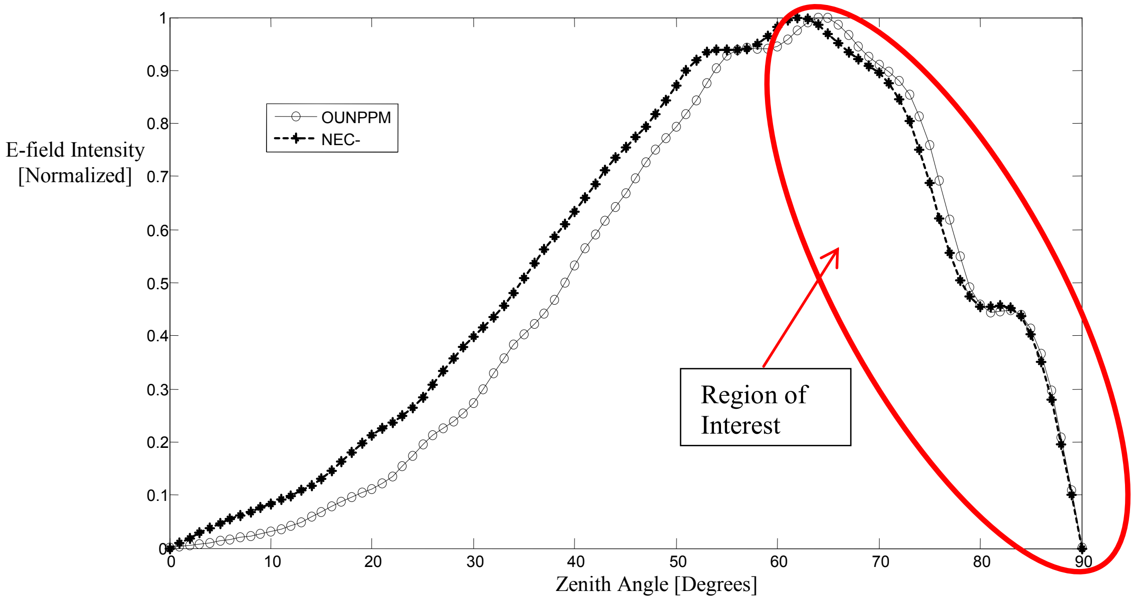

Figure 4-27. Normalized far zone electric field patterns for configuration shown in Figure 4-26 simulated with NEC-BSC and the new OUNPPM.

As can be seen in the Figure 4-27, the new OUNPPM and NEC-BSC show good agreement. The reasons for the difference between the OUNPPM and NEC-BSC are the same as those given for results of simulating configuration 1.

Finally the phase of the far zone electric fields for a 360 azimuth sweep at an elevation of 3 degrees above the horizon for the configuration of Figure 4-28 is simulated with the new OUNPPM and NEC-BSC. There is no scatterer in this simulation and thus fields represented by rays 1-5 in Figure 3-1 are the only fields simulated. Figure 4-28 is a top-view of the configuration of Figure 4-26. Figure 4-29 presents the results of the simulation.

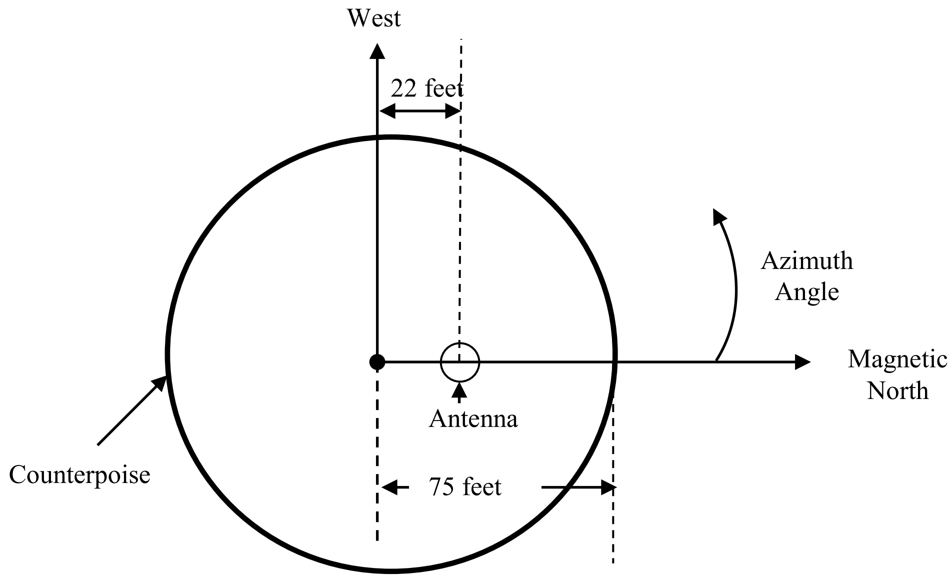

Figure 4-28. Alford loop antenna offset from the center of a counterpoise. Counterpoise is above an infinite, PEC ground (Top-view).

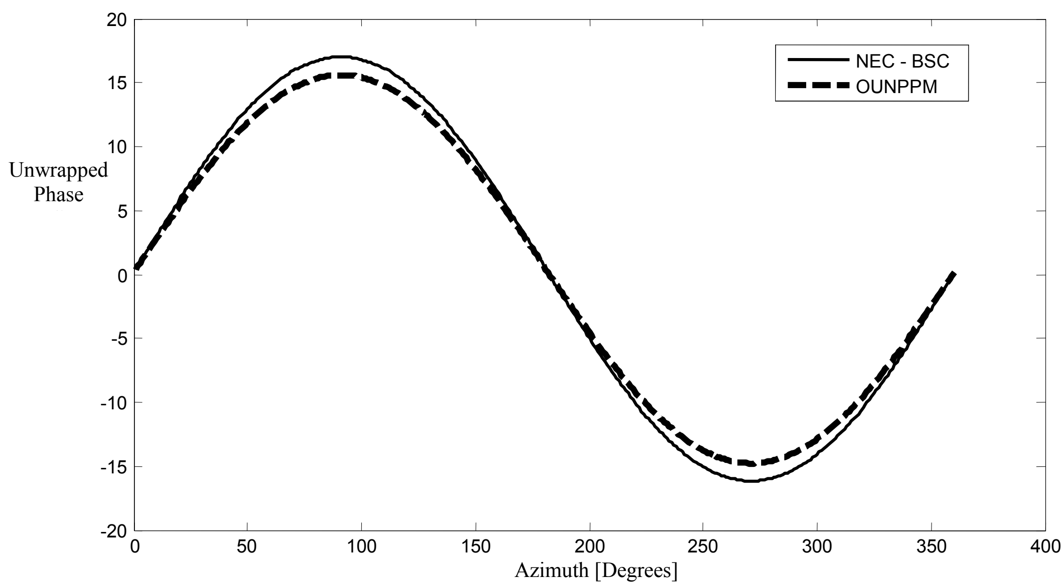

Figure 4-29. Phase of complex far zone electric fields of configuration 4-24 simulated using OUNPPM and NEC-BSC.

As can be seen in the Figure 4-29, the new OUNPPM and NEC-BSC show good agreement. The phase of the fields follow a sinusoidal pattern. This is because the phase of the field is proportional to the range of the observation point from the antenna, and for the orbital flight of Figure 4-28, the distance from the antenna to the observation point has a sinusoid variation with respect to the distance from the antenna to the center of the counterpoise and thus the phase will also exhibit a sinusoidal variation. The reasons for the difference between the OUNPPM and NEC-BSC are the same as those given for results of simulating configuration 1.

Implicit in simulations results of the far zone electric field pattern is the fact that for CVOR/DVOR counterpoises that are not circular, the new OUNPPM model will still predict good results. This is important because the DVOR counterpoise is not necessarily circular. As Figure 4-25 and Figure 4-27 illustrate, there is closer agreement between NEC-BSC and the new OUNPPM at zeniths of 60-90 degrees. It is at these zeniths that the new OUNPPM will typically be used. A suggestion for future improvement of the new OUNPPM will be to quantify the bearing errors that the variation between the results (far zone electric fields) obtained using new OUNPPM and NEC-BSC will cause.

CHAPTER 5: CONCLUSIONS AND RECOMMENDATIONS

5.1 Conclusions

This thesis presents an improvement to an existing CVOR/DVOR error prediction tool (i.e., 'old' OUNPPM). The old CVOR/DVOR error prediction tool of the old OUNPPM modeled the CVOR/DVOR ground station as a single point source mounted above a counterpoise raised at a height above the terrain/local ground. 2-D UTD was applied to compute the fields from the CVOR/DVOR ground station to the receiver/aircraft and any scatterer in the vicinity of the ground stations. The 2-D UTD fields arriving at the scatterer are then applied to a PO scattering model to compute the multipath fields from the scatterer to receiver/aircraft. A receiver model was then implemented to compute the bearing of the receiver/aircraft. It was reported that the old OUNPPM underestimates DVOR system errors and overestimates the CVOR system errors. By remodeling CVOR/DVOR stations using 3-D UTD in this thesis, an improved CVOR/DVOR error prediction model namely the new OUNPPM has been developed. In the new OUNPPM, all the antennas of the CVOR/DVOR ground station were considered, and each antenna was modeled as an Alford loop, which is the radiator/antenna used in actual CVOR/DVOR ground stations. The total complex fields from the ground station and multipath received at the aircraft are subsequently processed to compute the bearing of the aircraft from the ground station. The deviation of the computed bearing from the known true bearing of receiver/aircraft constitutes an error.

The 3-D UTD fields of the new OUNPPM have been validated using NEC-BSC, where it was observed that at low elevation angles (0-60 degrees above the horizon), which is where the CVOR/DVOR systems are typically used – except when they are been used for approach, there was close agreement between the new OUNPPM and NEC-BSC. By using the old OUNPPM as a baseline, simulations were run with new OUNPPM for different scenarios. Results of the simulations showed that whilst the old OUNPPM produced CVOR and DVOR intrinsic station errors of zero for all simulated receiver positions, the new OUNPPM produced an octantal intrinsic station error for the CVOR and a quadrantal error for the DSB DVOR.

The effects of multipath on the performance of the CVOR/DVOR systems was investigated by running simulations with the new OUNPPM, where a single scatterer was placed at two different locations around the CVOR/DVOR ground stations and assuming that the local ground was PEC. By comparing the results obtained from the new OUNPPM simulations with the old OUNPPM baseline, it was observed that the CVOR system bearing errors with the new OUNPPM were relatively lower than those of the old OUNPPM. The new OUNPPM also produced relatively higher DVOR bearing errors than the old OUNPPM. The new OUNPPM was also used to simulate the effect of multipath on the performance of CVOR system, where in this case the local ground was assumed to be covered in snow. The results of this simulation were compared with the new OUNPPM simulation of the same scattering scenario in which the local ground was modeled as PEC, and it was observed that there was not much difference between the results. It can be deduced from the aforementioned results that the results with the new OUNPPM point in the direction which this improvement effort was meant to achieve.

Another capability of the new OUNPPM as regards being used for VOR coverage analysis was demonstrated. From this thesis, the conclusions are as follows:

I. This software tool presents a means for siting CVOR/DVOR systems at sites that have scatterers (i.e., reflecting surfaces that cause multipath) in the radiated field of the CVOR/DVOR ground station.

II. Secondly, this tool aids the investigation of the effects of ground station parameters such as antenna separation, counterpoise size, height of antennas above the counterpoise, height of counterpoise above ground and the electrical properties of the local ground.

III. This tool can also be used to study the field pattern of any system whose configuration is akin to that of an antenna- an antenna array on a circular counterpoise or a counterpoise whose outline is close to that of a circle.

IV. Field and flight data to validate counterpoise modulation effects in the DVOR alone has been difficult to come by. Hence validation of the model was done by comparisons of the antenna patterns from the CVOR/DVOR computer model and NEC-BSC simulations. Further validation is necessary.

V. The improvement in this new OUNPPM should produce more accurate results than those of the old OUNPPM since the complete antenna array in the CVOR/DVOR systems has been modeled. Moreover, the systems have been modeled using a 3-D scattering analysis method and thus the computed fields reflect the inherent 3-D nature of the CVOR/DVOR ground station antenna-counterpoise configuration. Validation results with NEC-BSC show close agreement.

5.2 Recommendations

Although the CVOR/DVOR models developed in this thesis offers an improvement over the old model further improvements and validation can be attained and are recommended.

I. In section 3.2.1 it was mentioned that in the development of this model it was assumed that there was no coupling between the antennas of the CVOR/DVOR ground system. However the proximity of the CVOR/DVOR array elements implies that there will be coupling between antenna elements. In the DSB DVOR especially, antenna coupling is the major contributor to the station's intrinsic error. Inclusion of the effects of mutual coupling would significantly improve the accuracy of the VOR prediction tool.

II. Other error sources such as those caused by the blending function in the DVOR should be considered for inclusion in the OUNPPM.

III. In order to accurately account for effects of ground reflection on the performance of CVOR/DVOR, the effect of terrain roughness should be considered for inclusion into the new CVOR/DVOR model of the new OUNPPM.

IV. The effects of multipath from multiple scatterers on the performance of the CVOR/DVOR systems should be investigated, and validated.

V. A more complete DSB DVOR receiver model should be implemented. The analysis of the DSB DVOR as a superposition of two SSB DVORs in the new OUNPPM was based on the assumption that since in the DSB DVOR diametrically opposite antennas were excited to remove the counterpoise eccentricity effect, the DSB DVOR error can be obtained by adding the errors of two SSB DVORs. The validity of this assumption should be investigated further.

VI. Further validation via flight tests needed.

REFERENCES

[1] www.faa.gov, http://www.faa.gov/about/history/brief_history/ visited August 5, 2012.

[2] 2010 Federal Radionavigation Plan, DOT-VNTSC-RITA-08-02/DoD-4650.05.

[3] M. Kayton and W. R. Fried, "Terrestrial Radio-Navigation Systems," in *Avionics Navigation Systems*, 2nd Ed. New York, NY: John Wiley and Sons, 1997, pp. 108-127, ISBN 0-471-54795-6.

[4] S. Odunaiya and J. Blazyk, "Navigation and Landing Performance Prediction Models," Avionics Engineering Center, Ohio University, Sept. 2000.

[5] D. Quinet and S. Odunaiya, "Navigation Performance Prediction Model training manual Presented to the European CAA" Ohio University, Apr. 2006.

[6] G. W. Sims and S. Odunaiya, "User's manual for the modified Physical Optics VOR Model," Avionics Engineering Center, Ohio University, Ohio University, August 1991.

[7] Communication with Dr Simbo Odunaiya of Avionics Engineering Center, Ohio University, Athens OH on 08/11/2011 based on " Validation of Ohio University Navaids Performance Prediction Model (OUNPPM) Mathematical Model for Signal Interference in VOR Systems caused by Wind Turbine Farms," FAA William J. Hughes Technical Center, Navigation System Performance, AJP-7B3, June 10, 2010.

[8] A. Helfrick, "Principles of Avionics," Sixth Ed. Avionics Communications Inc. Leesburg, VA 2009, ISBN 978-188554427-8.

[9] H. C. Hurley, S. R Anderson, and H. F. Keary, "The CAA VHF Omnirange," Civil Aeronautics Administration Technical Development and Evaluation Center, Indianapolis, IN, Tech. Dev. Rep. 113, June, 1950.

[10] FAA Academy Training Manual, Federal Aviation Administration, VOR Principles & Figures Book, Course 40276-1, December, 1989.

[11] A. Alford, and K. G. Kandoian, “Ultra-high Frequency Loop Antennas,” AIEE Transactions, vol. 52, 1940.

[12] C. Bartone, “Fundamentals of Antennas for Communications, Navigation and Surveillance (CNS) Systems,” EEM Advancement Center Pte Ltd and GNSS Solutions Ltd, Copthorne Orchid, Singapore, Dec. 2010.

[13] S.R Anderson, and R. B. Flint, “The CAA Doppler Omnirange,” Federal Aviation Agency, Tech. Development Center, Indianapolis, IN, Tech. Dev. Rep. No. 392, April 1959.

[14] “VOR, VOR/DME, VORTAC Siting Criteria”, FAA Order 6820.10, April, 1986.

[15] V. E. Willey, “Development and Evaluation of a Double Sideband Doppler VOR System with High Level Reference Modulation,” National Aviation Facilities Experimental Center, Atlantic City, NJ, February, 1971.

[16] Y. T. Lo, and S.W. Lee, “Techniques for High-Frequency Problems,” Chapter 4 in *Antenna Handbook Theory, Applications, and Design.* New York, NY: Van Nostrand Reinhold Company, 1988, ISBN 0-442-2583-7.

[17] P. Y. Ufimtsev, “Physical Theory of Diffraction,” John Wiley & Sons, Inc., Hooken NJ 2007, ISBN 047009771X.

[18] D. A McNamara, C.W.I Pistorius and J.A.G Malherbe, “Introduction to the Uniform Theory of Diffraction,” Norwood MA: Artech House 1990. ISBN 0-89006-301-X.

[19] J. B. Keller, “Geometrical Theory of Diffraction,” Journal of Optical Society of America, vol. 52, pp. 116 – 130, 1962.

[20] R. G. Kouyoumjian and P. Pathak, “A uniform theory of diffraction for an edge in a perfectly conducting surface,” Proc. IEEE, vol. 62, pp. 448-1461, Nov. 1974.

[21] A. Alford, “Antenna System for Doppler VOR Ground Stations,” US Patent 3972044, Apr. 8. 1974.

[22] R. J. Marhefka, and J.W Silvestro, “Near Zone-Basic Scattering Code User’s Manual with Space Station Applications,” NASA Tech. Rep. 716199-13, NASA Langley Research Center, Hampton, VA, March 1989.

[23] C. A Balanis, “Antenna Theory,” Third Edition New York, NY: John Wiley and Sons, Inc., Hooken NJ 2005. ISBN 0-471-66782-X.

[24] R. J Marhefka, handwritten notes on the derivation of diffraction points for a source over an elliptical disk, 1974, Electroscience Laboratory, Ohio State University.

APPENDIX A: CODE DESCRIPTION

The CVOR/DVOR error prediction software was developed through object-oriented programming using C++. Two (2) classes are defined for the VOR ground station and airborne receiver. These classes are

- VOR_Source
- VOR_Receiver

Previously developed ground characterization and PO scattering modules are modified to enable incorporation of the VOR_Source and VOR_Receiver classes developed in this thesis into the old OUNPPM.

A.1

The private members of an object of the VOR_Source class are initialized to define the following properties of the CVOR/DVOR ground station.

1) VOR type (*v_type*): Conventional VOR or Doppler VOR
2) Position of VOR counterpoise specified by the position vector of center of the counterpoise (*cp_pos*).
3) Position of a specific element of antenna array (*src_pos*): This is necessary in order to compute the scattered field from a specific antenna. This parameter can be reset to reflect the processing of another antenna by a member function *Reset_VOR_Source*.
4) Radius of VOR counterpoise (*cp_rad*)
5) Height of VOR antenna above the counterpoise (*ant_ht*)

6) VOR frequency (freq): 108-118 MHz

7) Wavelength (lambda): Wavelength at frequency of antenna whose position is specified by *src_pos* in 3).

8) Angular frequency of signal fed to antenna whose position is specified *src_pos* in 3).

9) Wave number field radiated from antenna whose position is specified by *src_pos* in 3).

10) An integer/index to specify the antenna being processed (*antenna_index*)

11) Wedge factor (*en*): A GTD/UTD parameter to characterize a half plane.

12) Ground elevation at the CVOR/DVOR transmitting station (*grnd_elev*).

13) Number of antenna (*No_Of_Ant*): 4 for conventional VOR and 51 for Doppler VOR.

14) Arrays are declared and initialized to hold frequencies, angular frequencies, wavelengths, wave numbers and positions of all antennas: *freq_vec*, omega_*vec, lambda_vec*, beta_*vec*.

A flow-chart for the 3-D UTD field computation routine (*Fields*) member function of the VOR_Source class is given below. There are three overloaded versions of this function. With the properties of the VOR station set and the observation point/receiver position specified this routine gives references to the direct and ground reflected fields.

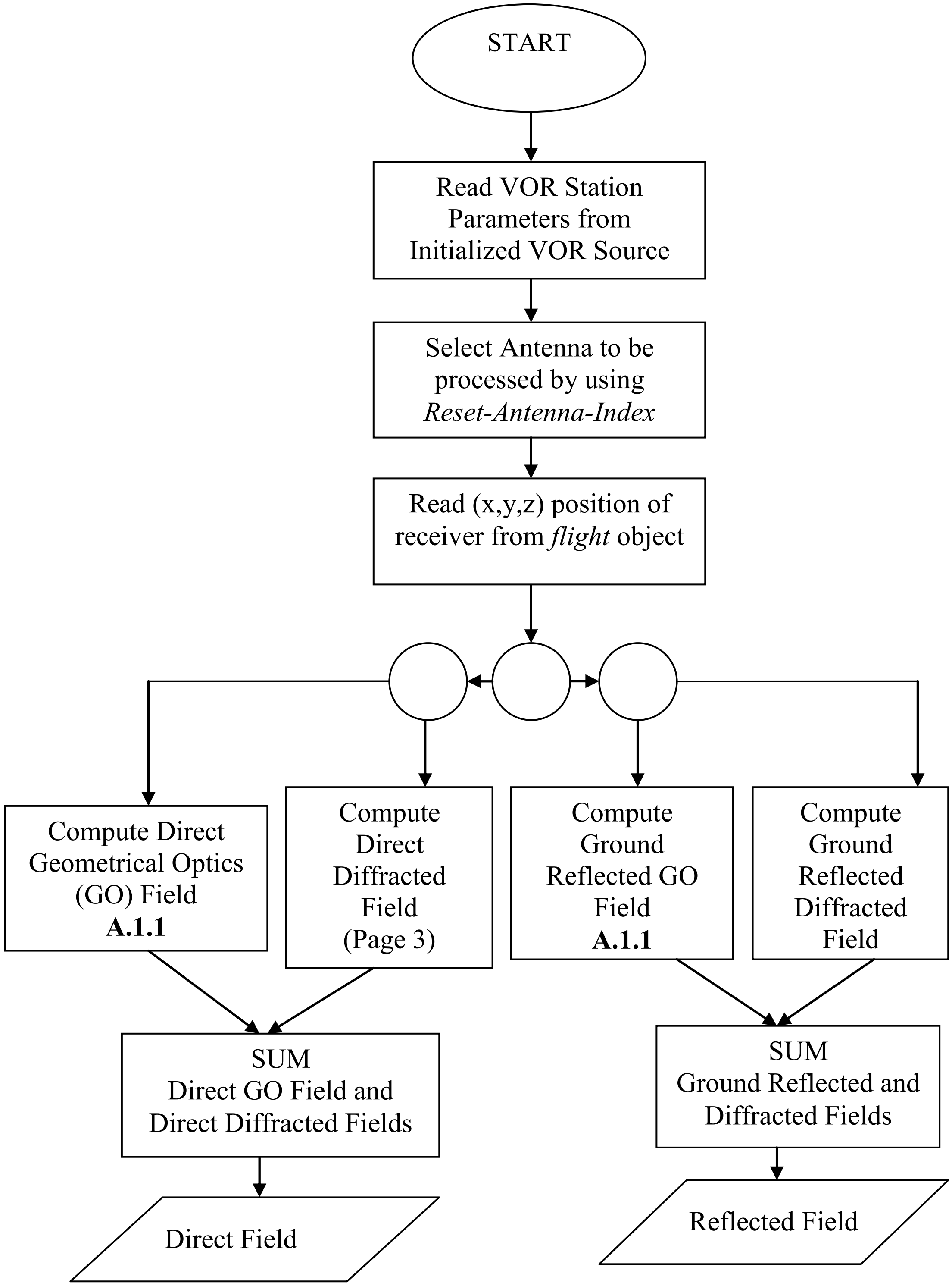

Figure A-1. Flow Diagram for *Fields* member function of *VOR_Source* class.

The function Fields is overloaded with another version that returns a dynamic array which holds the fields (direct + multipath) from all the antennas of the VOR antenna array. In the case of the CVOR this array will have 4 elements whilst a DSB DVOR array will have 101 elements – 1 for the center antenna, 50 for the upper sideband signals and another 50 for lower sideband signals.

A.1.1

The procedure to compute the geometrical optics field is given on page 64 of this document.

A.1.2

The flow diagram in Figure A-2 shows the basic elements of computing the diffracted component of the field from a specific antenna that arrives at the observation point.

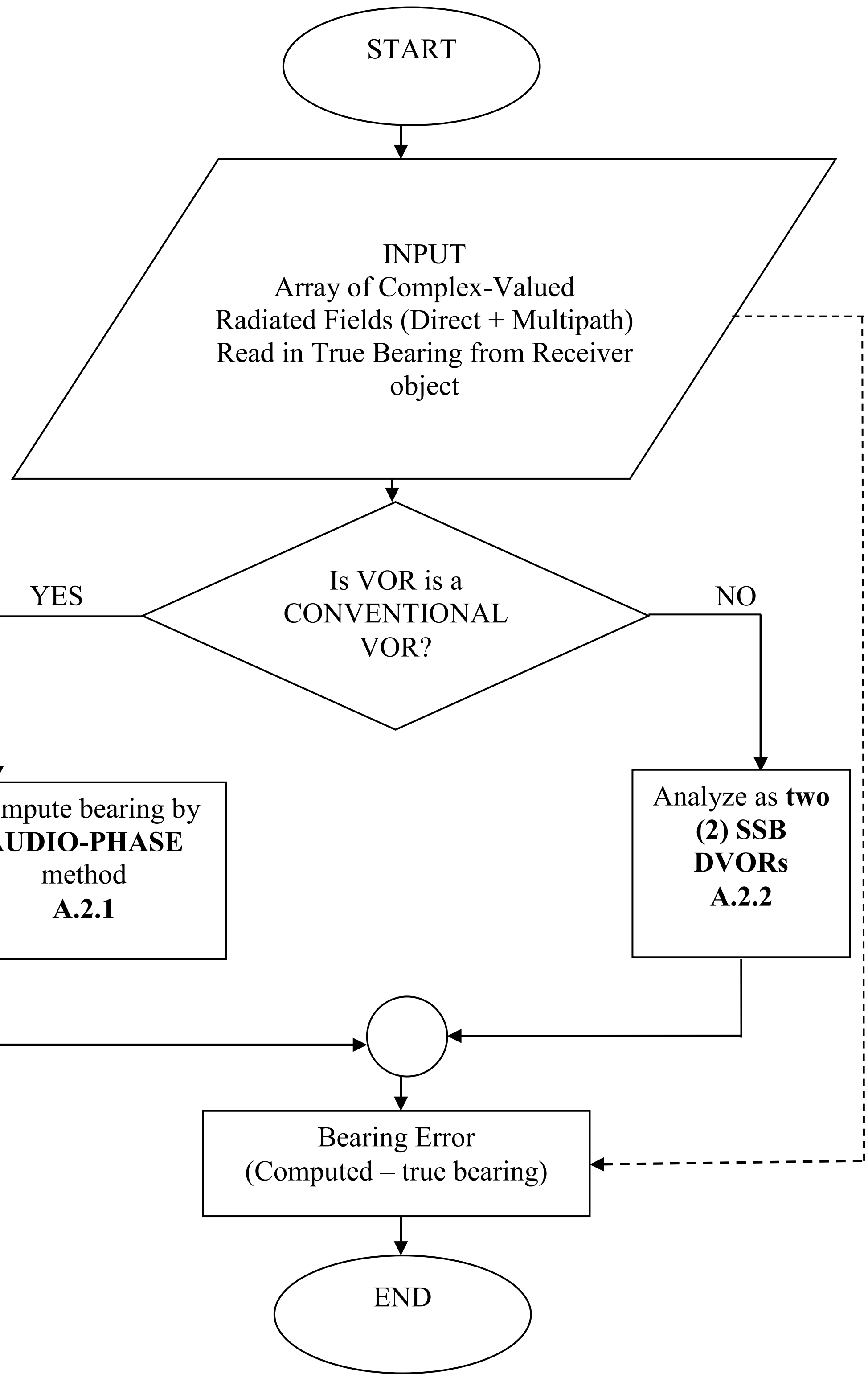

Figure A-2. Receiver class *bearing error* member function.

A.2.1 The following flow diagram is for the AUDIOPHASE method for computing the bearing of a receiver which receives fields from a Conventional VOR.

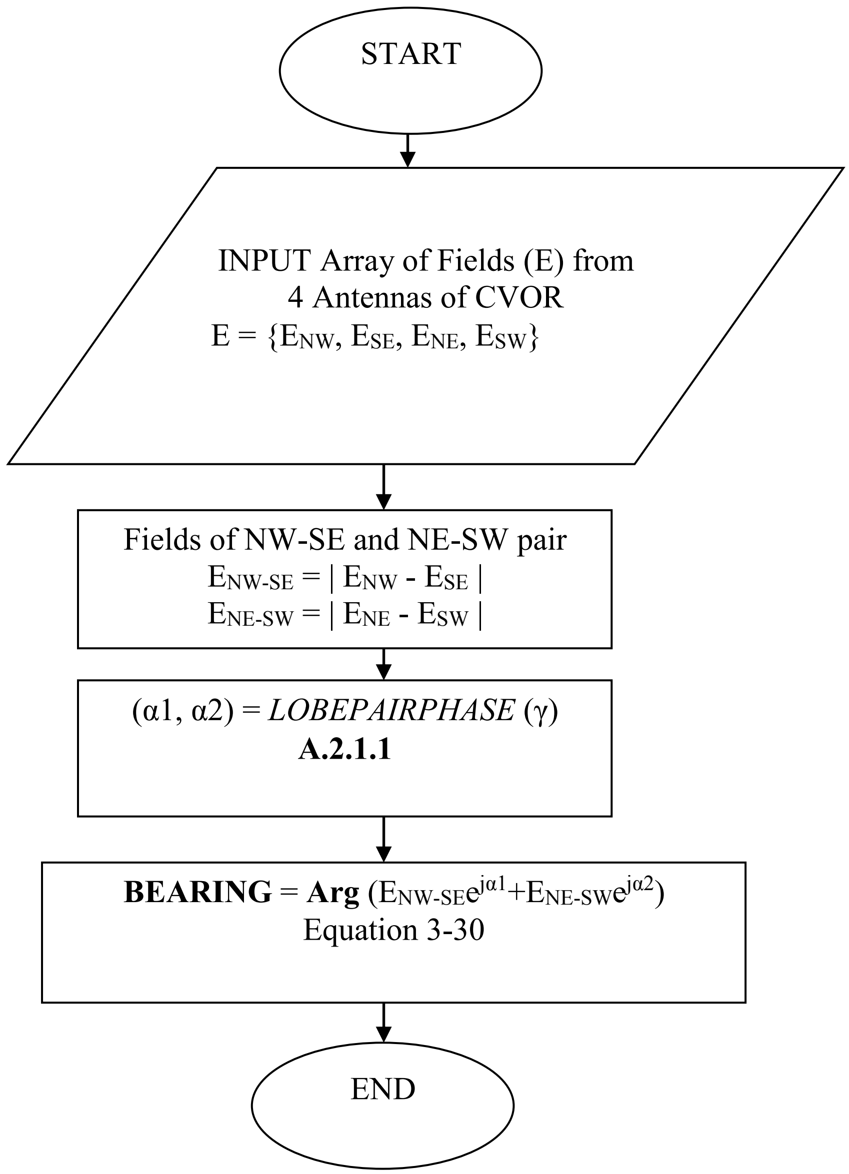

Figure A-3. Audiophase method of analyzing CVOR

A.2.1.1. The function LOBEPAIRPHASE assigns phases equal to the phase differences between signals from CVOR antenna pairs and the reference signal.

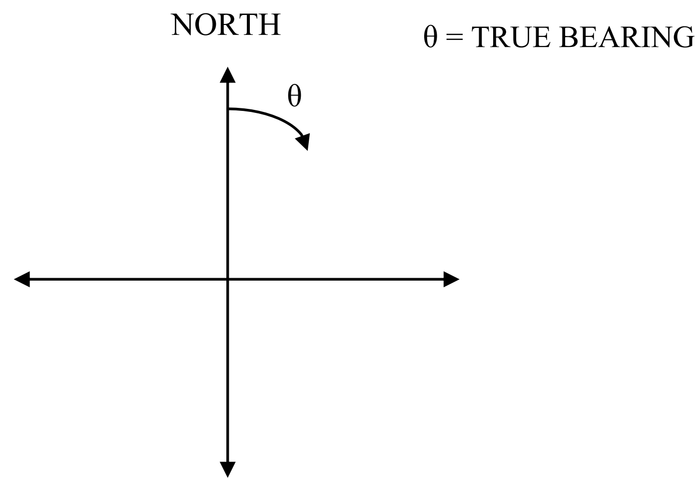

Figure A-4. Coordinate system for determining phase of lobe for antenna pairs.

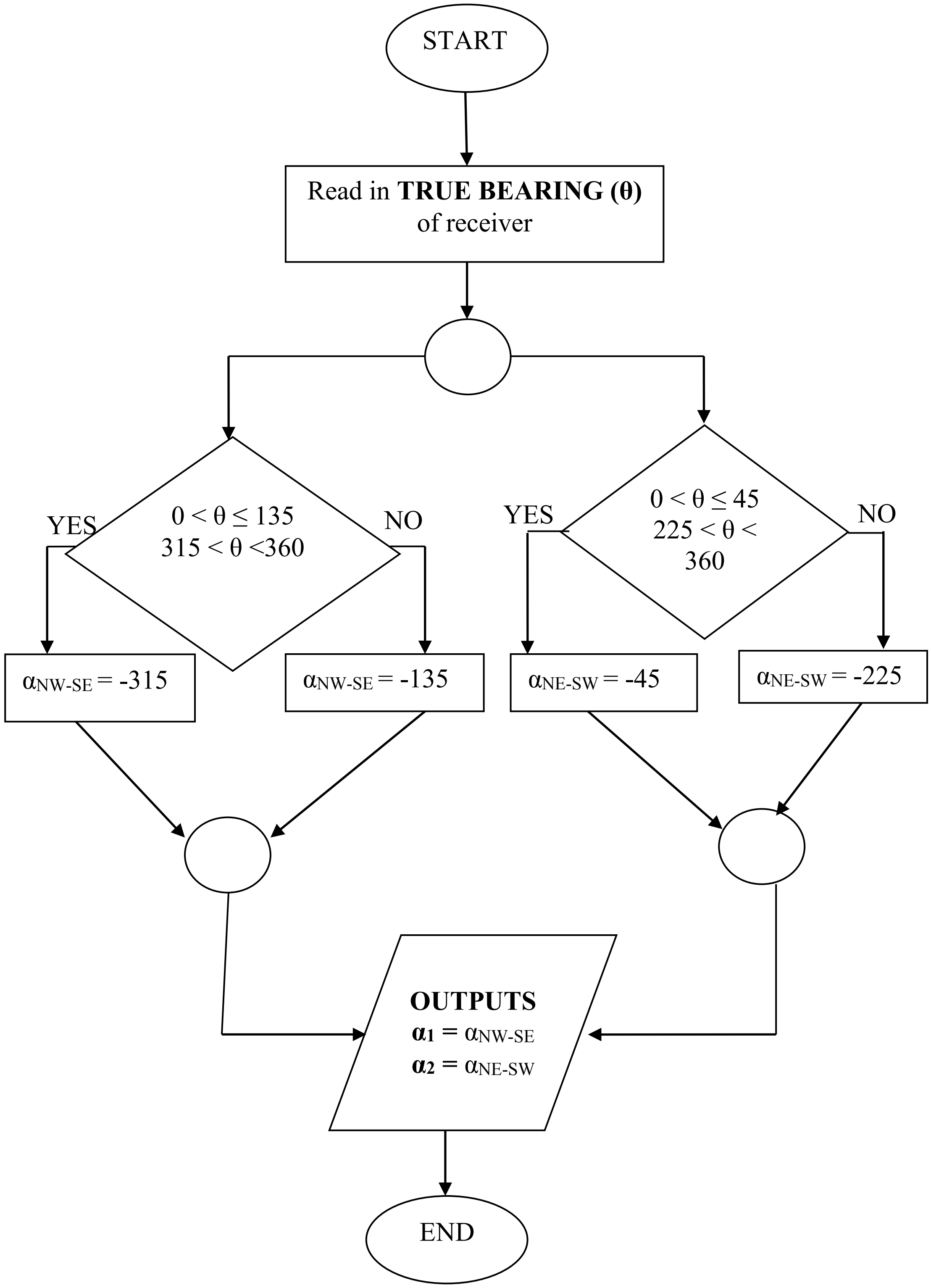

Figure A-5. Basic elements of the function LOBEPAIRPHASE

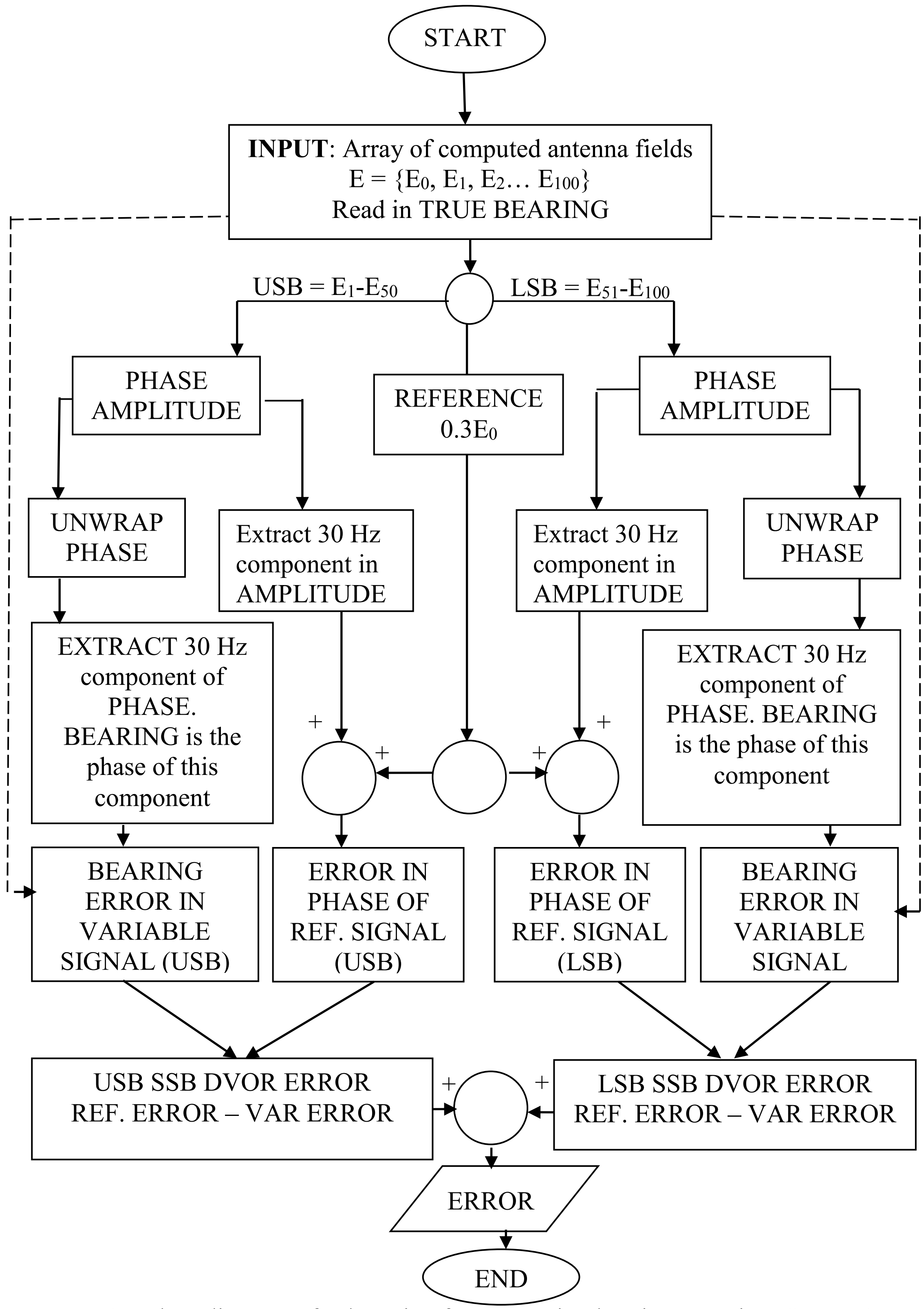

*Figure A-6.*Flow diagram of subroutine for computing bearing error in DSB DVOR.

APPENDIX B: FINDING DIFFRACTION POINTS FOR A SOURCE MOUNTED ABOVE A CIRCULAR PLATE

This derivation was adapted from [24].

Position of source point = $\mathbf{P_s}$ (s_x,s_y,s_z)

Direction of observation unit vector = $\hat{\mathbf{s}}$ (d_x,d_y,d_z)

Contour of circle =C (a, Φ)

Radius of circle = a

Polar angle of circle =Φ

Unit tangent vector at to circle = $\hat{t}$ (Φ)

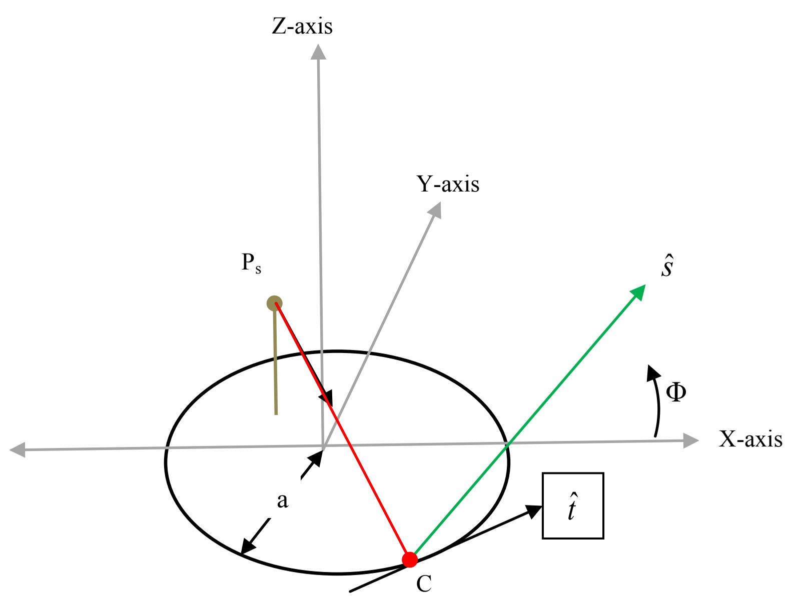

Figure B-1. Illustration of geometric set-up for computing diffraction points.

C(a, Φ) = acosΦ + asinΦ

$$\bar{t} = \frac{\partial C}{\partial \Phi} = -a\sin\Phi + a\cos\Phi$$

$$\hat{t} = \frac{\bar{t}}{|\bar{t}|} = -\sin\Phi + \cos\Phi$$

$$\overline{P_S C} = (a\cos\Phi - s_x)\hat{x} + (a\sin\Phi - s_y)\hat{y} + (-s_z)\hat{z}$$

$$\begin{aligned}\left|\overline{P_S C}\right|^2 &= (a\cos\Phi - s_x)^2 + (a\sin\Phi - s_y)^2 + (-s_z)^2 \\ &= a^2\cos^2\Phi - 2as_x\cos\Phi + s_x^2 + a^2\sin^2\Phi - 2as_y\sin\Phi + s_y^2 + s_z^2 \\ &= a^2 + s^2 - 2as_x\cos\Phi - 2as_y\sin\Phi\end{aligned}$$

$$\left|\overline{P_S C}\right|^2 = \Gamma - 2as_x\cos\Phi - 2as_y\sin\Phi s\ ,$$

$$where\ \Gamma = a^2 + s^2$$

$$\hat{s}^i = \frac{\overline{P_s C}}{\left|\overline{P_s C}\right|}$$

$$\begin{aligned}\overline{P_s C} \bullet \hat{t} &= -\sin\Phi(a\cos\Phi - s_x) + \cos\Phi(a\sin\Phi - s_y) \\ &= -a\cos\Phi\sin\Phi + s_x\sin\Phi + a\cos\Phi\sin\Phi - s_y\cos\Phi \\ &= s_x\sin\Phi - s_y\cos\Phi\end{aligned}$$

Direction of observation

$$\hat{s}^d = d_x\hat{x} + d_y\hat{y} + d_z\hat{z}$$

From Keller's Law of Edge Diffraction:

$$\hat{s}^i \bullet \hat{t} = \hat{s}^d \bullet \hat{t}$$

$$\frac{\overline{P_s C}}{\left|\overline{P_s C}\right|} \bullet \hat{t} = \hat{s}^d \bullet \hat{t}$$

$$\hat{s}^d \bullet \hat{t} = -d_x \sin\Phi + d_y \cos\Phi$$

$$\overline{P_s C} \bullet \hat{t} = \left|\overline{P_s C}\right| \hat{s}^d \bullet \hat{t}$$

$$\left(\overline{P_s C} \bullet \hat{t}\right)^2 = \left(\left|\overline{P_s C}\right| \hat{s}^d \bullet \hat{t}\right)^2$$

$$\left(\overline{P_s C} \bullet \hat{t}\right)^2 = \left(s_x \sin\Phi - s_y \cos\Phi\right)^2 = s_x^2 \sin^2\Phi - 2 s_x s_y \sin\Phi\cos\Phi + s_y^2 \cos^2\Phi$$

$$\left(\hat{s}^d \bullet \hat{t}\right)^2 = \left(-d_x \sin\Phi + d_y \cos\Phi\right)^2 = d_x^2 \sin^2\Phi - 2 d_x d_y \sin\Phi\cos\Phi + d_y^2 \cos^2\Phi$$

$$\begin{aligned}\left|\overline{P_s C}\right|^2 \left(\hat{s}^d \bullet \hat{t}\right)^2 &= \left(\Gamma - 2as_x \cos\Phi - 2as_y \sin\Phi\right) \\ &\quad * \left(d_x^2 \sin^2\Phi - 2 d_x d_y \sin\Phi\cos\Phi + d_y^2 \cos^2\Phi\right)\end{aligned}$$

$$\begin{aligned}\left|\overline{P_s C}\right|^2 \left(\hat{s}^d \bullet \hat{t}\right)^2 &= \Gamma d_x^2 \sin^2\Phi - 2\Gamma d_x d_y \sin\Phi\cos\Phi + \Gamma d_y^2 \cos^2\Phi - 2as_x d_x^2 \sin^2\Phi\cos\Phi + \\ &\quad 4as_x d_x d_y \sin\Phi\cos^2\Phi - 2as_x d_y^2 \cos^3\Phi - 2as_y d_x^2 \sin^3\Phi \\ &\quad + 4as_y d_x d_y \sin^2\Phi\cos\Phi - 2as_y d_y^2 \sin\Phi\cos^2\Phi\end{aligned}$$

Grouping terms

$$\begin{aligned}&\left|\overline{P_s C}\right|^2 \left(\hat{s}^d \bullet \hat{t}\right)^2 = \Gamma d_x^2 \sin^2\Phi - 2\Gamma d_x d_y \sin\Phi\cos\Phi + \Gamma d_y^2 \cos^2\Phi + \\ &\left(4as_y d_x d_y \sin^2\Phi\cos\Phi - 2as_x d_x^2 \sin^2\Phi\cos\Phi\right) + \left(4as_x d_x d_y \sin\Phi\cos^2\Phi - 2as_y d_y^2 \sin\Phi\cos^2\Phi\right) \\ &- 2as_x d_y^2 \cos^3\Phi - 2as_y d_x^2 \sin^3\Phi\end{aligned}$$

$$\begin{aligned}&\left|\overline{P_s C}\right|^2 \left(\hat{s}^d \bullet \hat{t}\right)^2 = \Gamma d_x^2 \sin^2\Phi - 2\Gamma d_x d_y \sin\Phi\cos\Phi + \Gamma d_y^2 \cos^2\Phi + \\ &\left(4as_y d_x d_y - 2as_x d_x^2\right)\sin^2\Phi\cos\Phi + \left(4as_x d_x d_y - 2as_y d_y^2\right)\sin\Phi\cos^2\Phi \\ &- 2as_x d_y^2 \cos^3\Phi - 2as_y d_x^2 \sin^3\Phi\end{aligned}$$

$$f(\Phi) = \left(\overline{P_s C} \bullet \hat{t}\right)^2 - \left|\overline{P_s C}\right|^2 \left(\hat{s}^d \bullet \hat{t}\right)^2 = 0$$

$$f(\Phi) = \left(s_x^2 - \Gamma d_x^2\right)\sin^2\Phi - 2\left(s_x s_y - \Gamma d_x d_y\right)\sin\Phi\cos\Phi + \left(s_y^2 - \Gamma d_y^2\right)\cos^2\Phi$$
$$- \left(4as_y d_x d_y - 2as_x d_x^2\right)\sin^2\Phi\cos\Phi - \left(4as_x d_x d_y - 2as_y d_y^2\right)\sin\Phi\cos^2\Phi$$
$$+ 2as_x d_y^2 \cos^3\Phi + 2as_y d_x^2 \sin^3\Phi = 0$$

$$A = s_x^2 - \Gamma d_x^2$$

$$B = 2\left(s_x s_y - \Gamma d_x d_y\right)$$

$$E = 4as_y d_x d_y - 2as_x d_x^2$$

$$F = 4as_x d_x d_y - 2as_y d_y^2$$

$$H = 2as_y d_x^2$$

$$G = 2as_x d_y^2$$

$$f(\Phi) = A\sin^2\Phi - B\sin\Phi\cos\Phi + D\cos^2\Phi - E\sin^2\Phi\cos\Phi - F\sin\Phi\cos^2\Phi$$
$$+ G\cos^3\Phi + H\sin^3\Phi = 0$$

From Euler:

$$\cos\Phi = \frac{e^{j\Phi} + e^{-j\Phi}}{2}$$

$$\sin\Phi = \frac{e^{j\Phi} - e^{-j\Phi}}{j2}$$

$$let\ \gamma = e^{j\Phi} \Rightarrow \frac{1}{\gamma} = e^{-j\Phi}$$

$$\cos\Phi = \frac{\gamma^2 + 1}{2\gamma}$$

$$\cos^2\Phi = \frac{\gamma^4 + 2\gamma^2 + 1}{4\gamma^2}$$

$$\cos^3\Phi = \frac{\gamma^6 + 3\gamma^4 + 3\gamma^2 + 1}{8\gamma^3}$$

$$\sin\Phi = \frac{\gamma^2 - 1}{j2\gamma}$$

$$\sin^2\Phi = \frac{\gamma^4 - 2\gamma^2 + 1}{-4\gamma^2}$$

$$\sin^3\Phi = \frac{\gamma^6 - 3\gamma^4 + 3\gamma^2 - 1}{-j8\gamma^3}$$

$$\sin\Phi\cos\Phi = \frac{\gamma^4 - 1}{j4\gamma^2}$$

$$\sin^2\Phi\cos\Phi = \frac{\gamma^6 - \gamma^4 - \gamma^2 + 1}{-8\gamma^3}$$

$$\sin\Phi\cos^2\Phi = \frac{\gamma^6 + \gamma^4 - \gamma^2 - 1}{j8\gamma^3}$$

$$\begin{aligned} f(\gamma) = {} & j2\gamma\left(A\gamma^4 - 2A\gamma^2 + A\right) + 2\gamma\left(B\gamma^4 - B\right) - j2\gamma\left(D\gamma^4 + 2D\gamma^2 + D\right) \\ & - j\left(E\gamma^6 - E\gamma^4 - E\gamma^2 + E\right) + \left(F\gamma^6 + F\gamma^4 - F\gamma^2 - F\right) - j\left(G\gamma^6 + 3G\gamma^4 + 3G\gamma^2 + G\right) \\ & + \left(H\gamma^6 - 3H\gamma^4 + 3H\gamma^2 - H\right) \end{aligned}$$

$$\begin{aligned} = {} & j2A\gamma^5 - j4A\gamma^3 + j2A\gamma + 2B\gamma^5 - 2B\gamma - j2D\gamma^5 - j4D\gamma^3 - j2D\gamma - jE\gamma^6 \\ & + jE\gamma^4 + jE\gamma^2 - jE + F\gamma^6 + F\gamma^4 - F\gamma^2 - F - jG\gamma^6 - j3G\gamma^4 - j3G\gamma^2 - jG \\ & + H\gamma^6 - 3H\gamma^4 + 3H\gamma^2 - H \end{aligned}$$

$$\begin{aligned} f(\gamma) = {} & (F + H - jG - jE)\gamma^6 + (2B + j2A - j2D)\gamma^5 + (F - 3H + jE - j3G)\gamma^4 + (-j4A - j4D)\gamma^3 \\ & + (3H - F + jE - j3G)\gamma^2 + (-2B + j2A - j2D)\gamma + (-F - H - jE - jG) = 0 \end{aligned}$$

The diffraction points are the arguments of some of the roots of the polynomial f (γ). All the roots must be tested using Keller's Law of edge diffraction to find which roots' arguments represent actual diffraction points. This formulation was used in section 3.2.1.3 to determine the diffraction points along the edge of the counterpoise.

Thesis and Dissertation Services